NUMERICAL SIMULATIONS OF THE RESTRICTED NONLINEAR SYSTEM

by

Joel U. Bretheim

A dissertation submitted to Johns Hopkins University
in conformity with the requirements for the degree of
Doctor of Philosophy

Baltimore, Maryland
February, 2018

Abstract

The restricted nonlinear (RNL) model is a simplified model for wall-bounded turbulence derived directly from the Navier-Stokes equations by restricting the nonlinear interaction between non-zero streamwise Fourier modes. The model is motivated by the prevalence of streamwise coherent structures in wall-bounded turbulent flows. In the last several decades, these flow structures have motivated many analytical, experimental, and numerical investigations to better understand the role they play in the dynamics of wall-bounded turbulence. The simplified nature of the RNL system offers a new, more tractable approach to understanding, for example, the connection between streamwise coherent structures and the momentum transfer mechanisms of wall-bounded turbulence.

Numerical simulations of wall-bounded turbulence using the RNL model have been shown to generate realistic mean velocity profiles in canonical wall-bounded flows at low Reynolds numbers. Initial simulations at higher Reynolds numbers produced less accurate results, and while a logarithmic region had been observed, its von Kármán constant is not consistent with the standard logarithmic law. In direct numerical simulations (DNS) of a half-channel flow, we demonstrate in the first part of this work that limiting

the streamwise-varying wavenumber support of RNL turbulence (producing a system which we term the 'band-limited' RNL model) to one or a few empirically determined modes improves its predictions considerably. In particular, the mean velocity profiles obtained with the band-limited RNL model follow standard logarithmic behavior for a range of moderate Reynolds numbers. Despite the more tractable nature of the RNL system, DNS of higher Reynolds number RNL flows are still limited by the demanding cross-plane resolution requirements for full resolution of the viscous terms.

In the second part of this work we extend the RNL model to arbitrarily high Reynolds numbers by developing a RNL large eddy simulation (LES) framework along with a method to systematically identify an appropriate streamwise wavenumber support based on spectral properties of wall-bounded turbulence. This method leads to a band-limited RNL-LES system that is successful in reproducing some of the most important statistical features captured in previous low to moderate Reynolds number simulations, e.g., the mean velocity and second-order moment profiles. As in the low to moderate Reynolds number DNS setting, the RNL-LES framework offers a new approach to understanding the connection between coherent structures and the momentum transfer mechanisms of wall-bounded turbulence, but at arbitrarily high Reynolds numbers. Additionally, we demonstrate a new numerical approach to solving the RNL-LES equations that exploits the properties of the system to achieve significant computational speedups relative to traditional LES.

In the third and final part of this work, we introduce a new approach to

the reduced-order modeling of wind farms based on the RNL-LES framework. The low computational cost nature of the RNL-LES framework makes it a potentially attractive candidate for a reduced-order approach to studying wind farm behavior over a range of conditions. To enable this, we use an appropriately altered version of the actuator disk turbine model to evaluate the ability of the RNL-LES framework to simulate very large wind farms in the fully-developed regime through comparisons with standard LES of wind farms under a variety of conditions. Then, the low computational cost of the RNL-LES approach is exploited to conduct a large parametric study of several vertically-staggered wind farm configurations in order to assess the impact of vertical staggering on wind farm power production.

Dissertation committee

Readers

Dennice F. Gayme (Co-Advisor)
Assistant Professor and Carol Linde Croft Faculty Scholar
Department of Mechanical Engineering
Johns Hopkins Whiting School of Engineering

Charles Meneveau (Co-Advisor)
Louis M. Sardella Professor of Mechanical Engineering
Department of Mechanical Engineering
Johns Hopkins Whiting School of Engineering

Anand Gnanadesikan
Professor
Department of Earth and Planetary Sciences
Johns Hopkins Krieger School of Arts and Sciences

Acknowledgments

I acknowledge the National Science Foundation and the taxpayers who support it. In particular, I am thankful for the IGERT and WINDINSPIRE programs which have created several valuable experiences for me these last few years.

I acknowledge the many developers of our computational fluid dynamics code ("Lesgo"), as well as the developers and maintainers behind GNU/Linux, Matplotlib, the Maryland Advanced Research Computing Center, and the countless other computational tools and resources which make this research possible.

I acknowledge all those who have educated me over many years across many states. In particular, I thank the professors of Grove City College and Johns Hopkins University. I thank Lori Graham-Brady, Michael Shields, and Anand Gnanadesikan for serving on my graduate board oral exam. Additional thanks to Anand Gnanadesikan for serving as a reader of this dissertation.

I acknowledge the staff of Johns Hopkins University for helping with all those activities outside of research. In particular, I thank Mike Bernard, Kevin Adams, Shahin Zand, Barb Adamson, Shawna O'Brien, and Marty Devaney.

I acknowledge the many current and former members, over several years,

of Charles Meneveau's research group and Dennice Gayme's research group. I especially thank Tony Martínez, Carl Shapiro, Xiang Yang, Perry Johnson, Ismail Hameduddin, Vaughan Thomas, Claire VerHulst, Jason Graham, Richard Stevens, Michael Wilczek, and Di Yang, for helping me learn how to conduct research, troubleshoot problems, and for their fun, humor, conversations, and companionship along the way.

I acknowledge several other Hopkins and Baltimore friends for enriching my experience at this university and in this city. In particular, I thank Adam Sierakowski, Dan Willen, Michelle Chen, Eshwan Ramudu, Jimi Oke, Chris & Abby Vazquez, Brian & Michelle O'Leary, and the Malmins.

I gratefully acknowledge my co-advisors, Charles Meneveau and Dennice Gayme, whose patience was essential and from whom I have learned a great deal in the realm of research. I thank them for taking me on as a student, for their thoughtful advising, and for ensuring I never had to worry about funding.

I acknowledge the Hermesmann family, whose support and encouragement will not be forgotten.

Most of all, I acknowledge those who have given me more than I could ever write down: my mother, my father, my brother, my wife, my son, and my Creator.

Dedication

To my mother, Patricia, who has shown me what it means to love unselfishly.

To my father, Daniel, who has taught me that the extra mile is never crowded.

To the only brother for me, Michael, who is in spirit fierce and free.

To my wife, Laura, who has shown me what it means to be kind.

To my son, Owen, who has delivered joy at a much-needed time.

To my Savior, Christ Jesus, who has shown me what it means to forgive.

Table of Contents

Table of Contents ix

List of Tables xi

List of Figures xii

1 Introduction 1

2 Direct numerical simulations of the restricted nonlinear system 15

2.1 Introduction 15

2.2 Restricted nonlinear equations for wall-bounded turbulence 15

2.3 Simulation setting and numerical approach 17

2.4 Results and discussion 18

3 Large eddy simulations of the restricted nonlinear system 27

3.1 Introduction 27

3.2 Restricted nonlinear equations for wall-bounded turbulence 28

3.2.1 Restricted nonlinear model 28
3.2.2 Restricted nonlinear large eddy simulation model . . . 30
3.3 Numerical approach 32
3.4 Simulation descriptions and results 38
3.4.1 Baseline RNL-LES results 40
3.4.2 LES cases 44
3.4.3 Band-limited RNL-LES cases 50

4 Application to reduced-order wind farm simulations 64
4.1 Introduction 64
4.2 Dynamical RNL-LES equations 65
4.3 Numerical setup 70
4.4 Results and discussion 72
4.4.1 Validating the RNL-LES wind farm model against LES 73
4.4.2 Application to vertical staggering 79

5 Conclusions 87

References 93

Vita 112

List of Tables

3.1 **Baseline RNL-LES and LES cases (labeled B- and L-, respectively). The lengthscale λ_{SGS_0} is effectively the smallest scale in the simulation and decreases with increasing grid size.** . 40

3.2 **Band-limited RNL-LES cases.** 51

4.1 **Summary of simulation cases. The label 'R' refers to RNL-LES while 'L' refers to LES. N_r and N_c refer to the number of turbine rows and columns, respectively. The turbine-to-turbine spacings in the spanwise and streamwise directions are indicated by S_y and S_x, respectively.** 73

4.2 **Groups are organized according to the nomenclature of Table 4.1, where each configuration is run at multiple different vertical staggerings. A particular case is referred to, for example, as R1-20, which indicates group R1 at 20% staggering.** 81

List of Figures

2.1 Mean streamwise velocity profiles for various simulated cases (square brackets indicate streamwise-, spanwise-, and time-averaging). The baseline RNL dynamics (red square markers in outer plot) is unconstrained, while all other cases have perturbation dynamics limited to the wavenumber(s) specified. Note: plot markers are sparse for data presentation purposes and do not indicate grid resolution. 19

2.2 (a) Plane snapshots of streamwise velocity u_{T} in a RNL half-channel Poiseuille flow simulation at $\mathrm{Re}_\tau = 180$. In this case, the streamwise dynamics is limited to the set of wavenumbers $k_x = \{0, 6, 6.5, 7\}$ in a box of size $[L_x, L_y, L_z]/\delta = [4\pi, 1, 2\pi]$. The horizontal plane is taken at height $y^+ = 15$. Cross-stream snapshots at (b) $\mathrm{Re}_\tau = 110$ limited to $k_x = \{0, 3.5\}$ and (c) $\mathrm{Re}_\tau = 340$ limited to $k_x = \{0, 14\}$. 21

2.3 (a) Skin-friction coefficient, c_f, as a function of friction Reynolds number. The dashed line is the standard empirical correlation for c_f based on obtaining u_0 from equation (2.3). Circles are the band-limited RNL results run at the optimal k_x. (b) The optimal mode's corresponding streamwise wavelength, $\lambda_x = 2\pi/k_x$, as a function of friction Reynolds number (in inner units). 23

2.4 Profiles of (a) streamwise normal Reynolds stress (inner units) and (b) Reynolds shear stress (outer units). The superscript prime $'$ indicates departure from the time-averaged value. The DNS values are from the channel flow simulation of Moser, Kim, and Mansour (1999) 25

2.5 Spanwise energy spectra obtained from the band-limited RNL model at $\mathrm{Re}_\tau = 180$, at two wall-normal locations. The RNL system is constrained to a single perturbation wavenumber of $k_x = 7$. Dashed lines are channel flow DNS data from Moser, Kim, and Mansour (1999) Symbols are RNL data. 26

3.1 Time histories of average perturbation kinetic energy (defined in Equation (3.10)) for different $k_{x,n}$ modes: LES case L-1 and baseline RNL-LES case B-1 (see Table 3.1). For these cases, the $k_{x,n}$ modes with $n > 5$ (plotted with dashed gray lines) are sustained indefinitely in the LES system but rapidly decay to zero (after the transients die out) in the RNL-LES system and remain there even as turbulence is sustained. 34

3.2 Instantaneous snapshot contours of streamwise velocity in the y-z cross-plane: (a) Baseline RNL-LES case B-4 and (b) LES case L-4. For display purposes, we plot half the channel width ($L_z/H = 2\pi$). 41

3.3 Baseline RNL-LES results (open symbols) compared to representative LES reference (case L-3, black line) data: (a) mean velocity profiles (b) streamwise Reynolds stress profiles. The superscript prime $'$ in the plot label indicates fluctuations about the time-averaged value. 43

3.4 Premultiplied vorticity spectra, $k_{x,n}(E_{\omega_x\omega_x} + E_{\omega_y\omega_y} + E_{\omega_z\omega_z})$. Each plot is normalized by its own maximum value. The colorbars are the same for each panel (0 to 1, blue to red). 45

3.5 Normalized streamwise wavelengths (solid black circles) corresponding to the streamwise wavenumbers identified in Figure 3.4. The hollow black circles correspond to the nearest discrete wavelengths just outside the peak range identified in Figure 3.4. The dashed red line represents the optimized wavelength in viscous units ($\lambda_x^+ = 150$) identified in the DNS-RNL system (Bretheim, Meneveau, and Gayme 2015). 47

3.6 LES results. Left column: premultiplied wall-normal vorticity streamwise spectra, $k_{x,n}(E_{\omega_y\omega_y})$. Right column: premultiplied streamwise velocity energy spanwise spectra, $k_{z,n}(E_{uu})$. Each plot is normalized by its own maximum value. Cases: L-2 (top), L-4 (middle), L-6 (bottom). The colorbars are the same for each panel (0 to 1, blue to red). 48

3.7 Premultiplied one-dimensional spanwise energy spectra $(k_{z,n}E_{uu})$ for LES. The colorbars are the same for each panel (0 to 1, blue to red). 50

3.8 Instantaneous snapshot contours of streamwise velocity in the y-z cross-plane: band-limited RNL-LES case R-4(i). For display purposes, we plot half the channel width ($L_z/H = 2\pi$). 52

3.9 Band-limited RNL-LES mean velocity and streamwise Reynolds stress profiles (Regime I cases). The superscript prime $'$ in the plot labels indicates fluctuations about the time-averaged value. Note: for clearer data presentation, the plot markers in panel (a) are sparsened and do not indicate grid resolution. 53

3.10 Mean velocity profiles of variants of case R-1 of Table 3.2. Variations about the optimized single nonzero streamwise wavenumber ($k_{x,4}$) illustrate the sensitivity of the results to the chosen $k_{x,n}$. 54

3.11 Comparison of premultiplied one-dimensional spanwise energy spectra for LES (top row), baseline RNL-LES (middle row), and band-limited RNL-LES (bottom row). The left column shows the energy in the streamwise component of velocity while the right column shows the energy in the wall-normal component of velocity. The colorbars are the same for each panel (0 to 1, blue to red). 56

3.12 Premultiplied two-dimensional spanwise energy spectra for LES (case L-4) at $y/H \sim 0.02$. Values normalized by in-plane maximum (colorbars are 0 to 1, blue to red). Vertical dashed lines correspond to the streamwise wavelengths associated with $k_{x,13}$ and $k_{x,18}$. 58

3.13 Band-limited and baseline RNL-LES mean velocity profiles in Regime II: (a) first attempt to include the large ($k_{x,7}$) scale in case R-5(ii), without limiting its influence near the wall and (b) the influence of $k_{x,7}$ is limited near the wall, resulting in a more accurate mean velocity profile. 60

3.14 Band-limited RNL-LES mean velocity and streamwise Reynolds stress profiles (Regime II cases). The superscript prime $'$ in the plot labels indicates fluctuations about the time-averaged value. 61

4.1 Contour plots of streamwise velocity obtained from (a) LES and (b) RNL-LES. Specifically, (a) corresponds to the turbine layout for case L3 of Table 4.1 while (b) shows the same configuration in the y-z cross-plane, which is effectively the domain of case R3, which only has a two-dimensional physical space grid and represents out-of-plane variations in streamwise Fourier space. The red and blue circles represent the turbine rotor swept areas and the dashed black line in panel (b) is at the turbine baseline hub height (z_h). 74

4.2 Mean velocity profiles for the RNL-LES system (circle markers) with and without turbines compared to those for the LES system (solid lines) and the rough wall log law (dashed line). 76

4.3 Contours of mean streamwise velocity in the y-z cross-plane for representative LES and RNL-LES cases. 77

4.4 Vertical profiles of the relevant terms in the kinetic energy budget in Equation (4.13). Note that each term is horizontally-averaged for plotting purposes and each term is nondimensionalized by u_*^3/H. Markers and solid lines denote RNL-LES and LES data, respectively. The horizontal dashed lines mark the turbine region. 79

4.5 Vertical profiles of the power extraction and kinetic energy flux terms of the kinetic energy budget for all vertical staggering levels considered herein. Each term is nondimensionalized by u_*^3/H and horizontally-averaged. The black shaded region (panel a) shows the rotor swept area of the vertically-aligned turbines. The red and blue shaded regions (panels b and c) show the rotor swept areas of the upwardly- and downwardly-staggered turbines, respectively, with the purple region indicating area overlap. 82

4.6 Representative wind farm power signals for both RNL-LES and LES at vertical staggering levels of 10% and 30%. The power signals are normalized by the time-averaged value of the power produced by the corresponding vertically-aligned wind farm. Red curves represent the average power production of upwardly-staggered rows while the blue curves are that of the downwardly-staggered rows. The black curves show the overall wind farm power output. 83

4.7 Wind farm power output gain as a function of vertical staggering. All results (a), net power gains (b), upper row power gains (c), and lower row power gains (d). 85

Chapter 1

Introduction

The search for structure and organization in turbulence continues to motivate all manner of experimental and numerical studies (Smits, McKeon, and Marusic 2011), often with the goal of developing or improving models. In the special case of wall-bounded turbulence, many such studies are inspired by the coherent flow structures which form in the presence of the solid boundary (see Robinson 1991, and references therein). In particular, experimental (Kline et al. 1967; Adrian, Meinhart, and Tomkins 2000; Hutchins and Marusic 2007b) and analytical (Farrell and Ioannou 1993; Hamilton, Kim, and Waleffe 1995; Bamieh and Dahleh 2001; Jovanović and Bamieh 2005) evidence suggest that coherent structures elongated in the streamwise direction play a key role in the production, storage, and redistribution of kinetic energy within the flow. As such, the ubiquity and dynamical significance of streamwise coherent structures represent a natural starting point for the development of reduced-order models of wall-bounded turbulence.

One such model is the two-dimensional three-velocity-component (2D/3C) model, which has been studied in the context of both turbulent plane Couette

flow (Bobba 2004; Gayme et al. 2010; Gayme et al. 2011) and turbulent pipe flow (Bourguignon and McKeon 2011). Under external stochastic forcing, the 2D/3C plane Couette flow system develops roll/streak structures consistent with wall-bounded turbulence and its mean velocity profile transitions from a linear, laminar profile to the "S-shaped" profile characteristic of fully-developed turbulent plane Couette flow (Gayme et al. 2010). While the 2D/3C model is nonlinear and captures the mechanism responsible for the blunting of the turbulent mean velocity profile, it does not include streamwise-varying velocity perturbations. It therefore requires continuous external excitation to generate a perturbation field and to maintain turbulence (Bobba 2004).

The restricted nonlinear (RNL) model is similarly inspired by the prevalence of streamwise-coherent strucures in wall-bounded turbulence. However, it is more comprehensive than the 2D/3C model in that it describes the evolution of both a streamwise-constant velocity field, which we refer to as the "streamwise mean flow," as well as the evolution of a streamwise-varying perturbation field that interacts with the streamwise mean flow. The resulting coupling between the streamwise mean flow and the streamwise-varying perturbation field allows the RNL system to maintain turbulence through a self-sustaining cycle in which the streamwise mean flow is influenced by a perturbation field that is in turn regulated through interactions with the streamwise mean flow (Thomas et al. 2014). The RNL model, which has been studied in the context of plane Couette flow (Thomas et al. 2014) and plane Poiseuille flow (Constantinou et al. 2014), thus captures two mechanisms absent in the linearized NS system without the need for external stochastic

forcing: the momentum transfer responsible for the turbulent mean velocity profile and the self-sustaining mechanism of turbulence.

The RNL system was introduced in the context of stochastic structural stability theory (S3T) based models of turbulent plane Couette flow by Farrell and Ioannou (2012) and further characterized by Thomas et al. (2014) and Constantinou et al. (2014). The RNL system of equations is derived directly from the Navier-Stokes (N-S) equations by partitioning the flow variables into streamwise-averaged mean quantities and streamwise-varying perturbations about that mean and then restricting the nonlinear interactions between the streamwise-varying perturbation velocities. Specifically, it restricts the nonlinear interactions between perturbation velocities to the streamwise-averaged component of the quadratic perturbation-perturbation nonlinearity. This simplification of the governing equations of fluid motion has profound consequences in terms of simplifying both the analytical and computational complexity of the flow representation. The ability of such a model to reproduce key flow features also opens up many new questions about the role of the nonlinearity in the dynamical and statistical behavior of wall-bounded turbulence.

The RNL system can be interpreted as an approximation of the S3T model, developed earlier by Farrell and Ioannou (2003) for applications in planetary atmospheric fluid dynamics and later applied to canonical wall-bounded turbulence problems (see, e.g., Farrell et al. 2012; Farrell and Ioannou 2012; Farrell et al. 2016; Farrell, Ioannou, and Nikolaidis 2017; Farrell and Ioannou 2017). The S3T model describes the evolution of a streamwise-averaged mean

flow (first cumulant) and corresponding streamwise-averaged perturbation covariance (second cumulant); the equations are closed by parameterizing or neglecting the third- and higher-order cumulants. The RNL dynamics similarly comprise the joint evolution of a streamwise-averaged mean flow and a single realization of the perturbation dynamics, as discussed in detail in Farrell, Gayme, and Ioannou (2017).

The RNL model has been explored via direct numerical simulation (DNS), i.e., including full resolution of the viscous term within the context of the RNL equations, in both turbulent plane Couette flow (Thomas et al. 2014; Thomas et al. 2015) and turbulent channel flows (Constantinou et al. 2014; Farrell et al. 2016). Thomas et al. (2014) demonstrate that the RNL system, despite its relative simplicity, produces a self-sustaining turbulence in plane Couette flow. Therefore, the RNL model does not require continuous forcing in order to maintain turbulence, unlike many other common reduced-order models of wall-bounded turbulence, such as linear models[1] or the two-dimensional three-component (2D/3C) model (Bobba 2004; Gayme et al. 2010; Gayme et al. 2011; Bourguignon and McKeon 2011). Thomas et al. (2014) also show that at low Reynolds number the first- and second-order statistics of the RNL system compare favorably to those obtained by DNS of the full N-S system.

Constantinou et al. (2014) explore the RNL system in the context of Poiseuille flow at higher Reynolds numbers, finding the RNL system to closely resemble the dynamics of the full N-S system, albeit with important quantitative differences. In particular, they note the presence of a logarithmic region in

[1] Romanov proved that the laminar solution to Couette flow is linearly stable (Romanov 1973)

the mean velocity profiles, but with significantly different values of the von Kármán and additive constants. Their results indicate that these quantitative differences become more pronounced at higher Reynolds numbers.

One interesting attribute of the RNL system is that it supports a drastically reduced number of streamwise modes relative to the N-S system. Constantinou et al. (2014) report that only the first seven streamwise Fourier modes are sustained in their RNL simulation of turbulent channel flow at a friction Reynolds number ($Re_\tau = u_\tau H/\nu$) of 950, where u_τ is the friction velocity, and H and ν are the channel half-height and kinematic viscosity, respectively. As a point of reference, a corresponding DNS of the full N-S system would sustain energy in all resolved modes, a total of 128 streamwise Fourier modes in this case. Thomas et al. (2015) report similar behavior in turbulent plane Couette flow. Furthermore, they demonstrate that the number and range of sustained streamwise Fourier components depends on the size of the domain. By extending the streamwise length L_x of the domain to values as high as $96\pi H$, the authors prove the existence of an upper streamwise wavelength (or lower streamwise wavenumber) limit in the natural support of RNL turbulence.

Thomas et al. (2015), Bretheim, Meneveau, and Gayme (2015), and Farrell et al. (2016) further demonstrate that it is possible to sustain RNL turbulence on only a single nonzero streamwise Fourier mode interacting with the mean flow. In the latter paper, the authors describe the idea of 'band-limiting' the streamwise wavelengths contributing to the RNL dynamics. In a range of moderately high Reynolds numbers, they show that by judiciously selecting the range of wavelengths included in the RNL simulation, the resulting mean

velocity profiles exhibit a logarithmic portion, with a realistic von Kármán constant and intercept. The band-limiting procedure thus proves effective in improving the similarity between RNL turbulence and full N-S turbulence. Alizard (2017) shows such a 'band-limited' or 'minimal' RNL model also supports invariant solutions in a subcritical channel flow, including traveling wave solutions which are self-similar with respect to the centerline Reynolds number. The band-limited RNL system differs from the original (or 'baseline') RNL system in that the streamwise-varying Fourier components supporting the dynamics are pre-selected for simulation. This 'band' of streamwise modes differs from the natural set of streamwise wavelengths supported by the baseline system. In this sense, the baseline version represents the 'natural' dynamics of the RNL system while the band-limited version represents the optimized RNL dynamics. Throughout the rest of this work, we thus distinguish between the baseline and band-limited versions of the RNL system, with the key difference being the particular streamwise wavenumber support of the system.

The RNL system hinges on a formal separation between a streamwise mean and streamwise-varying parts, and in that sense the RNL model falls into the general class of systems referred to as quasi-linear (QL) models of turbulent wall-bounded shear flow (such models are extensively used in the atmospheric sciences (Farrell and Ioannou 2007; Marston, Conover, and Schneider 2008; Srinivasan and Young 2012)). However, the RNL model is spatially-averaged in only the streamwise direction; a more generalized approach might define the separation about a particular lengthscale and may

apply the separation across more than one flow direction. This is the approach taken by Constantinou, Farrell, and Ioannou (2016) and Marston, Chini, and Tobias (2016) in the Generalized Quasilinear (GQL) approximation. The GQL framework employs a spectral filter in each of the horizontal directions to separate variables into large scale and small scale parts and then neglects nonlinear interactions between the small scale parts. This approach, which has been successfully applied to simulations of zonal jets (Constantinou, Farrell, and Ioannou 2016; Marston, Chini, and Tobias 2016) and rotating Couette flow (Tobias and Marston 2017), can be reduced to the RNL approach by defining a streamwise-averaged mean flow with wavenumber cutoffs of zero in the streamwise direction and infinity in the spanwise direction. The RNL system can thus be thought of as a special case of the GQL framework, where the large scale is taken as the zeroth streamwise wavenumber. As discussed above, the zeroth streamwise wavenumber, which represents the streamwise-averaged flow, is a physically significant choice for the large scale as streamwise coherent structures carry a large portion of the flow energy and these types of structures are ubiquitous in the flow (Morrison et al. 2004; Hutchins and Marusic 2007b; Hutchins and Marusic 2007a).

Both the RNL and GQL frameworks provide a natural way to approach reduced-order modeling in terms of the important constituent lengthscales active in the turbulence dynamics. These approaches offer the possibility of constructing a lengthscale 'backbone' of wall-bounded turbulence. A related decomposition-based approach is the resolvent analysis technique proposed by McKeon and Sharma (2010) and further explored by Sharma and McKeon

(2013) and Sharma, Moarref, and McKeon (2017). These resolvent methods have, by incorporating time frequency information, proven successful in identifying a key wavenumber-frequency 'kernel' or 'skeleton' of turbulent pipe flow. The aforementioned researchers use this approach to build a modeling framework for wall-bounded turbulent flows based on a set of self-similar structures and their triadically-interacting wavenumber sets. In addition to answering fundamental questions about the structure of wall-bounded turbulence, this procedure could provide more insight into the important streamwise modes of the RNL system.

In a similar vein is the class of asymptotically reduced models, which are built around the invariant solutions (Gibson, Halcrow, and Cvitanović 2008) and exact coherent structures (Waleffe 2001) identified in canonical wall-bounded turbulence systems. While quite distinct from the resolvent and RNL methods, this class of methods similarly offers a window into the morphological structure of wall-bounded turbulence and the lengthscale 'backbone' which springs from the interaction of the flow with the wall. And unlike the RNL and GQL approaches, this technique does not rely on an explicitly stated separation of scales. The review papers by Kawahara, Uhlmann, and Veen (2012) and Klewicki, Chini, and Gibson (2017) and the references therein provide helpful overviews of this segment of the literature.

The ability of the RNL system to realistically approximate turbulence in wall-bounded flows is interesting in and of itself, given that it neglects a significant portion of the nonlinear terms in the N-S equations which give rise to much of the complexity of turbulence. Another reason why the RNL model is

a promising tool for the study of wall-bounded turbulence is its computational tractability relative to DNS of the N-S system, which is known to be computationally expensive. Since the RNL system is a reduced-order simplification of the N-S system, a proper numerical implementation can achieve significant savings in terms of computational cost, making it an attractive candidate for numerical investigations.

The numerical investigations of the RNL system have thus far been limited to low and moderate friction Reynolds numbers. In the second chapter of this work, we present results of DNS of the RNL system at low to moderate Reynolds numbers, including the band-limited RNL system. While these studies have proven fruitful in gaining better understanding of the RNL system, we seek to probe the RNL dynamics at significantly higher Reynolds numbers with an eye toward extending the approach to engineering application areas such as wind farms (Bretheim, Meneveau, and Gayme 2017). These flows typically occur at friction Reynolds numbers several orders of magnitude higher than can currently be reached with state-of-the-art DNS methods (for reference, the most advanced DNS of channel flow is the 2015 simulation of Lee and Moser (2015) at a friction Reynolds number of about 5200). Although the RNL model significantly reduces the computational burden, the spatial resolution required in the cross-stream plane is typically comparable to that required in DNS and thus can still be prohibitive at large Reynolds numbers. In order to extend the RNL system to arbitrarily high Reynolds numbers, we employ a large eddy simulation (LES) framework - a coarse-grained approach where the small spatial scales are not resolved but their effects are modeled by

means of a sub-grid stress tensor and the wall stress is modeled with a wall model.

In the third chapter of this work, we propose a new version of the RNL model suitable for wall-modeled large eddy simulations at arbitrarily high Reynolds numbers. We then identify and implement a new, tailored numerical approach that exploits the specific attributes of the RNL-LES system to increase computational efficiency and realize the full potential of the model for reduced-order simulations. This numerical approach entails a hybrid physical/Fourier space grid, with certain operations performed efficiently in Fourier space. As done in the work by Bretheim, Meneveau, and Gayme (2015), which investigates what we henceforth refer to as the DNS-RNL system because it fully resolves the viscous scales, we introduce a 'band-limited' version of the RNL-LES system, which improves the accuracy of the RNL-LES results analogously to the improvement seen in the band-limited DNS-RNL system. A main contribution of this work is the identification of a method to select the streamwise wavenumber bands *a priori*, which overcomes a shortcoming of the prior DNS-RNL work (Bretheim, Meneveau, and Gayme 2015), where the streamwise wavenumber bands were determined empirically and *a posteriori*. Our method to select the streamwise wavenumber band consists of analyzing LES reference data, where we identify a key lengthscale and its scaling behavior based on spectral characteristics of wall-bounded turbulence. This enables the proper band-limiting of the RNL-LES system to achieve improved statistical flow quantities relative to the baseline RNL-LES

system. More specifically, we connect the important streamwise wavenumbers to corresponding scales in the vertical cross-plane by analysing energy spectra, in order to understand the effects of streamwise band-limiting on the cross-plane dynamics. Finally, we analyze the sensitivity of the results to the chosen streamwise wavenumbers.

In the fourth chapter, we apply the RNL-LES framework to simulations of very large wind farms. The last decade has witnessed the advent of large eddy simulation (LES) as a useful approach to study many of the fluid dynamical aspects of large scale wind turbine arrays and their interaction with the atmospheric boundary layer (ABL) (Stevens and Meneveau 2017). LES of wind turbine arrays is based on the numerical integration of the filtered (coarse-grained) Navier-Stokes equations in three dimensions, coupled with a model to represent the effects of the turbines on the flow field. An early example of this approach came with the work of Calaf, Meneveau, and Meyers (2010), who provided a detailed study of a wind turbine array in the ABL under the asymptotic fully-developed regime, i.e., under the assumption that the streamwise extent of the wind farm is significantly greater than the characteristic height of the ABL.

Since the work of Calaf, Meneveau, and Meyers (2010), the LES approach has been deployed in a number of wind farm studies, including the characterization of turbine wakes and wake effects in wind farms (Xie and Archer 2015; Abkar, Sharifi, and Porté-Agel 2016; Howland et al. 2016), wind farm configuration or layout effects (Meyers and Meneveau 2012; Archer, Mirzaeisefat, and Lee 2013; Stevens, Gayme, and Meneveau 2014; Stevens, Gayme, and

Meneveau 2016b), the effects of atmospheric stability in wind farms (Abkar and Porté-Agel 2013; Lu and Porté-Agel 2015; Abkar and Porté-Agel 2015b), meteorological effects due to wind farms (Calaf, Parlange, and Meneveau 2011; Lu and Porté-Agel 2011; Sharma, Parlange, and Calaf 2017), vertical entrainment of kinetic energy (Calaf, Meneveau, and Meyers 2010; Abkar and Porté-Agel 2014; VerHulst and Meneveau 2014; Allaerts and Meyers 2015; VerHulst and Meneveau 2015) in wind farms, turbine aerodynamics (Martínez-Tossas, Churchfield, and Leonardi 2015; Martínez-Tossas, Churchfield, and Meneveau 2017; Jha and Schmitz 2018), and wind farm control strategies for frequency regulation (Shapiro et al. 2016; Boersma et al. 2017; Shapiro et al. 2017b; Shapiro et al. 2017a). LES has also provided reference data for the development of both analyticalBastankhah and Porté-Agel 2014; Abkar and Porté-Agel 2015a; Stevens, Gayme, and Meneveau 2015; Stevens, Gayme, and Meneveau 2016a and reduced-order numerical (VerHulst and Meneveau 2014; Iungo et al. 2015; Iungo et al. 2017) models. It is clear that the LES approach to wind farm studies has rapidly gained a foothold in the literature and proven fruitful in a diverse set of engineering and scientific areas relevant to wind farms. The recent review article by Stevens and Meneveau (2017), which offers a comprehensive overview of the state of wind farm flow physics, further details the current state of LES as an approach to wind farm studies.

While LES has proved very useful as a research tool in studying a wide array of wind farm problems, it is nonetheless a relatively high cost approach in terms of computational expense. The cost of high-fidelity LES has thus restricted its use primarily to the academic domain, where researchers have

access to extensive supercomputer resources for wind farm LES studies and lack the time pressures faced by industry for the design and construction of wind farms. As Boersma et al. (2017) states, "the resulting computation time [of three-dimensional high-fidelity wind farm models] can be in order of days or weeks... [and] the computation time needed for LES is in general more than the total time that is simulated." Taking into account even just a few parameters like turbine hub height, swept area, and layout, the parameter space for a wind farm design easily reaches into the many thousands of unique configurations and waiting days or weeks for a single simulation to run is not feasible for a competitive industry. This reality has impeded the progress of LES-based research approaches in the wind energy industry, where lower cost computational approaches based on the Reynolds-averaged Navier-Stokes (RANS) equations and engineering wake models tend to take precedence. Hence, there is interest to develop a reduced-order LES-based model for wind farm studies in order to enable faster computational studies which can be used, e.g., to investigate different wind farm designs.

This work explores such a model based on the recently formulated restricted nonlinear-LES equations (henceforth referred to as the RNL-LES system). This approach has recently been demonstrated (Bretheim, Meneveau, and Gayme 2018a) to accurately reproduce low-order turbulence statistics in a high Reynolds number half-channel flow at a fraction of the computational cost of traditional LES.

With the background and motivation of the RNL system established, we first present results of DNS of the RNL system in the second chapter of this

work, including results of the so-called band-limited RNL model. In the third chapter, we present results for the RNL-LES model, which extends the RNL system to arbitrarily high Reynolds numbers. In the fourth chapter, we apply the new RNL-LES framework to simulations of very large wind farms in the fully-developed regime. Finally, in the fifth and final chapter, we summarize the results and describe directions for future work.

Chapter 2

Direct numerical simulations of the restricted nonlinear system

2.1 Introduction

In section 2.2 we introduce the RNL system of equations, written in the standard Gibbs notation. We then describe our simulation setting and numerical approach in section 2.3, followed by a presentation and discussion of the results of our DNS of the baseline and band-limited RNL systems in section 2.4. The main contents of this chapter have appeared in the paper by Bretheim, Meneveau, and Gayme (2015).

2.2 Restricted nonlinear equations for wall-bounded turbulence

In the RNL model, the total velocity field, $\mathbf{u}_\mathrm{T}(x, y, z, t)$ (consisting of the respective streamwise, wall-normal, and spanwise components $(u_\mathrm{T}, v_\mathrm{T}, w_\mathrm{T})$ with y as the wall-normal direction) is decomposed as $\mathbf{u}_T = \mathbf{U} + \mathbf{u}$. Here $\mathbf{U}(y, z, t) = \langle \mathbf{u}_\mathrm{T} \rangle$ is the time-dependent streamwise-constant mean velocity,

and $\mathbf{u}(x, y, z, t)$ is the streamwise-varying "perturbation velocity." Here, angle brackets $\langle\ \rangle$ denote a streamwise-averaged quantity (note: in later chapters we use $\langle\ \rangle_x$ for the same purpose), averaged over the streamwise extent of the spatial domain (i.e., the $k_x = 0$ mode in a Fourier representation). The RNL model dynamics can then be written as the following system of equations:

$$\frac{\partial \mathbf{U}}{\partial t} + \mathbf{U} \cdot \nabla \mathbf{U} + \nabla P/\rho - \nu \nabla^2 \mathbf{U} = -\langle \mathbf{u} \cdot \nabla \mathbf{u} \rangle + \partial_x p_\infty \hat{\mathbf{i}}, \quad \nabla \cdot \mathbf{U} = \mathbf{0} \tag{2.1a}$$

$$\frac{\partial \mathbf{u}}{\partial t} + \mathbf{u} \cdot \nabla \mathbf{U} + \mathbf{U} \cdot \nabla \mathbf{u} + \nabla p/\rho - \nu \nabla^2 \mathbf{u} = 0, \quad \nabla \cdot \mathbf{u} = 0 \tag{2.1b}$$

with density ρ, kinematic viscosity ν, and constant pressure gradient forcing $\partial_x p_\infty$ in the streamwise direction. This system differs from the full incompressible N-S equations (decomposed in this manner) only in the omission of the term $\langle \mathbf{u} \cdot \nabla \mathbf{u} \rangle - \mathbf{u} \cdot \nabla \mathbf{u}$ from the right-hand side of the evolution equation for the streamwise-varying perturbation field (2.1b).

Prior RNL simulations have shown that most of the streamwise-varying modes decay in time, leaving only a modest number of streamwise-varying modes interacting with the $k_x = 0$ mode (the precise number and nature of these modes depends on Reynolds number and channel size (Constantinou et al. 2014; Thomas et al. 2014)). Here k_x refers to the non-dimensional wavenumber $k_x = \delta k_x' = \delta 2\pi / L_x \times (n)$, where n is a nonnegative integer.

In this section, we explore what level of streamwise complexity needs to be added to the RNL model in order to reproduce an extended log law. The simulation environment is Poiseuille flow in a half-channel geometry. The

cross-stream (y-z) plane is fully-resolved, containing the multiple scales expected in turbulent channel flow. Streamwise complexity is added to the RNL model by pre-selecting a set of streamwise-varying wavenumbers ($k_x \neq 0$) and limiting the RNL dynamics to interactions between this set of wavenumbers and the streamwise mean flow (i.e., the flow associated with $k_x = 0$). In this context, we investigate whether the RNL system can predict realistic logarithmic mean velocity distributions and characterize its behavior as we vary the set of $k_x \neq 0$ modes supporting the "band-limited" RNL turbulence.

2.3 Simulation setting and numerical approach

We simulate the RNL system by restricting the dynamics in an existing direct numerical simulation (DNS) code. The code employs a pseudospectral discretization in the streamwise (x) and spanwise (z) directions along with a centered second-order finite-difference scheme in the wall-normal (y) direction. Time integration is achieved with a second-order Adams-Bashforth method. No-slip and stress-free boundary conditions are imposed at the bottom and top walls, respectively, with periodic conditions in the horizontal directions. The 3/2 rule is applied for dealiasing. All simulations are conducted in a half-channel box of size $[L_x, L_y, L_z]/\delta = [4\pi, 1, 2\pi]$, where δ is the half-channel's height. We use uniform mesh-spacing in all coordinate directions and have cross-stream resolution of $[\Delta y^+, \Delta z^+] \approx [1.0, 7.0]$ for all Reynolds numbers considered herein. The half-channel box size and cross-stream resolution are thus comparable to those of the channel (Poiseuille) flow DNS of Kim, Moin, and Moser (1987) and Moser, Kim, and Mansour

(1999). As usual, the superscript $+$ indicates scaling by the inner variables of friction velocity and viscous lengthscale ($u_\tau = \sqrt{\tau_w/\rho} = \sqrt{-(\delta/\rho)\,\partial_x p_\infty}$ and $\delta_\nu = \nu/u_\tau$, respectively). The wall shear stress is τ_w and the friction Reynolds number is $\mathrm{Re}_\tau = u_\tau \delta/\nu$.

As previously mentioned, the RNL system naturally supports fewer streamwise modes (k_x) than the NS system (Constantinou et al. 2014; Thomas et al. 2014). Constantinou et al. (2014) reported that in a full-channel configuration at $\mathrm{Re}_\tau = 950$ (with $L_x = \pi\delta$), the RNL system sustained the six lowest streamwise-varying wavenumbers ($k_x = 2, 4, .., 12$), in addition to the streamwise mean flow ($k_x = 0$). The energy of the seventh and higher streamwise-varying wavenumbers ($k_x \geq 14$) decayed asymptotically to zero.

2.4 Results and discussion

Our simulations of RNL turbulence in a half-channel at $\mathrm{Re}_\tau = 180$ recover results similar to those of Constantinou et al. (2014), with the RNL turbulence naturally sustaining the five lowest equally-spaced streamwise-varying wavenumbers ($k_x = 0.5, 1.0, 1.5, 2.0, 2.5$, since $L_x = 4\pi\delta$), and the streamwise mean flow ($k_x = 0$). The corresponding mean velocity distribution is shown in Figure 2.1 with open square markers. As is apparent, the baseline RNL system overpredicts the mean streamwise velocity for $y^+ > 10$ and produces an approximately logarithmic region above $y^+ \sim 30$ with slope and intercept that are, however, not consistent with the well-known values for $\kappa \sim 0.41$ and $B \sim 5$. This behavior is similar to the results of Constantinou et al. (2014), who reported the existence of a logarithmic law in full-channel RNL turbulence

with $\kappa = 0.71, B = 11.1$ at $\mathrm{Re}_\tau = 350$ and $\kappa = 0.77, B = 14.0$ at $\mathrm{Re}_\tau = 950$.

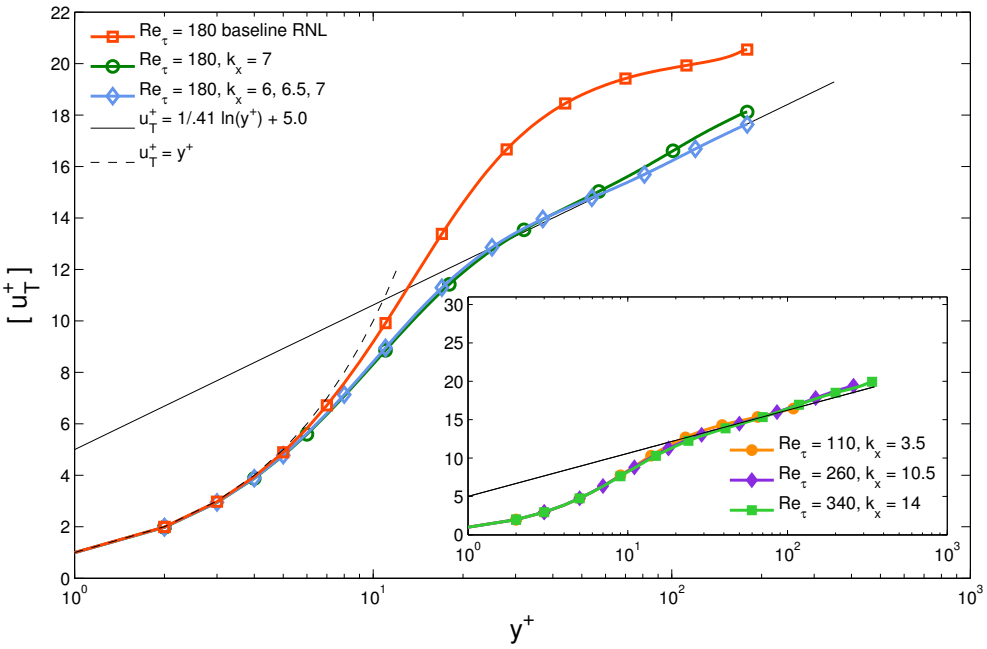

Figure 2.1: Mean streamwise velocity profiles for various simulated cases (square brackets indicate streamwise-, spanwise-, and time-averaging). The baseline RNL dynamics (red square markers in outer plot) is unconstrained, while all other cases have perturbation dynamics limited to the wavenumber(s) specified. Note: plot markers are sparse for data presentation purposes and do not indicate grid resolution.

These results raise the question of whether keeping a different set of streamwise-varying wavenumber modes for the perturbation field could lead to more accurate interaction dynamics and therefore produce more realistic mean velocity distributions. Specifically, we consider a RNL system that is band-limited to a reduced set of streamwise-varying wavenumbers. To clearly distinguish the two types of RNL systems discussed herein, we will hereafter refer to the RNL system without any mode-limiting as the baseline RNL system. First, we experiment with various choices of streamwise-varying wavenumbers supporting the flow. For a set of three wavenumbers

$k_x = \{6, 6.5, 7\}$, the resulting mean velocity profile is shown in Fig. 2.1 with open diamond markers. This figure shows that the band-limited system generates profiles that closely match the standard logarithmic law. In order to provide a qualitative view of the flow, a snapshot of the streamwise velocity is shown in Figure 2.2. The cross-stream structure displays realistic vortical structures while the band-limited nature of the streamwise-varying perturbations and the associated restriction to a particular set of streamwise wavelengths is clearly visible. These results demonstrate that the mean velocity profile obtained from simulations of the RNL system that are band-limited to only three streamwise-varying wavenumbers ($k_x = \{6, 6.5, 7\}$) yields an accurate mean velocity profile. The profile exhibits a logarithmic region with standard values of $\kappa = 0.41$ and $B = 5.0$.

The preceding results are achieved by constraining the dynamics of the perturbation field to a limited set of streamwise-varying modes, which essentially forces the flow to exist on some set of wavenumbers different from the set that naturally arises under the baseline RNL dynamics. In previous studies the RNL system has also been shown to sustain turbulence even in the case of a single mode interacting with the streamwise mean flow (Gayme et al. Nov. 2013). Figure 2.1 shows the mean turbulent velocity profile from such a case when the active streamwise-varying mode is $k_x = 7$ (open circle markers). These results show good agreement with the standard logarithmic law up to $y/\delta \sim 0.4$. Thus, the RNL system not only maintains turbulence when further limited to only one perturbation wavenumber but also yields an accurate mean velocity profile through interactions of $k_x = 0$ and $k_x = 7$.

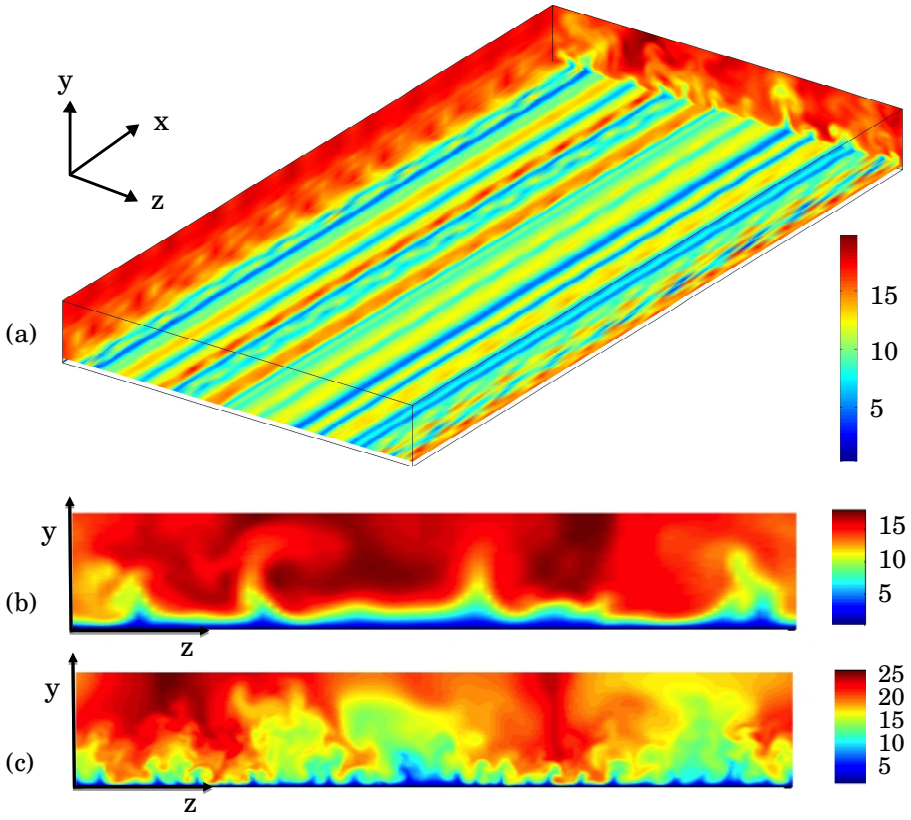

Figure 2.2: (a) Plane snapshots of streamwise velocity u_{T} in a RNL half-channel Poiseuille flow simulation at $\mathrm{Re}_\tau = 180$. In this case, the streamwise dynamics is limited to the set of wavenumbers $k_x = \{0, 6, 6.5, 7\}$ in a box of size $[L_x, L_y, L_z]/\delta = [4\pi, 1, 2\pi]$. The horizontal plane is taken at height $y^+ = 15$. Cross-stream snapshots at (b) $\mathrm{Re}_\tau = 110$ limited to $k_x = \{0, 3.5\}$ and (c) $\mathrm{Re}_\tau = 340$ limited to $k_x = \{0, 14\}$.

Next, we examine a range of Reynolds numbers. In order to simplify the testing as much as possible, we consider a perturbation field with only a single streamwise-varying mode. In order to decide which mode is retained in the model, we simulate the RNL system at each Reynolds number for a range of single $k_x \neq 0$ wavenumbers. For each case, we quantify deviations between the model and the standard log law by comparing a measure of the integrated velocity profile with well-known empirical correlations for channel flow. A natural metric for this comparison is the skin-friction coefficient

$$c_f = 2\tau_w / \left(\rho u_0^2\right). \tag{2.2}$$

In order to avoid relying on data at a single point (centerline velocity, u_0) we calculate the bulk average velocity, $u_b = \frac{1}{\delta}\int_0^\delta [u]\,\mathrm{d}y$ from the simulations (here and throughout, square brackets [ ] denote streamwise-, spanwise-, and time-averaged mean quantities). We relate the bulk velocity to the centerline velocity using the empirical relation $u_0 \approx u_\tau/\kappa + u_b$ (Pope 2000). By calculating the skin-friction in this way, we obtain a single value that characterizes the entire mean velocity profile. We then compare the band-limited RNL system's c_f to the following empirical correlation (Pope 2000) for c_f:

$$\sqrt{\frac{c_f}{2}} = \frac{u_0}{u_\tau} = \frac{1}{\kappa}\ln Re_\tau + B + B_1 \tag{2.3}$$

with $\kappa = 0.41$, $B = 5.0$, and $B_1 = 0.2$ (Pope 2000). We note that these values and the empirical correlation in Eq. (2.3) are for a full and not a half-channel, but the differences are expected to be acceptably small for present purposes. We refer to the single streamwise-varying wavenumber

that minimizes the relative error in the skin-friction coefficient (defined as $e_{c_f} = |c_{f,\text{sim}} - c_{f,\text{eq.(2.3)}}|/c_{f,\text{eq.(2.3)}}$) as the "optimal" wavenumber.

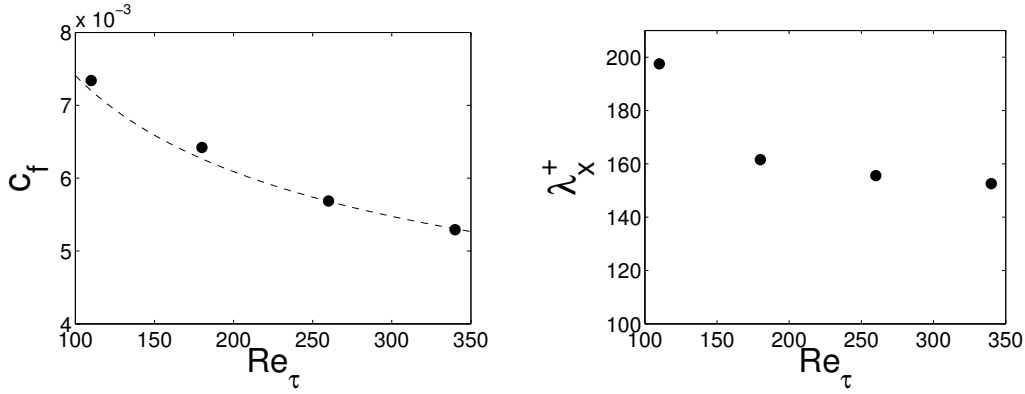

Figure 2.3: (a) Skin-friction coefficient, c_f, as a function of friction Reynolds number. The dashed line is the standard empirical correlation for c_f based on obtaining u_0 from equation (2.3). Circles are the band-limited RNL results run at the optimal k_x. (b) The optimal mode's corresponding streamwise wavelength, $\lambda_x = 2\pi/k_x$, as a function of friction Reynolds number (in inner units).

Figure 2.3 shows the c_f values obtained for the optimal streamwise wavenumber in panel (a) and the trend in the corresponding streamwise wavelength as a function of friction Reynolds number in panel (b). In initial tests, it was expected that perhaps λ_x would tend to a certain fraction of δ (outer scaling), but the results appear to show inner scaling instead, tending to a wavelength of about 150 viscous units. This wavelength is reminiscent of the well-documented near-wall structures reported by, e.g., Kline et al. (1967) who observed near-wall streak structures with an average spanwise spacing of 100 viscous units. Smith and Metzler (1983) further characterized these structures, showing their spacing in viscous units is "essentially invariant with Reynolds number" and increases with distance from the wall. Jiménez (2012)

also notes that the smallest structures within the near-wall region are of order 100 viscous units. Other studies (Jiménez and Moin 1991; Hamilton, Kim, and Waleffe 1995) have demonstrated that this length scale corresponds closely to the minimum spanwise channel width necessary to maintain turbulence. Further simulations at higher Reynolds numbers are required in order to establish whether this scaling can be maintained for arbitrarily high Reynolds numbers.

Next, second-order statistics are considered. Figure 2.4(a) shows that the baseline RNL model overpredicts the normal Reynolds stress in the streamwise direction at $\mathrm{Re}_\tau = 180$, with a peak value of ≈ 17 occurring at $y^+ \approx 20$. This differs from the Navier-Stokes DNS system's peak value of ≈ 7.06 at $y^+ \approx 15.28$ (we compare with the channel flow simulation of Moser, Kim, and Mansour (1999)). By altering the streamwise wavenumbers supporting the RNL turbulence, however, we obtain improved predictions. When the RNL system's dynamics is constrained to interactions between the streamwise mean flow ($k_x = 0$) and a single streamwise-varying wavenumber ($k_x = 7$), the peak normal Reynolds stress in the streamwise direction is reduced to ≈ 9 and occurs at $y^+ \approx 13$ for the $\mathrm{Re}_\tau = 180$ case. Permitting interactions with two additional wavenumbers, $k_x = 6$ and $k_x = 6.5$, yields a slight reduction to about 8.6 for the peak value, occurring at the same wall-normal location. In general, the peak values of the streamwise components of the normal Reynolds stresses for the single streamwise-varying wavenumber cases increase with increasing Re_τ. The wall-normal locations of these peak values change slightly to $y^+ \approx 14$ for both $\mathrm{Re}_\tau = 260$ and 340. As expected from

overall momentum conservation, the Reynolds shear stress profiles, shown in Figure 2.4(b), are quite realistic (since the mean velocity and hence the viscous stress distributions are realistic). Good agreement is obtained between the various band-limited RNL model cases at $\mathrm{Re}_\tau = 180$ and the channel flow DNS of Moser, Kim, and Mansour (1999) at the same friction Reynolds number.

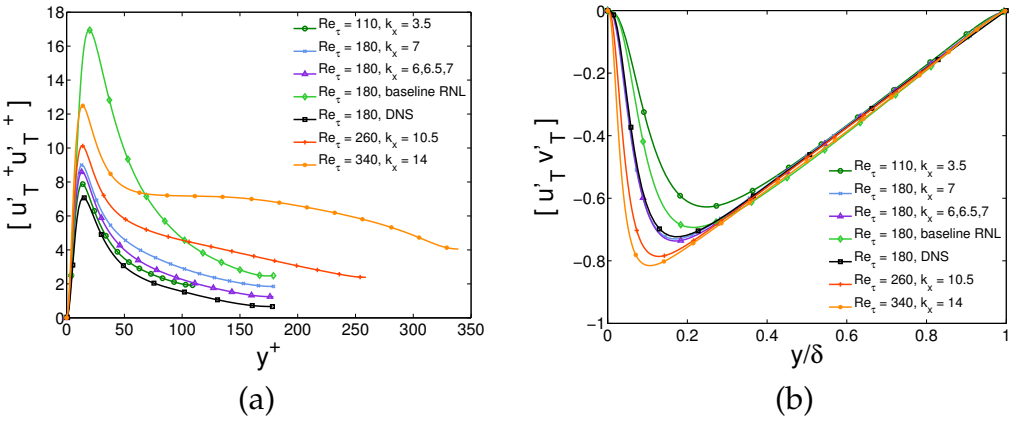

Figure 2.4: Profiles of (a) streamwise normal Reynolds stress (inner units) and (b) Reynolds shear stress (outer units). The superscript prime $'$ indicates departure from the time-averaged value. The DNS values are from the channel flow simulation of Moser, Kim, and Mansour (1999)

Finally, we focus on the transverse spatial structure of the fluctuations. Figure 2.2 already gave an indication that physically realistic structures are generated. More quantitatively, the spanwise spectra can be considered. The RNL case constrained to the single streamwise-varying wavenumber $k_x = 7$ is shown in Figure 2.5 at two distances from the wall, and compared to DNS. As can be seen, there is good agreement at small scales. The streamwise velocity spectra from RNL overestimates the DNS spectra at the largest scales while

underestimating the peak value which occurs at $k_z \sim 10$, while the spanwise and wall-normal velocity components generated by the RNL simulation underestimate the low wavenumber region of the spectra. Considering the simplicity of the RNL model compared to Navier-Stokes, it can be argued that there is good qualitative agreement in these spectra.

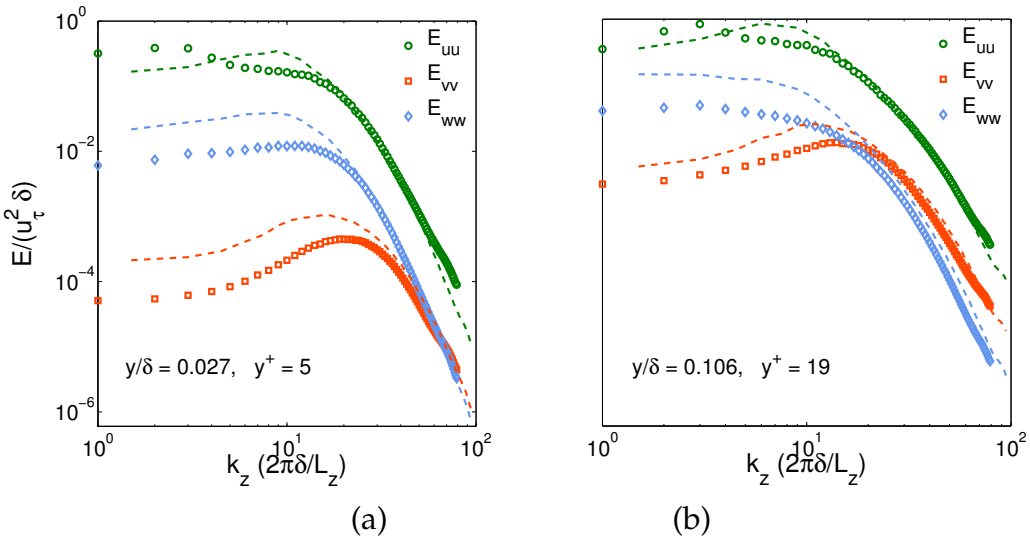

Figure 2.5: Spanwise energy spectra obtained from the band-limited RNL model at $\mathrm{Re}_\tau = 180$, at two wall-normal locations. The RNL system is constrained to a single perturbation wavenumber of $k_x = 7$. Dashed lines are channel flow DNS data from Moser, Kim, and Mansour (1999) Symbols are RNL data.

Chapter 3

Large eddy simulations of the restricted nonlinear system

3.1 Introduction

In section 3.2 we introduce the equations of motion, with the original RNL system in section 3.2.1 and the newly-proposed RNL-LES system in section 3.2.2. Our numerical approach is described in section 3.3. The simulation parameters and implementation details are described at the beginning of section 3.4. We then present the results and analysis of simulations of the baseline RNL-LES system in section 3.4.1, drawing comparisons to the previously studied DNS-RNL system. In section 3.4.2 we analyze reference LES data, which is then used to inform our simulations of the band-limited RNL-LES system, presented in section 3.4.3. The main contents of this chapter have appeared in the paper by Bretheim, Meneveau, and Gayme (2018a).

3.2 Restricted nonlinear equations for wall-bounded turbulence

In this section, we first present the RNL model (section 3.2.1) along with its associated state variable decompositions and notation. We then present the newly-formulated RNL-LES model (section 3.2.2). Unlike in the previous chapter, in this chapter we find it more suitable to present the equations in index notation. Accordingly, the relevant decompositions and equations are written once again, below, but now in index notation.

3.2.1 Restricted nonlinear model

The RNL system is derived by first decomposing the respective total velocity and pressure fields into streamwise-averaged components and streamwise-varying ('perturbation') components, as follows:

$$u_i^{tot}(x,y,z,t) = U_i(y,z,t) + u_i(x,y,z,t), \tag{3.1a}$$

$$= \left\langle u_i^{tot} \right\rangle_x \quad + u_i(x,y,z,t), \tag{3.1b}$$

$$p^{tot}(x,y,z,t) = P(y,z,t) + p(x,y,z,t), \tag{3.1c}$$

$$= \left\langle p^{tot} \right\rangle_x \quad + p(x,y,z,t), \tag{3.1d}$$

where the (x,y,z) coordinates refer to the streamwise, wall-normal, and spanwise directions, respectively, and the angle brackets $\langle\cdot\rangle_x$ represent the streamwise-averaging operation: $\langle\phi\rangle_x(y,z,t) = \frac{1}{L_x}\int_0^{L_x}\phi(x,y,z,t)\,\mathrm{d}x$, for a scalar variable ϕ and for a channel of streamwise extent L_x. Similarly, we

use $\langle\cdot\rangle_z$ and $\langle\cdot\rangle_t$ to denote spanwise- and time-averaging. Square brackets $[\cdot]$ denote averaging in time and both horizontal directions. The velocity components in each of the three coordinate directions are written $u^{tot} = u_1^{tot}$, $v^{tot} = u_2^{tot}$, and $w^{tot} = u_3^{tot}$ for the streamwise, wall-normal, and spanwise velocities, respectively.

Using the decompositions of Equations (1a-d) and then neglecting the nonlinear interactions between perturbations, it is straightforward to derive the governing equations for the RNL system as:

$$\partial_t U_i + U_j \partial_j U_i + \partial_i P - \frac{1}{\mathrm{Re}} \partial_j \partial_j U_i = - \left\langle u_j \partial_j u_i \right\rangle_x + \partial_1 p_\infty \delta_{i1}, \tag{3.2a}$$

$$\partial_t u_i + U_j \partial_j u_i + u_j \partial_j U_i + \partial_i p - \frac{1}{\mathrm{Re}} \partial_j \partial_j u_i = 0, \tag{3.2b}$$

where $\partial_i U_i = \partial_i u_i = 0$ and $\partial_1 p_\infty \delta_{i1}$ represents the streamwise pressure gradient that forces the flow (δ_{ij} is the Kronecker delta). The full N-S system can be recovered from the RNL system simply by adding the terms $-(u_j \partial_j u_i - \left\langle u_j \partial_j u_i \right\rangle_x)$ to the right-hand side of Equation (3.2b). These terms represent the streamwise-varying components of the perturbation-perturbation nonlinearity. Only the streamwise-averaged portion of the perturbation-perturbation nonlinearity, $- \left\langle u_j \partial_j u_i \right\rangle_x$, is retained in the RNL system. Mathematically, it is only this restriction of the nonlinearity (a quasi-linearization), that distinguishes the RNL system from the N-S system. All of the differences between the observed behavior of the RNL system and the N-S system stem from this restriction.

3.2.2 Restricted nonlinear large eddy simulation model

In order to obtain a RNL system suitable for LES, we introduce, as usual in LES, a filtered velocity field, $\tilde{u}_i^{tot}$, as the coarse-grained part of the total velocity, u_i^{tot}. We then introduce a sub-grid scale stress tensor, $\tau_{ij}^{tot,R}$, to model the effects of the unresolved scales. The anisotropic part of the sub-grid scale stress tensor is $\tau_{ij}^{tot,r} = \tau_{ij}^{tot,R} - \frac{1}{3}\tau_{kk}^{tot,R}\delta_{ij}$ and is approximated by the Smagorinsky model (Smagorinsky 1963),

$$\tau_{ij}^{tot,r} = -2\,\nu_T\,\tilde{S}_{ij}, \tag{3.3}$$

where $\tilde{S}_{ij} = \frac{1}{2}(\partial_j \tilde{u}_i^{tot} + \partial_i \tilde{u}_j^{tot})$ is the symmetric part of the filtered velocity gradient tensor and the eddy viscosity is given by:

$$\nu_T = \lambda_{\mathrm{SGS}}^2 |\tilde{S}|. \tag{3.4}$$

Here we define the characteristic strain rate using a horizontal average as follows:

$$|\tilde{S}| = \sqrt{2\left\langle \tilde{S}_{ij}\tilde{S}_{ij}\right\rangle_{x,z}}. \tag{3.5}$$

The Smagorinsky lengthscale λ_{SGS}, which represents the sub-grid scale mixing length, is determined by the Smagorinsky coefficient, C_s, and a non-dimensional filter width, Δ, modified by a wall-damping function such that

$$\lambda_{\mathrm{SGS}} = C_s\Delta = \left[\left(\frac{1}{C_0\Delta}\right)^n + \left(\frac{1}{\kappa(y+y_0)}\right)^n\right]^{-1/n}, \tag{3.6}$$

with the wall-damping exponent taken as $n = 2$. Far from the wall, the mixing lengthscale is approximately $\lambda_{\mathrm{SGS}_0} = C_0\Delta$, while close to the wall it tends to κy, where κ is the von Kármán constant. The filter width Δ is defined and

discussed in more detail in section 3.4.

The wall region is modeled by prescribing the stresses in accordance with the log law according to

$$\tau_{i,3}^{tot,w} = -\left(\frac{\tilde{u}_r\,\kappa}{\ln(y_1/y_0)}\right)^2 \frac{\tilde{u}_i^{tot}(x,y_1,z)}{\tilde{u}_r}, \tag{3.7a}$$

$$\tilde{u}_r = \sqrt{\left\langle \tilde{u}_1^{tot}(x,y_1,z)^2 + \tilde{u}_2^{tot}(x,y_1,z)^2 \right\rangle_{x,z}}, \tag{3.7b}$$

where y_0 is the prescribed roughness length, y_1 is the height of the first grid-point above the modeled wall, and $i = 1,2$. More details on this standard equilibrium wall model can be found in Schmidt and Schumann (1989) and Albertson (1996). Our implementation differs from Albertson's in that we calculate a horizontal average in Equation (4.5b), in order to maintain consistency with the horizontally-averaged characteristic strain rate in Equation (3.5).

The final set of simulated equations, which we refer to as the RNL-LES model, can now be written as:

$$\partial_t \tilde{U}_i + \tilde{U}_j\partial_j\tilde{U}_i + \partial_i\tilde{P}_\star - \frac{1}{\mathrm{Re}}\partial_j\partial_j\tilde{U}_i = -\left\langle \tilde{u}_j\partial_j\tilde{u}_i\right\rangle_x - \partial_j\left\langle \tau_{ij}^{tot,r}\right\rangle_x + \partial_1\tilde{p}_\infty\delta_{i1}, \tag{3.8a}$$

$$\partial_t\tilde{u}_i + \tilde{U}_j\partial_j\tilde{u}_i + \tilde{u}_j\partial_j\tilde{U}_i + \partial_i\tilde{p}_\star - \frac{1}{\mathrm{Re}}\partial_j\partial_j\tilde{u}_i = -\partial_j\tau_{ij}^r, \tag{3.8b}$$

along with $\partial_i\tilde{U}_i = \partial_i\tilde{u}_i = 0$. The residual stress term has been decomposed into its streamwise-averaged and fluctuating parts:

$$\tau_{ij}^r = \tau_{ij}^{tot,r} - \left\langle \tau_{ij}^{tot,r}\right\rangle_x. \tag{3.9}$$

The modified pressure, $\tilde{p}_\star^{tot} = \tilde{P}_\star + \tilde{p}_\star$, includes the isotropic part of the

sub-grid stress tensor, $\frac{1}{3}\tau_{kk}^{tot,R}$.

3.3 Numerical approach

To simulate the RNL-LES system, we have adapted a research code which has been previously used for direct numerical simulations of the RNL system (Bretheim, Meneveau, and Gayme 2015), as well as for many LES studies of wall-bounded turbulence (see, e.g. Calaf, Meneveau, and Meyers 2010; Graham and Meneveau 2012; VerHulst and Meneveau 2014). The wall-normal (y) direction is discretized with a centered second-order finite difference scheme while the horizontal directions (x and z) are pseudospectral. We use the second-order Adams-Bashforth method for time advancement with dynamic timestepping, subject to the requirement that the maximum Courant number at any point in the domain be less than 0.05 at every timestep. We employ a wall model (Equation (3.7)) at the bottom boundary with imposed wall stress. The top boundary has stress-free and zero normal velocity conditions and the horizontal directions are periodic. We dealias the advective term with the 3/2 rule as required by the pseudospectral methods and the vertical grid-spacing is uniform.

We now discuss a computationally efficient means of implementing the RNL-LES model by first demonstrating the reduced streamwise-varying wavenumber support of the RNL-LES dynamics. To facilitate this dicussion, we define the non-dimensional streamwise wavenumbers (or Fourier modes) as $k_{x,n} = n(2\pi H/L_x)$, where n is a nonnegative integer and H is the

domain height (used for non-dimensionalization). We refer to the n^{th} streamwise Fourier mode as $k_{x,n}$. The corresponding non-dimensional streamwise wavelengths are $\lambda_{x,n} = 2\pi/k_{x,n}$. Therefore, the streamwise-averaged velocity corresponds to the $k_{x,n=0}$ Fourier mode and the perturbations correspond to the $k_{x,n\neq 0}$ Fourier modes. The spanwise wavenumbers ($k_{z,n}$) and wavelengths ($\lambda_{z,n}$) are similarly defined. We also define the average perturbation kinetic energy associated with each wavenumber $k_{x,n}$ as:

$$E(k_{x,n},t) = \frac{1}{2}\frac{1}{L_y L_z}\int_0^{L_z}\int_0^{L_y} \tilde{u}_i''(k_{x,n},y,z,t)\tilde{u}_i''^{*}(k_{x,n},y,z,t)\,\mathrm{d}y\,\mathrm{d}z, \qquad (3.10)$$

where $\phi'' = \phi - \langle\phi\rangle_z$.

In order to illustrate the differences in the streamwise wavenumber support of the LES and baseline RNL-LES systems, we present two representative time histories of the average perturbation kinetic energy in Figure 3.1 for LES and RNL-LES (cases L-1 and B-1, respectively, which are fully described later in Table 3.1). Each case uses the same initial condition, which is a rough-wall logarithmic law for the mean velocity to which random noise sampled from a uniform distribution has been added. The two simulations use the same number of grid points, and thus have the same number of possible streamwise wavenumbers. However, the time history of the average perturbation kinetic energy (Figure 3.1) reveals that while LES will sustain energy in every resolved streamwise mode (after initial transients have died out), the RNL-LES only sustains a fraction of the resolved modes, with every mode above some cutoff frequency decaying to zero.

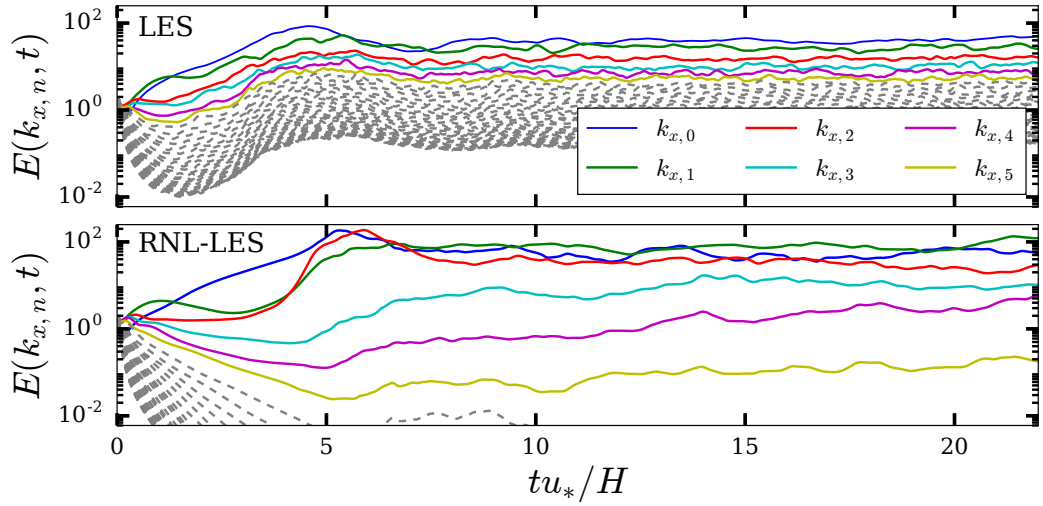

Figure 3.1: Time histories of average perturbation kinetic energy (defined in Equation (3.10)) for different $k_{x,n}$ modes: LES case L-1 and baseline RNL-LES case B-1 (see Table 3.1). For these cases, the $k_{x,n}$ modes with $n > 5$ (plotted with dashed gray lines) are sustained indefinitely in the LES system but rapidly decay to zero (after the transients die out) in the RNL-LES system and remain there even as turbulence is sustained.

The reduced streamwise wavenumber support of RNL-LES is consistent with prior simulations of the RNL system (Constantinou et al. 2014; Bretheim, Meneveau, and Gayme 2015; Thomas et al. 2015) and is a consequence of the restriction of the convective nonlinearity in the equation for the perturbations (Equation (4.2b)). Bretheim, Meneveau, and Gayme (2015) report a natural support of only six streamwise wavenumbers in a half-channel at $Re_\tau = 180$ while Constantinou et al. (2014) report a natural support of seven streamwise wavenumbers in a full channel at $Re_\tau = 950$. As will be explored in the context of RNL-LES later in this chapter and as previously summarized in the introduction, the RNL system can still support self-sustaining turbulence even when restricted to a single nonzero streamwise wavenumber interacting with

the mean flow (Thomas et al. 2015; Bretheim, Meneveau, and Gayme 2015; Farrell et al. 2016). With proper band-limiting of streamwise wavelengths, the resulting statistics compare favorably with those obtained by DNS of the full N-S system at low to moderate Reynolds numbers (Bretheim, Meneveau, and Gayme 2015).

The relatively small number of streamwise Fourier modes supported by the RNL and RNL-LES systems (compared to LES of the filtered N-S equations) motivates a mathematical description of the RNL model solely in Fourier space for the streamwise direction. To this end, we write the total velocity as a Fourier series over the finite interval $0 \leq x < L_x$:

$$\tilde{u}_i^{tot}(x,y,z,t) = \frac{1}{\sqrt{L_x}} \sum_{n \in \mathcal{S}_{N_x}} \tilde{u}_i^{(n)}(y,z,t) \exp(ik_{x,n}x), \tag{3.11}$$

where $\tilde{u}_i^{(n)} = L_x^{-1/2} \int_0^{L_x} \exp(-ik_{x,n}\xi)\ \tilde{u}_i^{\text{tot}}(\xi,y,z,t)\ \mathrm{d}\xi$ are the complex Fourier coefficients. The set $\mathcal{S}_{N_x}$ is the set of streamwise modes in the Fourier series and N_x is the number of streamwise modes in (cardinality of) the set. Note that the derivatives with respect to the streamwise direction are evaluated in Fourier space by multiplying the Fourier coefficients by $ik_{x,n}$; the total convective nonlinearity in the N-S equations can then be written as:

$$\tilde{u}_j^{tot}\partial_j\tilde{u}_i^{tot} = \frac{1}{L_x} \sum_{\substack{m \in \mathcal{S}_{M_x} \\ n \in \mathcal{S}_{N_x}}} [\tilde{u}^{(m)}(ik_{x,n})\tilde{u}_i^{(n)} + \tilde{v}^{(m)}\partial_y\tilde{u}_i^{(n)} + \tilde{w}^{(m)}\partial_z\tilde{u}_i^{(n)}]\ \mathrm{e}^{i(k_{x,m}+k_{x,n})}. \tag{3.12}$$

Equation (3.12) represents the full convective nonlinearity in the N-S system, where all $k_{x,m}$ modes interact with all $k_{x,n}$ modes. The RNL system restricts these interactions to those in which $m = 0$, $n = 0$, or $m + n = 0$.

The calculation of the nonlinearity (in $k_{x,n}$ Fourier space) is thus reduced from an $\mathcal{O}(N_x^2)$ operation (in DNS or LES) to an $\mathcal{O}(N_x)$ operation (in RNL or RNL-LES).

This drastic reduction in the number of interactions between modes and the fact that the RNL turbulence can be sustained by a single streamwise-varying mode interacting with the mean flow, make it feasible to simulate the equations with the streamwise direction represented only in the $k_{x,n}$ Fourier space (i.e., there is no need for a physical space streamwise grid). This approach eliminates the usual practice of computing the nonlinear terms in purely physical space which, even when using fast Fourier transforms (FFTs) to obviate the computationally expensive $\mathcal{O}(N_x^2)$ convolution, remains a significant cost. For the y-z cross-plane we maintain a physical space grid and thus we still compute FFTs for the spanwise (z) direction in the usual manner.

The ability to affordably simulate entirely in streamwise Fourier space is particularly advantageous in scenarios where we are only interested in simulating a small set of $k_{x,n}$ modes, say, e.g., $k_{x,0}$ and $k_{x,64}$. In the traditional pseudospectral approach, simulating the RNL system with these two streamwise modes would require a physical grid with $N_x > 2k_{x,\max}$ (or $N_x > 128$ in this example, with the corresponding set of 128 Fourier modes $\mathcal{S}_{N_x} = \{0, \pm 1, \ldots, \pm 63, 64\}$), even though we are only interested in two modes. The ability to simulate entirely in $k_{x,n}$ space, and simulating only the Fourier modes of interest, thus has the tremendous computational advantage of significantly lowering the memory requirements for storage of system variables (in addition to requiring fewer FFTs, since now only FFTs in the spanwise

direction are required).

While the particular nonlinear restriction inherent to the RNL system has interesting numerical advantages, it is important to also understand the physical interpretation of the restriction. Referring once again to Equation (3.12), we see that an interaction between mode m and n directly affects mode $p = m + n$ by either depositing or extracting energy in mode p. By restricting the nonlinear interactions to those where either $m = 0$, $n = 0$, or $m + n = 0$, we remove the mechanism by which new streamwise modes could be created. As such, only the $k_{x,n}$ modes specified in the initial condition can be present in the simulation. The different nonzero modes cannot interact directly with each other, but only indirectly through the $k_{x,0}$ mode via the $U_i u_i$ and $u_i U_i$ terms. As such, the restriction reduces the number of streamwise energy transfer pathways, requiring all streamwise energy transfer to be conducted through the zeroth streamwise Fourier mode.

In summary, two of the physical consequences of the nonlinear restriction inherent to the RNL system are:

1. Fewer streamwise modes are sustained relative to the N-S or LES systems.

2. As was demonstrated by previous numerical experiments (Thomas et al. 2015; Bretheim, Meneveau, and Gayme 2015), RNL turbulence self-sustains on a small number of nonzero streamwise modes (even as few as one) interacting with the zeroth streamwise mode.

These physical attributes of the RNL system thus enable the following

numerical simplifications:

1. Efficient convolution sums over the few remaining $k_{x,n}$ modes.
2. FFTs in the streamwise direction are obviated.
3. Computer memory usage is reduced by storing only the $k_{x,n}$ modes of interest.

In our implementation of the RNL-LES system, we have achieved measured wall time speedups as high as one order of magnitude relative to the corresponding LES system (computational speedups are further discussed in section 3.4.3).

3.4 Simulation descriptions and results

We now present the three groups of simulations considered in this chapter: the baseline RNL-LES (section 3.4.1), the LES reference data (section 3.4.2), which are used to parameterize the band-limited RNL-LES, and the band-limited RNL-LES results (section 3.4.3).

For all cases considered, the extent of the simulation domain is $[L_x, L_y, L_z]/H = [2\pi, 1, 2\pi]$. We focus on the case of very high Reynolds number flow, and therefore neglect the viscous terms in Equations (3.2a) and (3.2b). The bottom boundary condition is specified through the roughness length and the wall model's von Kármán constant, which are respectively set to y_0/H = 1.25e-5 and $\kappa = 0.4$. For all cases, the grid aspect ratio is fixed at $\Delta_z/\Delta_y = \pi$ and for the baseline RNL-LES and LES reference, we use

$\Delta_x/\Delta_y = \pi$ (note the Δ_x is not relevant to the band-limited RNL-LES cases, since there is no streamwise physical grid for those cases). All grid spacings discussed herein are non-dimensional (e.g., $\Delta_z = L_z/(HN_z)$).

Typical LES implementations of the Smagorinsky sub-grid scale model with a constant coefficient use C_0 in the range of 0.1 to 0.3 ($C_0 = 0.16$ is common), and $\Delta = \Delta_{3D} = (\Delta_x\Delta_y\Delta_z)^{1/3}$ is often used (Scotti, Meneveau, and Lilly 1993). Here we modify this value to account for the fact that the band-limited RNL-LES simulations use a two-dimensional physical space grid for the y-z cross-plane coupled with Fourier-space-only $k_{x,n}$ modes, which necessitates the use of a two-dimensional filter width, i.e., $\Delta = \Delta_{2D} = (\Delta_y\Delta_z)^{1/2}$. The two-dimensional physical grid also motivates the use of a horizontally-averaged $\tilde{S}_{ij}\tilde{S}_{ij}$ in the characteristic strain rate in Equation (3.5), since the non-averaged form cannot be calculated without transforming to a physical space grid in the streamwise direction. In order to maintain as much consistency as possible between the three simulation groups, we set $\Delta = \Delta_{2D}$ for all cases, even though the baseline RNL-LES and LES simulations use a three-dimensional grid in physical space. We set $C_0 = 0.23$, larger than 0.16, in order to compensate for the smaller filter width ($\Delta_{2D} < \Delta_{3D}$) and the horizontally-averaged characteristic strain rate.

For all three simulation groups, we study a range of grid sizes varying in cross-plane resolution from $[N_y, N_z] = [32, 64]$ to $[N_y, N_z] = [256, 512]$. As the number of grid points changes between cases, the only parameter affecting the resolved turbulence is the Smagorinsky lengthscale, λ_{SGS}, which decreases with increasing grid size and is effectively the smallest lengthscale in the

simulation. Since the range of possible lengthscales increases with increasing grid size (and decreasing λ_{SGS}), λ_{SGS} plays a role similar to that of inverse Reynolds number in DNS.

Finally, the band-limited RNL-LES data are produced using the computationally efficient numerical implementation described in the previous section. The baseline RNL-LES and LES data are produced using the standard FFT-based numerical framework since the numerical enhancements are unique to the band-limited RNL-LES system.

3.4.1 Baseline RNL-LES results

In Table 3.1 we summarize both the baseline RNL-LES and the LES cases that are respectively discussed in sections 3.4.1 and 3.4.2.

Label	$N_x = N_z$	N_y	$\lambda_{SGS_0} = C_0\Delta$
B-1, L-1	64	32	0.0125
B-2, L-2	128	64	0.0063
B-3, L-3	192	96	0.0042
B-4, L-4	256	128	0.0031
B-5, L-5	384	192	0.0021
B-6, L-6	512	256	0.0016

Table 3.1: Baseline RNL-LES and LES cases (labeled B- and L-, respectively). The lengthscale λ_{SGS_0} is effectively the smallest scale in the simulation and decreases with increasing grid size.

Figure 3.2 shows instantaneous cross-stream snapshot contours of streamwise velocity for a pair of representative baseline RNL-LES and LES cases. A comparison of panels (a) and (b) clearly demonstrates that the baseline RNL-LES lacks the small scale structures typically observed in LES at this

resolution and suggests that there are quantitative differences between the baseline RNL-LES results and the reference LES results.

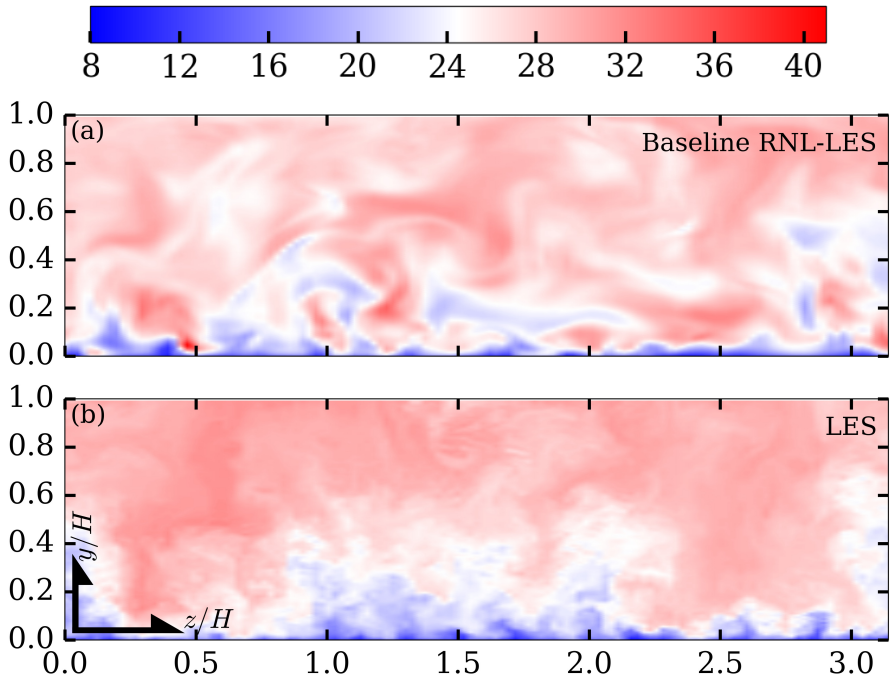

Figure 3.2: Instantaneous snapshot contours of streamwise velocity in the y-z cross-plane: (a) Baseline RNL-LES case B-4 and (b) LES case L-4. For display purposes, we plot half the channel width ($L_z/H = 2\pi$).

Figure 3.3 plots the mean velocity and streamwise Reynolds stress profiles for a representative subset of the baseline RNL-LES cases of Table 3.1. As in prior results at moderate Reynolds numbers (Constantinou et al. 2014; Bretheim, Meneveau, and Gayme 2015; Farrell et al. 2016), the mean velocity profiles significantly over-predict the expected logarithmic profile (in this case, the rough-wall log law) near the wall. In addition to being too large in magnitude, the baseline RNL-LES mean velocity profile becomes approximately logarithmic above a certain height (here in the region $y/H > 10^{-1}$), but the

curves level out at too flat a slope, an attribute which is consistent with prior results from the DNS-RNL system at lower Reynolds numbers (Constantinou et al. 2014; Bretheim, Meneveau, and Gayme 2015; Farrell et al. 2016). The LES reference data (case L-3) also over-predict the log law in much of the domain, but with an accurate slope – a result which is typical of the constant coefficient Smagorinsky sub-grid scale model (Porté-Agel, Meneveau, and Parlange 2000). Additionally, as λ_{SGS} decreases, the baseline RNL-LES mean velocity profiles grow increasingly worse in both their magnitudes and slopes; this trend is also consistent with the Reynolds number trends observed in prior RNL studies (Constantinou et al. 2014; Farrell et al. 2016).

The streamwise Reynolds stresses are likewise significantly over-predicted by the baseline RNL-LES dynamics, particularly in the bottom third of the channel; the results similarly become less accurate with decreasing λ_{SGS}. These results are again consistent with prior DNS studies of the RNL system (Constantinou et al. 2014; Bretheim, Meneveau, and Gayme 2015), which show increasingly less accurate second-order statistics with increasing value of Re_τ.

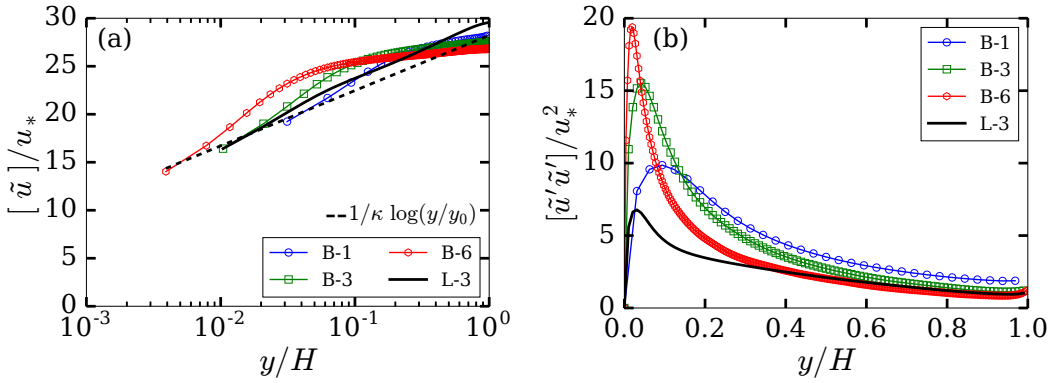

Figure 3.3: Baseline RNL-LES results (open symbols) compared to representative LES reference (case L-3, black line) data: (a) mean velocity profiles (b) streamwise Reynolds stress profiles. The superscript prime $'$ in the plot label indicates fluctuations about the time-averaged value.

As will be addressed below in section 3.4.3, these observed statistical inaccuracies in the baseline RNL-LES system can be addressed by appropriately restricting (i.e., band-limiting) the active streamwise wavenumbers supporting the dynamics, as in Bretheim, Meneveau, and Gayme (2015). In that work, the band-limiting was accomplished by selecting the streamwise wavenumbers empirically. More specifically, the authors ran many simulations over a range of candidate streamwise wavenumbers at different Reynolds numbers. They then integrated the resulting mean velocity profiles to compute the corresponding skin-friction coefficients and identified an optimal streamwise wavenumber at each Reynolds number that minimized the error in the skin-friction coefficient. Repeating this process over a range of Reynolds numbers led the authors to postulate that the optimal streamwise wavenumber asymptotes to a constant value that scales in inner units and corresponds to an important small scale lengthscale of roughly 150 viscous units. Restricting

the RNL streamwise dynamics to the single important streamwise lengthscale of 150 viscous units led to significantly improved turbulence statistics and spectra over the entire simulated range of low to moderate Reynolds numbers ($Re_\tau = 110$ to $Re_\tau = 340$).

This streamwise lengthscale of 150 viscous units falls in the middle of the range of peak 'surrogate dissipation' for a full-channel DNS at $Re_\tau = 2000$ (see Jiménez 2012, for details). A similar argument, but applied in the context of LES, could serve as a guide as to which streamwise modes to retain in the band-limited RNL-LES system such that the advection of mean velocity is balanced by the viscous (or sub-grid) dissipation. This hypothesis is tested in the next section, which examines LES data with a range of different mixing lengths. The resulting data will be used to inform the band-limited RNL-LES simulations of section 3.4.3.

3.4.2 LES cases

We now present results for the LES (cases L-1 through L-6) described in Table 3.1. We first present statistical analyses of these LES results using various spectra. In Figure 3.4 we plot the premultiplied vorticity spectra, defined as $k_{x,n}(E_{\omega_x\omega_x} + E_{\omega_y\omega_y} + E_{\omega_z\omega_z})$, for all six cases.

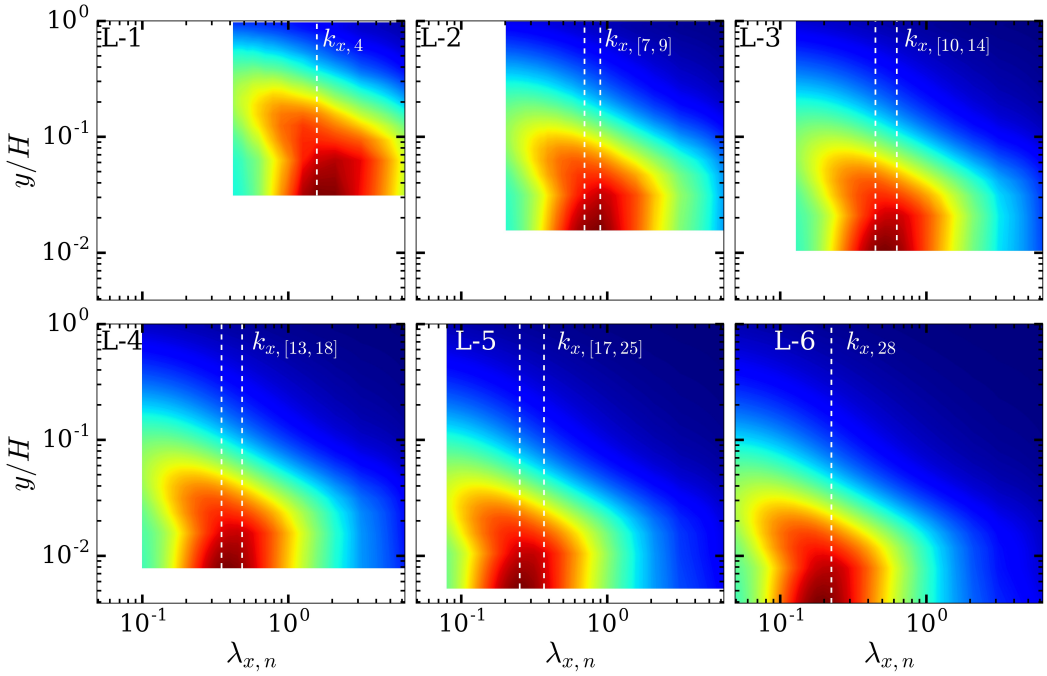

Figure 3.4: Premultiplied vorticity spectra, $k_{x,n}(E_{\omega_x\omega_x} + E_{\omega_y\omega_y} + E_{\omega_z\omega_z})$. Each plot is normalized by its own maximum value. The colorbars are the same for each panel (0 to 1, blue to red).

These plots show that the range of streamwise wavenumbers over which peak dissipation occurs in the LES shifts to smaller and smaller scales as the grid scale λ_{SGS_0} of the LES is reduced. The normalized streamwise wavelengths ($\lambda_{x,n}/\lambda_{\mathrm{SGS}_0} = 2\pi/(k_{x,n}\lambda_{\mathrm{SGS}_0})$) associated with the streamwise wavenumbers corresponding to the range of peak values of the dissipation spectra for cases L-1 through L-5 are plotted against N_y in Figure 3.5, where the range of wavelengths associated with the peak are indicated by the shaded grey regions. The solid black circle markers correspond to the discrete $k_{x,n}$ modes identified in Figure 3.4 for each case (e.g., $k_{x,4}$ for L-1 with $N_y = 32$

which corresponds to $\lambda_{x,4}/\lambda_{\mathrm{SGS}_0} \approx 125$) while the hollow black circles correspond to the nearest discrete $k_{x,n}$ modes just outside the peak range identified in Figure 3.4 (e.g., for L-1, $k_{x,3}$ and $k_{x,5}$ are nearest the key mode of $k_{x,4}$). This plot identifies the range of scales $\lambda_{x,n}/\lambda_{\mathrm{SGS}_0} = [100, 180]$, which is consistent with the dissipation range $\lambda_x^+ = [100, 200]$ in the work by Jiménez (2012), where the plus sign denotes viscous units. The important small scale of $\lambda_x^+ = 150$, identified in Bretheim, Meneveau, and Gayme (2015), is represented by the dashed red line. This plot also indicates that as the system size (LES resolution that is indicated here simply by N_y) increases (and λ_{SGS} decreases), the dissipation range includes an increasing number of $k_{x,n}$ modes. As the LES resolution improves (and thus, the separation of scales increases), the dissipation range shifts to smaller scales. As the dissipation range shifts to smaller scales, an increasingly larger number of streamwise Fourier modes span the dissipation range.

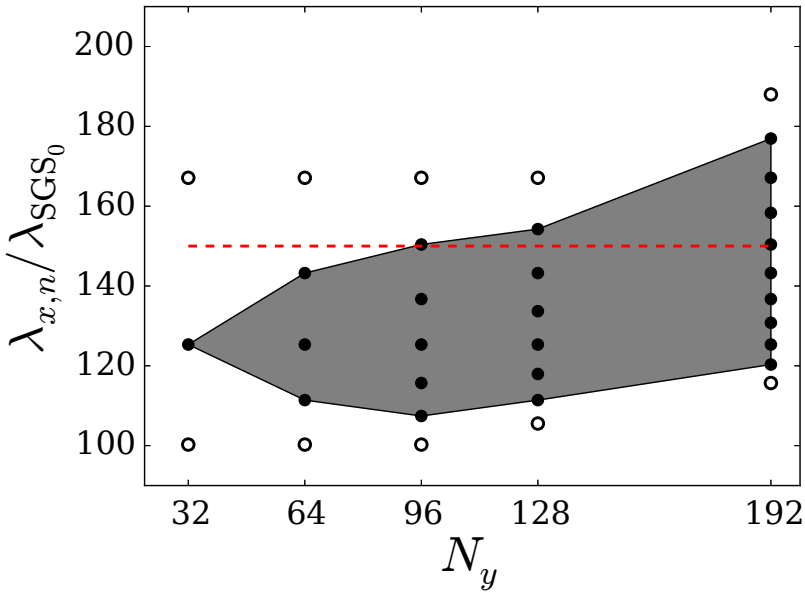

Figure 3.5: Normalized streamwise wavelengths (solid black circles) corresponding to the streamwise wavenumbers identified in Figure 3.4. The hollow black circles correspond to the nearest discrete wavelengths just outside the peak range identified in Figure 3.4. The dashed red line represents the optimized wavelength in viscous units ($\lambda_x^+ = 150$) identified in the DNS-RNL system (Bretheim, Meneveau, and Gayme 2015).

The scaling of λ_{SGS} is easily understood from its definition (recall that far from the wall, $\lambda_{\mathrm{SGS}} \approx \lambda_{\mathrm{SGS}_0} = C_0\Delta$). Since $\Delta \sim (N_y N_z)^{-1/2}$, each quadrupling of the cross-plane grid size $(N_y N_z)$ results in a halving of λ_{SGS_0} and a corresponding doubling of the $k_{x,n}$ associated with λ_{SGS_0}. This trend is observable in other quantities, for example those shown in Figure 3.6, which plots premultiplied wall-normal vorticity spectra in the streamwise direction and premultiplied energy spectra in the spanwise direction. Each quadrupling of the grid size results in a factor of two shift of peak values to smaller scales (higher wavenumbers).

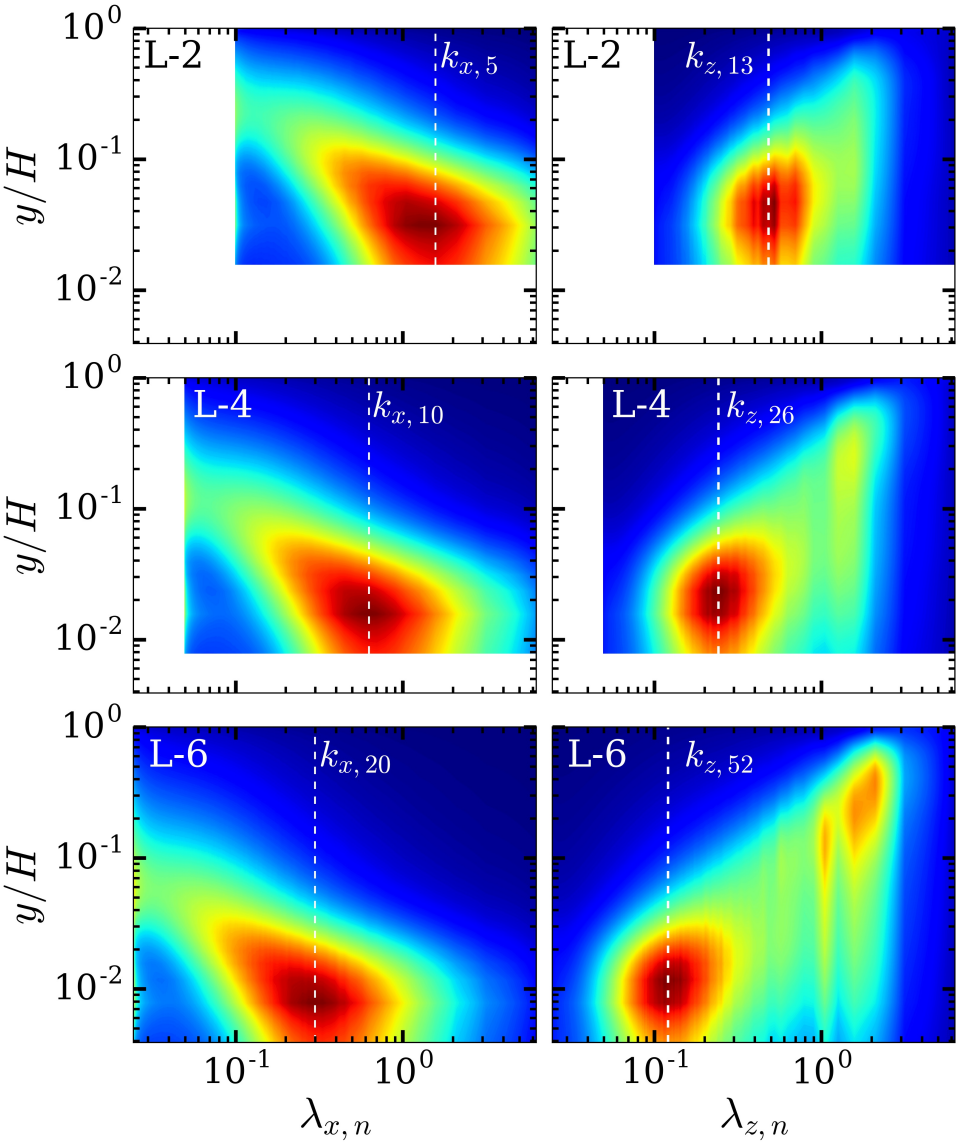

Figure 3.6: LES results. Left column: premultiplied wall-normal vorticity streamwise spectra, $k_{x,n}(E_{\omega_y\omega_y})$. Right column: premultiplied streamwise velocity energy spanwise spectra, $k_{z,n}(E_{uu})$. Each plot is normalized by its own maximum value. Cases: L-2 (top), L-4 (middle), L-6 (bottom). The colorbars are the same for each panel (0 to 1, blue to red).

Figure 3.7 plots the premultipled spanwise energy spectra for all of the

LES cases in Table 3.1. The $k_{z,n}$ value associated with the peak in these spectra doubles as N_y and N_z each double (or $N_y N_z$ quadruples); this scaling is also observed in Figure 3.6. In Figure 3.7 we also see the emergence of a second peak as $N_y N_z$ increases. This large scale begins to appear in case L-4 and is readily apparent in cases L-5 and L-6. Case L-6 additionally hints at the emergence of a third distinct peak, albeit a weak one. It is this separation of scales in the channel cross-plane which motivates including multiple bands or levels in the band-limited RNL-LES discussed in the next section.

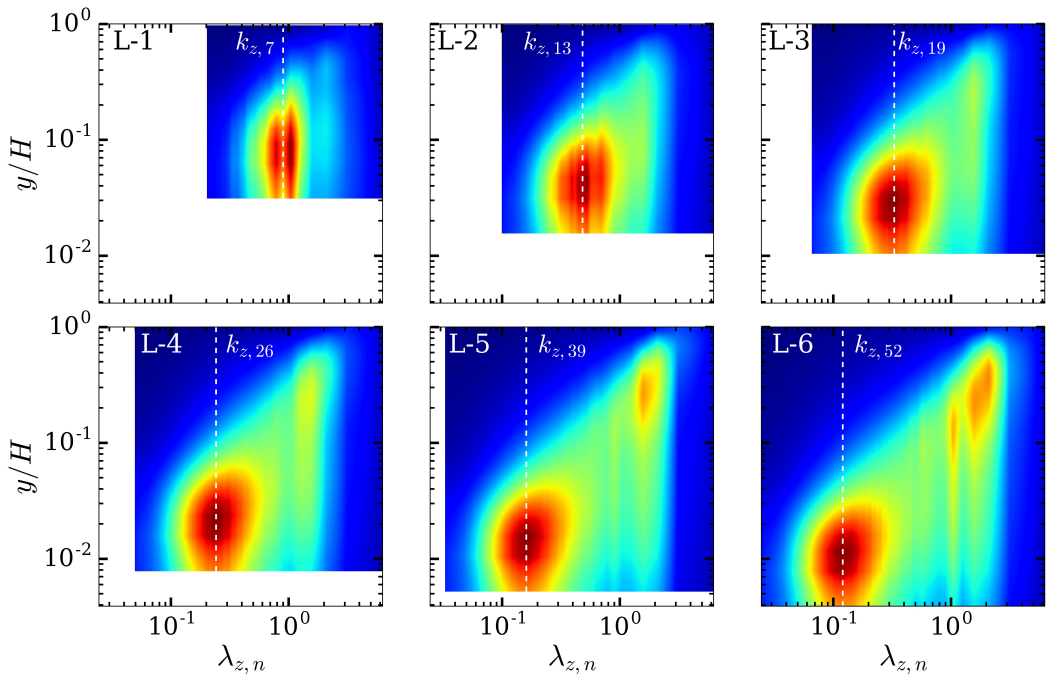

Figure 3.7: Premultiplied one-dimensional spanwise energy spectra $(k_{z,n}E_{uu})$ for LES. The colorbars are the same for each panel (0 to 1, blue to red).

3.4.3 Band-limited RNL-LES cases

We now examine whether the important streamwise wavenumbers predicted by the LES in the previous section can be used to inform the selection of modes simulated in the band-limited RNL-LES system. Table 3.2 summarizes the band-limited RNL-LES cases, where the selected streamwise wavenumbers correspond to those identified in Figure 3.4. The labels used here correspond numerically to those used in Table 3.1, e.g., case R-3 is meant to be compared directly to cases L-3 and B-3. The simulation cases in this table are implemented in the manner described at the beginning of section 3.4, where the simulation domain consists of a physical grid in the y-z cross-plane along

with a subset of $k_{x,n}$ modes (the 'band-limited' modes) which live only in the spectral Fourier space. We thus only report the y-z grid points in Table 3.2. We first consider the results in the 'Regime I' column, which will be fully explained and distinguished from 'Regime II' later in this section. We consider cases R-4 and R-5 to be 'overlap' cases in that the statistics are reasonably approximated in both Regimes I and II. The bracketed values (i) and (ii) in the labels for R-4 and R-5 refer respectively to Regimes I and II.

Label	N_z	N_y	$\lambda_{\mathrm{SGS}_0} = C_0\Delta$	$k_{x,n}$ (Regime I)	$k_{x,n}$ (Regime II)
R-1	64	32	0.0125	4	—
R-2	128	64	0.0063	7-9	—
R-3	192	96	0.0042	10-14	—
R-4(i)	256	128	0.0031	13-18	—
R-4(ii)	256	128	0.0031	—	7, 14
R-5(i)	384	192	0.0021	17-25	—
R-5(ii)	384	192	0.0021	—	7, 21
R-6	512	256	0.0016	—	7, 28
R-7	768	384	0.0010	—	7, 42

Table 3.2: Band-limited RNL-LES cases.

Figure 3.8 shows instantaneous cross-stream snapshot contours of streamwise velocity for case R-4(i). The velocity shows clear improvement over the corresponding baseline RNL-LES result (case B-4 in Figure 3.2(a)), with the presence of fine-scale structures more similar to those of LES at this cross-plane resolution in Figure 3.2(b).

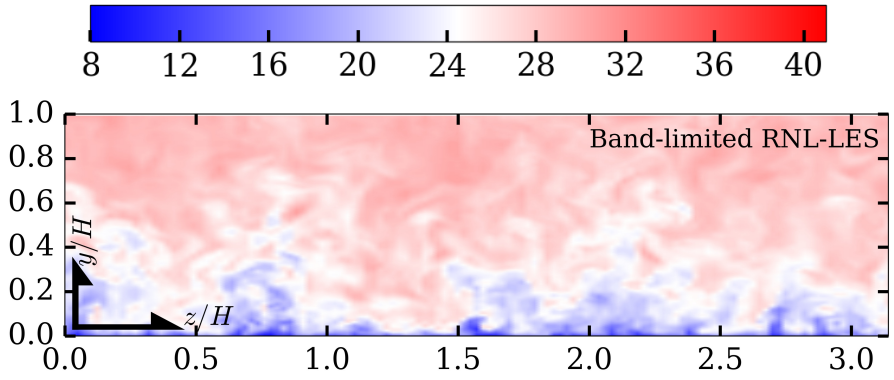

Figure 3.8: Instantaneous snapshot contours of streamwise velocity in the y-z cross-plane: band-limited RNL-LES case R-4(i). For display purposes, we plot half the channel width ($L_z/H = 2\pi$).

Figure 3.9(a) shows the mean velocity profiles resulting from the band-limited RNL-LES cases in Regime I of Table 3.2. The mean velocity profiles show significantly better agreement with the correct log law than do their corresponding baseline RNL-LES cases (see Figure 3.3). Likewise, the corresponding streamwise Reynolds stresses compare much more favorably to LES. Referring to Figure 3.9(b), the peak Reynolds stresses have fallen to a value of approximately 8 whereas the baseline RNL-LES Reynolds stresses peaked at a value closer to 18. These results validate our proposed method of selecting the $k_{x,n}$ 'bands' by referencing the regions of peak dissipation in LES (Figure 3.4). By shifting the active lengthscales away from those naturally supported by the baseline RNL-LES system to those scales associated with the dissipation range of the LES system, we achieve a properly band-limited RNL-LES system with significantly improved turbulence statistics.

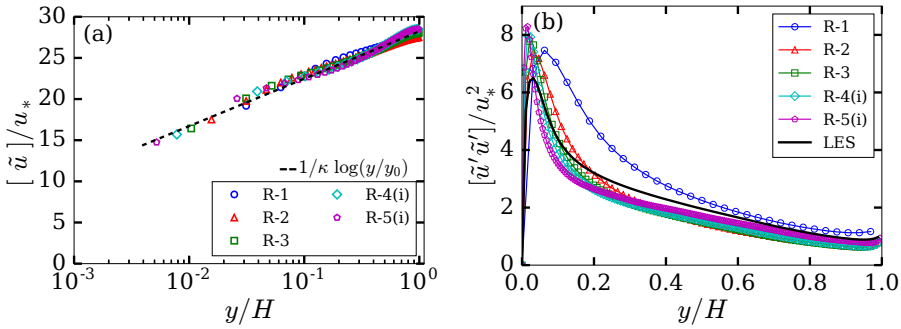

Figure 3.9: Band-limited RNL-LES mean velocity and streamwise Reynolds stress profiles (Regime I cases). The superscript prime $'$ in the plot labels indicates fluctuations about the time-averaged value. Note: for clearer data presentation, the plot markers in panel (a) are sparsened and do not indicate grid resolution.

It is clear that the selected range of streamwise wavelengths has a significant effect on the accuracy of the band-limited RNL-LES results. In order to investigate the sensitivity of these results to the selected range of streamwise wavelengths, we consider a representative case (R-1 of Table 3.2, which required only a single nonzero streamwise wavenumber) and vary the chosen streamwise wavenumber. Figure 3.10 shows that the resulting mean velocity profiles depend strongly on the chosen streamwise wavenumber, consistent with prior work in the DNS setting (Bretheim, Meneveau, and Gayme 2015; Thomas et al. 2015). The magnitude of the mean velocity increases with increasing streamwise wavenumber and eventually even surpasses the baseline RNL-LES mean velocity profile. For this particular case, setting n in the range of 3 to 5 results in a reasonable mean velocity profile. We took $n = 4$ as our representative case (case R-1 of Table 3.2). We also note that case R-1 is the most sensitive to changes in the selected streamwise wavelength since it has

just a single nonzero streamwise wavelength interacting with the mean flow. The other cases, which involve a range of streamwise wavelengths, are less sensitive to the particular set of wavelengths chosen, so long as the chosen range reasonably spans the range of peak wavelengths identified in Figure 3.4, the precise upper and lower bounds of which are arbitrary.

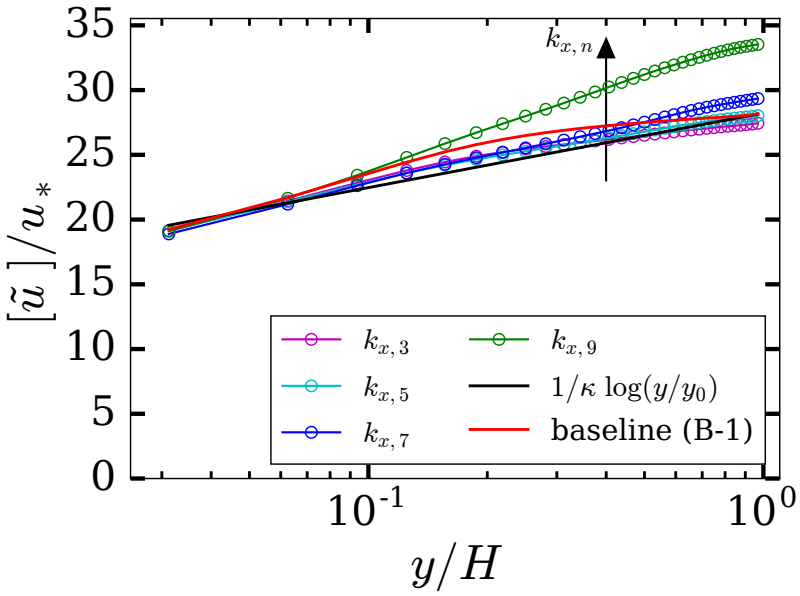

Figure 3.10: Mean velocity profiles of variants of case R-1 of Table 3.2. Variations about the optimized single nonzero streamwise wavenumber ($k_{x,4}$) illustrate the sensitivity of the results to the chosen $k_{x,n}$.

The band-limiting procedure of the Regime I cases clearly improves the resulting profiles of the first- and second-order statistics in the RNL-LES system. We can also observe an improvement in terms of the resulting cross-plane scales by examining the premultiplied one-dimensional spanwise energy spectra. In Figure 3.11 we see a marked difference between the energetic

spanwise scales of baseline RNL-LES compared to LES and band-limited RNL-LES. The baseline RNL-LES naturally sustains only a reduced number of streamwise modes (from $k_{x,0}$ up through some cutoff wavenumber). The resulting dynamics existing on this natural set of low $k_{x,n}$ modes affects a change in the spanwise $k_{z,n}$ modes, shifting their energy to larger scales. This effect is also apparent in Figure 3.8, where the baseline RNL-LES instantaneous cross-plane snapshot contours of streamwise velocity are smoother and larger scale than those of the corresponding LES. The band-limiting procedure, which shifts the $k_{x,n}$ modes into the appropriate dissipation range, is able to correct this spanwise shifting effect, returning the energy spectra peak locations back to their LES-observed values.

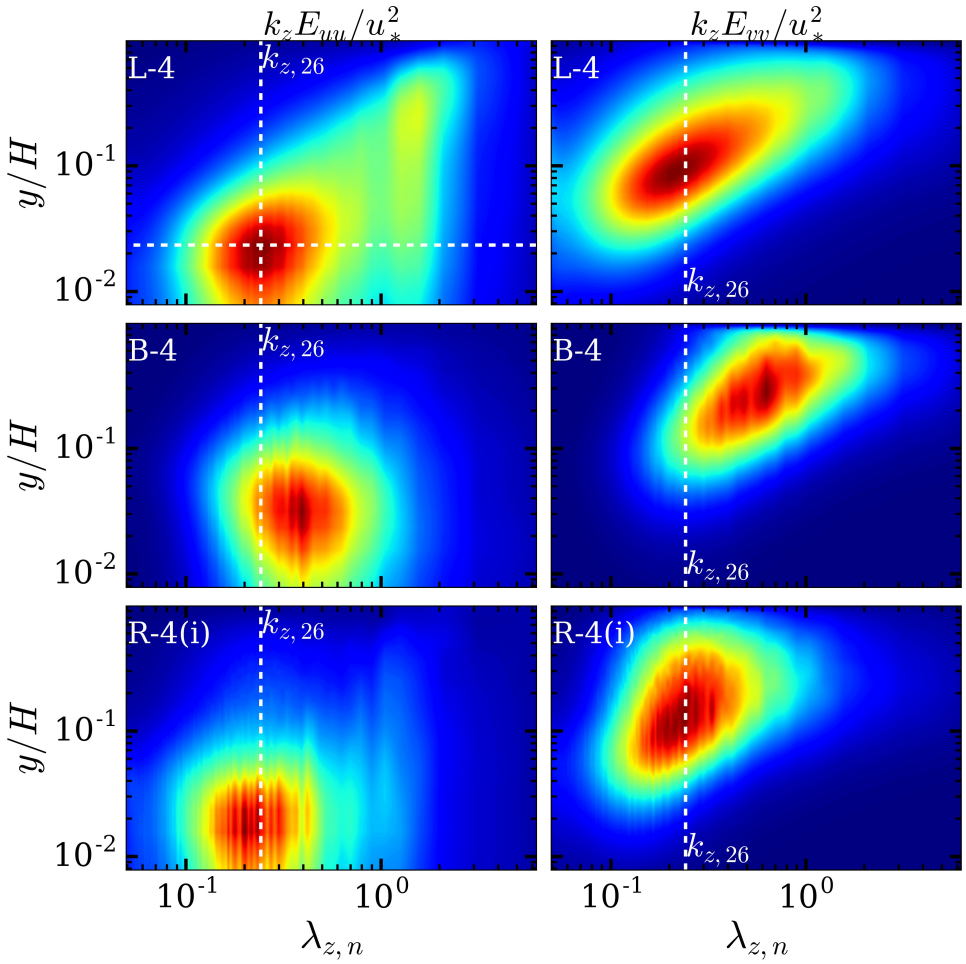

Figure 3.11: Comparison of premultiplied one-dimensional spanwise energy spectra for LES (top row), baseline RNL-LES (middle row), and band-limited RNL-LES (bottom row). The left column shows the energy in the streamwise component of velocity while the right column shows the energy in the wall-normal component of velocity. The colorbars are the same for each panel (0 to 1, blue to red).

Additionally, we can connect the spanwise structures ($k_{z,n}$ modes) to the streamwise structures ($k_{x,n}$ modes) by examining premultiplied two-dimensional energy spectra. Referring to the top left panel of Figure 3.11, the high spanwise wavenumber peak of $k_{z,26}$ occurs at a height of $y/H \sim 0.02$.

Figure 3.12 plots the premultiplied two-dimensional energy spectra of spanwise velocity ($k_x k_z E_{ww}$) at this height. These two-dimensional spectra illustrate the connection between key spanwise and streamwise lengthscales. The vertical dashed lines in this plot correspond to the wavenumber limits chosen for the corresponding RNL-LES simulation (case R-4(i)), which retained streamwise wavenumbers ranging from $k_{x,13}$ to $k_{x,18}$. The streamwise lengthscales of this range correspond well to the peak near-wall spanwise lengthscale of $\lambda_{z,26} = 2\pi/k_{z,26}$.

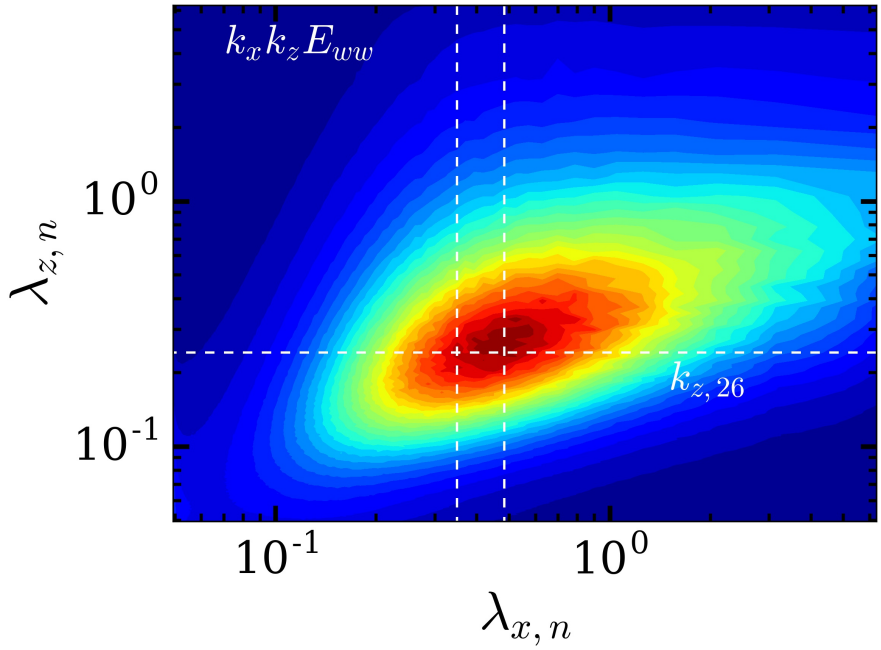

Figure 3.12: Premultiplied two-dimensional spanwise energy spectra for LES (case L-4) at $y/H \sim 0.02$. Values normalized by in-plane maximum (colorbars are 0 to 1, blue to red). Vertical dashed lines correspond to the streamwise wavelengths associated with $k_{x,13}$ and $k_{x,18}$.

The Regime I cases of Table 3.2 were obtained by simulating only streamwise wavenumbers associated with the region of peak premultiplied vorticity spectra (plus $k_{x,0}$) in the corresponding LES (Figure 3.4). These nonzero streamwise wavenumbers correspond to the dissipative small scales for each grid size. We select a range of scales about this one small scale in order to suitably span the dissipation range, a range which increases with increasing grid size. As the grid size increases, however, a distinct large scale emerges (see Figure 3.7). This scale is larger than the dissipation range scale and appears not to change much with changing grid resolution. The emergence of this large scale is not unexpected, as larger grids entail more scale separation due to the

higher resolution in the y-z cross-plane.

These observations motivate the addition of a large scale in the band-limited RNL-LES simulations on larger grids. In fact, as the grid size increased beyond that of case R-5(i), with $[N_y, N_z] = [192, 384]$, we were unable to obtain realistic turbulence statistics by only including streamwise wavenumbers associated with the dissipative small scales. By introducing a large streamwise scale (lower wavenumber), while still retaining a dissipative small scale, we again recovered realistic turbulence statistics. We identify this large scale as $k_{x,7}$, which is the first streamwise Fourier mode to have a wavelength smaller than the height of the half-channel ($\lambda_{x,7} = 2\pi/7 < L_z$). We distinguish the larger grid cases, requiring both a large and small scale, as Regime II.

In our first attempt to include a large scale ($k_{x,7}$) in the band-limited RNL-LES system, we found the resulting mean velocity to be too high in magnitude in the region $y/H < 0.1$. This initial attempt is labelled case R-5(ii*) and the results are plotted in Figure 3.13(a), where it is clear that the mean flow is too fast near the wall, albeit the overall profile is still more accurate than that of the baseline RNL-LES result (case B-5). When a large scale such as $k_{x,7}$ is included among smaller scales in the RNL-LES system, it tends to dominate and the lack of interaction between $k_{x,n\neq 0}$ modes leads to too much energy being retained in the large scale and too little dissipation in the small scales. We address this by setting $\tilde{u}_i^{n=7} = 0$ (before the pressure solving step, in order to maintain a divergence-free velocity field) in the region $y/H \leq 0.1$, where $\tilde{u}_i^n$ are the complex Fourier coefficients of velocity for the nth streamwise Fourier mode (cf. Equation (3.11)). The resulting mean velocity profile (case R-5(ii))

is plotted in Figure 3.13(b) and shows better agreement with the rough-wall logarithmic velocity profile. We adopt this height-dependent 'mode-blocking' approach for all of the Regime II band-limited RNL-LES cases of Table 3.2.

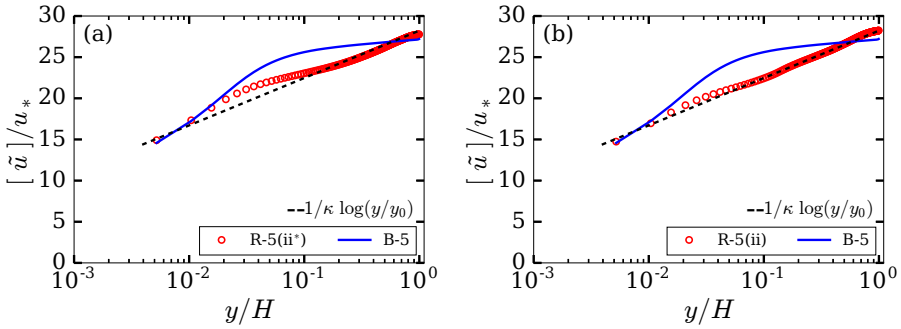

Figure 3.13: Band-limited and baseline RNL-LES mean velocity profiles in Regime II: (a) first attempt to include the large ($k_{x,7}$) scale in case R-5(ii), without limiting its influence near the wall and (b) the influence of $k_{x,7}$ is limited near the wall, resulting in a more accurate mean velocity profile.

Figure 3.14(a) shows the mean velocity profiles resulting from the band-limited RNL-LES cases in Regime II of Table 3.2. Note that these results were obtained with the inclusion of just one streamwise wavenumber in the dissipative small scale region, which proved sufficient, whereas the cases of Regime I required an ever-widening band of wavenumbers in this region to obtain realistic results. The mean velocity profiles for cases R-4(ii), R-5(ii), and R-6 show significantly better agreement with the correct log law than do their corresponding baseline RNL-LES cases (see Figure 3.3). Likewise, the corresponding streamwise Reynolds stresses again compare much more favorably to LES. Referring to Figure 3.14(b), the peak Reynolds stresses have fallen once again to a value of approximately 8 whereas the baseline

RNL-LES Reynolds stresses peaked at a value closer to 18. Note the clear discontinuity at $y/H = 0.1$ (indicated with the dashed vertical line) in the Reynolds stress profiles. This is due to the 'mode-blocking' of $k_{x,7}$ scale in the region $y/H \leq 0.1$, described earlier in the section.

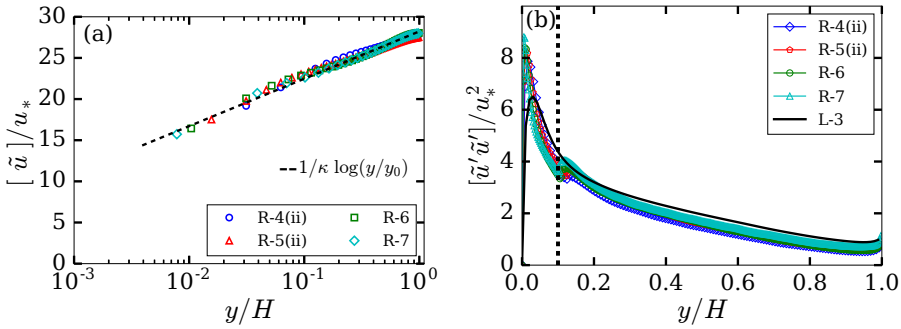

Figure 3.14: Band-limited RNL-LES mean velocity and streamwise Reynolds stress profiles (Regime II cases). The superscript prime $'$ in the plot labels indicates fluctuations about the time-averaged value.

Referring back to the LES data (case L-6) in Figure 3.7, we see the beginnings of the emergence of a third distinct scale at $\approx \lambda_{z,1}$, in between the large scale and dissipative small scale. Even so, the realistic results of case R-6 suggest that just the two streamwise scales of $k_{x,7}$ and $k_{x,28}$ are enough to achieve accurate turbulence statistics.

We simulated one additional case (R-7), which does not have a corresponding baseline RNL-LES case, to test whether or not the 'mode-blocking' approach of Regime II, with only two streamwise scales, would continue to hold at the even larger cross-plane resolution of $[N_y, N_z] = [384, 768]$. The resulting mean velocity and streamwise Reynolds stress profiles, also plotted in Figure 3.14, suggest that Regime II holds at this grid size. While we did not

attempt any cases for grid sizes larger than that of case R-7, we expect that the emergence of a third, intermediate scale (seen to begin emerging in case L-6 in Figure 3.7) will require the inclusion of a third streamwise wavenumber, in between the large scale of $k_{x,7}$ and the dissipative small scale which scales with the grid size; validating this hypothesis is a direction for future work.

We end the discussion with a note on the computational cost of simulating the RNL-LES system. Our simulations of the baseline RNL-LES system necessarily were carried out with the same numerical setup and on the same size physical space grids as their corresponding LES cases. As such, the computational cost of the baseline RNL-LES system is comparable to that of LES. The band-limited RNL-LES system, however, has the potential for significant computational speedups over LES due to the drastically reduced number of degrees of freedom. In our implementation, we employed a hybrid physical/Fourier space grid and calculated the nonlinear terms as convolutions in Fourier space in the streamwise direction, as described in section 3.3. This allowed us to store only the Fourier modes of interest for each simulation case and to eliminate many of the FFTs required by a traditional pseudospectral approach. Case R-5 was our largest cross-plane grid size studied herein with both Regime I and II sub-cases. With a fixed number of processors on the same hardware, we measured simulation wall time speedups of 3.0x for case R-5(i) and 17.2x for case R-5(ii) relative to LES (case L-5). The Regime I speedup is not significant since the number of required streamwise Fourier modes increases as the dissipation range shifts to smaller and smaller wavelengths. The Regime II speedup, however, is significant as only a single large scale

($k_{x,7}$) and a single small scale ($k_{x,21}$) are needed (in addition to the streamwise mean flow, $k_{x,0}$). While all four Regime II cases studied herein required only two nonzero streamwise Fourier modes, we expect that further increasing the cross-plane grid resolution will eventually require the inclusion of more streamwise Fourier modes as the scale separation increases. Nonetheless, with a fixed or slowly growing number of streamwise wavenumbers, significant computational speedups can be obtained with band-limited RNL-LES in Regime II over LES as cross-plane grid resolution increases.

Chapter 4

Application to reduced-order wind farm simulations

4.1 Introduction

The first and primary goal of this chapter is to assess the suitability of the RNL-LES framework for wind farm simulations. We pursue this goal by simulating a number of RNL-LES wind farm configurations and comparing the results with traditional LES. In the second part of this chapter, we leverage the computational affordability of this reduced-order approach to conduct a parametric study of vertical staggering of wind turbine hub heights in fully-developed wind farms, an area which has not received much attention in the existing literature (see, e.g., Vasel-Be-Hagh and Archer 2017; Stevens, Arendshorst, and Wang 2017). After introducing the equations of motion in Section 4.2, we describe the numerical setup in Section 4.3, followed by the results and discussion in Section 4.4. The main contents of this chapter appear in the submitted manuscript by Bretheim, Meneveau, and Gayme (2018b).

We note that while in the previous chapters we have designated the spanwise and wall-normal coordinate directions as the z- and y-directions, respectively, in this chapter we change notations in order to align with the customary notations used within the wind energy literature. As such, the spanwise and wall-normal directions are now referred to as the y- and z-directions, respectively. The streamwise direction continues to be referred to as the x-direction.

4.2 Dynamical RNL-LES equations

The RNL-LES system is defined in terms of streamwise-averaged velocity and pressure fields ($\mathbf{U}$ and P, respectively) and streamwise-varying velocity and pressure fields ($\mathbf{u}$ and p, respectively). The total velocity and pressure fields are written as:

$$\mathbf{u}^{tot}(x,y,z,t) = \underbrace{\mathbf{U}(y,z,t)}_{=\langle \mathbf{u}^{tot} \rangle_x} + \mathbf{u}(x,y,z,t), \tag{4.1a}$$

$$p^{tot}(x,y,z,t) = \underbrace{P(y,z,t)}_{=\langle p^{tot} \rangle_x} + p(x,y,z,t). \tag{4.1b}$$

The streamwise, spanwise, and vertical directions are denoted by the coordinates x, y, and z, respectively. The angle brackets $\langle \cdot \rangle$ indicate an averaged quantity, where any subscript indicates the type of averaging (e.g., $\langle \cdot \rangle_x$ is a streamwise-averaged quantity and $\langle \cdot \rangle_{y,t}$ is a spanwise- and time-averaged quantity). The streamwise, spanwise, and vertical velocity components are denoted by u, v, and w, respectively.

In this work, we present simulation results of both the RNL-LES and

LES systems. Since the RNL-LES system is the main focus of the work, we first describe that system and then describe how to recover the relevant LES equations from the RNL-LES equations. We first consider the case without the turbine forcing term. The set of equations used for the simulations of the RNL-LES system described herein are written as:

$$\partial_t \tilde{\mathbf{U}} + \tilde{\mathbf{U}} \cdot \nabla \tilde{\mathbf{U}} + \nabla \tilde{P}_\star - \frac{1}{\mathrm{Re}} \nabla^2 \tilde{\mathbf{U}} = -\langle \tilde{\mathbf{u}} \cdot \nabla \tilde{\mathbf{u}} \rangle_x - \nabla \cdot \langle \boldsymbol{\tau}^{tot,r} \rangle_x + \partial_x \tilde{p}_\infty \hat{\mathbf{e}}_\mathbf{x}, \quad (4.2a)$$

$$\partial_t \tilde{\mathbf{u}} + \tilde{\mathbf{U}} \cdot \nabla \tilde{\mathbf{u}} + \tilde{\mathbf{u}} \cdot \nabla \tilde{\mathbf{U}} + \nabla \tilde{p}_\star - \frac{1}{\mathrm{Re}} \nabla^2 \tilde{\mathbf{u}} = -\nabla \cdot \boldsymbol{\tau}^r, \quad (4.2b)$$

where $\nabla \cdot \tilde{\mathbf{U}} = \nabla \cdot \tilde{\mathbf{u}} = 0$ and $\partial_x \tilde{p}_\infty$ is the streamwise pressure gradient driving the flow ($\hat{\mathbf{e}}_\mathbf{x}$ is the streamwise direction unit vector). The modified pressure is $\tilde{p}_*^{tot} = \tilde{P}_* + \tilde{p}_*$ and includes the isotropic part of the sub-grid stress tensor. The tilde symbol indicates the coarse-grained quantities, as usual in LES.

The anisotropic part of the sub-grid scale stress tensor is modeled according to

$$\boldsymbol{\tau}^{tot,r} = -2 \left(\lambda_{\mathrm{SGS}}^2 \sqrt{2 \langle \tilde{\mathbf{S}} : \tilde{\mathbf{S}} \rangle_{x,y}} \right) \tilde{\mathbf{S}}, \quad (4.3)$$

where $\tilde{\mathbf{S}} = (\nabla \tilde{\mathbf{u}}^{tot} + \nabla \tilde{\mathbf{u}}^{tot,T})/2$ is the symmetric part of the filtered velocity gradient tensor. The Smagorinsky lengthscale λ_{SGS} is calculated with a wall-damping function according to

$$\lambda_{\mathrm{SGS}} = C_s \Delta = \left[\left(\frac{1}{C_0 \Delta} \right)^2 + \left(\frac{1}{\kappa (z + z_0)} \right)^2 \right]^{-1/2}, \quad (4.4)$$

as in the work by Albertson (1996), where C_0 is the Smagorinsky constant, Δ is the filter width, κ is the von Kármán constant, and z_0 is the roughness length. The wall region is not resolved but rather modeled (following the standard

equilibrium wall model of Schmidt and Schumann (1989)) by prescribing log law stresses such that

$$\boldsymbol{\tau}_{x,z}^{tot,w} = -\left(\frac{\tilde{u}_r \kappa}{\ln(z_1/z_0)} \frac{\tilde{u}^{tot}(x,y,z_1)}{\tilde{u}_r}\right)^2, \tag{4.5a}$$

$$\boldsymbol{\tau}_{y,z}^{tot,w} = -\left(\frac{\tilde{u}_r \kappa}{\ln(z_1/z_0)} \frac{\tilde{v}^{tot}(x,y,z_1)}{\tilde{u}_r}\right)^2, \tag{4.5b}$$

$$\tilde{u}_r = \sqrt{\langle \tilde{u}^{tot}(x,y,z_1)^2 + \tilde{v}^{tot}(x,y,z_1)^2 \rangle_{x,y}}, \tag{4.5c}$$

where z_1 is the height of the first grid point above the wall. The recent work by Bretheim, Meneveau, and Gayme (2018a), which introduces the RNL-LES system, contains further details on the RNL-LES equations and the corresponding sub-grid stress and wall models.

To simulate the effect of wind turbines on the flow system, we augment Equation (4.2a) by adding an actuator disk forcing term ($F_{T,n}\hat{\mathbf{e}}_\mathbf{x}$) to the right-hand side of the equation (here the subscript n, where n=2 or 3, is used to distinguish between the RNL-LES and LES versions of the turbine forcing, respectively). The need for two different versions of the turbine forcing term is due to the streamwise-averaged, reduced-order nature of the RNL-LES model and is further explained later in this section as well as in Section 4.3. We explain the RNL-LES turbine forcing term by first referencing the typical LES context, where the actuator disk turbine forcing is calculated according to

$$F_{T,3}(\mathbf{x}) = -\frac{1}{2}\frac{\pi D^2}{4}\rho C_T' \langle \tilde{u} \rangle_{d,t}^2 \mathcal{R}_3(\mathbf{x}), \tag{4.6}$$

where ρ is the fluid density, C_T' is the (local) thrust coefficient, D is the turbine rotor diameter, and $\langle \tilde{u} \rangle_{d,t}$ is the disk- and time-averaged velocity. This approach, which is used in the work by Stevens, Graham, and Meneveau (2014), uses a smoothed normalized indicator function $\mathcal{R}_3(x, y, z)$ to distribute the turbine thrust force over the grid points in the turbine rotor region. The spatial disk-averaging is calculated according to

$$\langle \tilde{u} \rangle_d = \int \mathcal{R}_n(\mathbf{x})\ \tilde{\mathbf{u}}(\mathbf{x})\ d^n\mathbf{x}, \quad n = 2 \text{ or } 3. \tag{4.7}$$

The spatial disk-averaging changes with simulation context ($n = 3$ for the fully three-dimensional LES setting and $n = 2$ for the reduced-order RNL-LES setting). Before the turbine forcing is applied to the flow, the disk-averaged velocity is further smoothed in time (Calaf, Meneveau, and Meyers 2010; VerHulst and Meneveau 2014) via time-averaging over a short time scale (T). The smoothed indicator function is calculated according to

$$\mathcal{R}_n(\mathbf{x}) = \int G_n(\mathbf{x} - \mathbf{x}')\mathcal{I}_n(\mathbf{x}')\mathrm{d}^n(\mathbf{x}'), \tag{4.8}$$

where the Gaussian smoothing kernel is

$$G_n(\mathbf{x}) = [6/(\pi\Delta_n)]^{n/2} \exp\left(-6||\mathbf{x}||^2/\Delta_n^2\right), \tag{4.9}$$

and the indicator function is either

$$\mathcal{I}_3(\mathbf{x}) = (s\pi D^2/4)^{-1}\left[H(\hat{x} + s/2) - H(\hat{x} - s/2)\right] H(D/2 - \hat{r}), \tag{4.10}$$

or

$$\mathcal{I}_2(\mathbf{x}) = (\pi D^2/4)^{-1} H(D/2 - \hat{r}), \tag{4.11}$$

depending on the simulation context (LES: $n = 3$, RNL-LES: $n = 2$), with r as the distance from the rotor center. The turbine thickness s is relevant only in the LES context and $H(x)$ is the Heaviside (unit step) function. The filter width in the smoothing kernel is taken as either $\Delta_3 = 1.5\sqrt{\Delta_x^2 + \Delta_y^2 + \Delta_z^2}$ or $\Delta_2 = 1.5\sqrt{\Delta_y^2 + \Delta_z^2}$, once again depending on the simulation context.

In the LES setting, the turbine forcing is applied pointwise in three-dimensional physical space. In the RNL-LES setting, however, the simulation is conducted entirely in streamwise Fourier space (Bretheim, Meneveau, and Gayme 2018a) in order to take advantage of the system's properties and for computational efficiency (further details are in Section 4.3). Since the RNL-LES equations are simulated entirely in streamwise Fourier space, the turbine forcing is also calculated and applied in the streamwise Fourier space according to

$$F_{T,2}(\mathbf{x}) = -\frac{1}{2}\frac{\pi D^2}{4}\rho C_T' \left\langle \tilde{U} \right\rangle_{d,t} * \left\langle \tilde{U} \right\rangle_{d,t} \frac{N_r}{L_x}\mathcal{R}_2(\mathbf{x}), \tag{4.12}$$

where $\left\langle \tilde{U} \right\rangle_{d,t}$ is the disk- and time-averaged streamwise mean (zeroth streamwise Fourier mode) velocity and N_r is the number of turbine rows along the streamwise direction. Note the $*$ symbol denotes the convolution operation as the calculation for the turbine forcing is conducted in streamwise Fourier space (in keeping with the RNL-LES framework). The turbine forcing of Equation (4.12) differs from that of Equation (4.6) in two key ways: 1) it uses the two-dimensional version of the Gaussian smoothing kernel appropriate for RNL-LES rather than the three-dimensional version appropriate for LES and 2) it represents the integrated effect of multiple streamwise turbine rows and

applies that forcing only to the streamwise mean part of the flow whereas the forcing of Equation (4.6) is applied locally in the streamwise direction within the fully three-dimensional LES context.

While the equations for this section describe the RNL-LES system, we also include LES results in this work. The LES system is recovered from the RNL-LES system simply by adding the terms $-(\mathbf{u}\cdot\nabla\mathbf{u} - \langle\mathbf{u}\cdot\nabla\mathbf{u}\rangle_x)$ to the right-hand side of Equation (4.2b) and removing the horizontal averaging operation from Equations (4.3) and (4.5c). For a comprehensive explanation of the differences between the RNL-LES and LES systems, refer to the work (Bretheim, Meneveau, and Gayme 2018a) which originally introduced the RNL-LES system.

4.3 Numerical setup

Our RNL-LES and LES numerical simulations are carried out with the LES research code that was previously modified to implement the RNL-LES system (Bretheim, Meneveau, and Gayme 2018a), as well as used for many prior LES studies of wind farms (Calaf, Parlange, and Meneveau 2011; Stevens, Gayme, and Meneveau 2014; VerHulst and Meneveau 2014). The code is pseudospectral in both horizontal directions (x and y) for LES, while for RNL-LES only the spanwise direction (y) is pseudospectral while the x direction is treated entirely in Fourier space. The vertical direction (z) is treated with second-order finite differencing. The second-order Adams-Bashforth scheme is used for time integration with a maximum Courant number of 0.05 at every timestep.

The horizontal directions have periodic boundary conditions, the top boundary has zero stress and vertical velocity, and the bottom boundary condition is described by Equations (4.5a)-(4.5c). The grid spacing is uniform in all directions and the advective terms in Equations (4.2a)-(4.2b) are dealiased with the 3/2 rule.

All simulations reported herein use $\kappa = 0.4$ and a roughness length $z_0/H = 10^{-4}$, where $H = 1000$ m is the characteristic lengthscale describing the height of the ABL. In this work, all simulations are conducted at effectively infinite Reynolds number, so the viscous terms of Equations (4.2a)-(4.2b) are neglected. The simulation cross-plane box size is $[L_y, L_z]/H = [\pi, 1]$ with gridpoints $[N_y, N_z] = [128, 128]$ for all cases. The LES cases, in which the x direction is also treated in the pseudospectral fashion, additionally have $L_x = \pi$ and $N_x = 128$. The RNL-LES cases, which are conducted entirely in the $k_{x,n}$ Fourier space, as previously noted, use streamwise wavenumbers of $k_{x,n} = n(2\pi H/L_x)$ where $n = \{0, 7, 8, 9\}$. These particular streamwise wavenumbers are chosen using the method described by Bretheim, Meneveau, and Gayme (2018a) and are a consequence of the prescribed cross-plane grid resolution and Smagorinsky constant $C_0 = 0.23$. As in Bretheim, Meneveau, and Gayme (2018a), for all cases considered herein the filter width in Equation (4.4) is set to $\Delta = (\Delta_y \Delta_z)^{1/2}$, where, e.g., $\Delta_y = L_y/(HN_y)$. All actuator disk turbines use $D = 100$ m, $C_T' = 4/3$, and have a baseline hub height of $z_h = 100$ m. In the LES context, the turbines additionally are represented by a filtered top-hat region of thickness $s = 10$ m. The short time scale used to time-average the disk-averaged velocity is $T = 30$ s. We use the velocity scale

$u_* = 0.45$ m/s for nondimensionalization.

Many of the LES-based wind farm studies cited in the introduction employed the pseudospectral LES approach (and corresponding periodic domain, simulating what is sometimes referred to as an "infinite" wind farm), as in Calaf, Meneveau, and Meyers (2010), which lends itself well to simulations of wind farms in the fully-developed regime and it is this regime only that we will consider herein. We note that the later work by Stevens, Graham, and Meneveau (2014), introduced the idea of using a concurrent precursor simulation in order to generate realistic turbulent inflow conditions and enable the simulation of finite (developing regime) wind farms within the context of pseudospectral LES. This precursor approach is used in several of the works previously cited. The focus of this work, however, is to introduce a reduced-order LES-based approach to wind farm simulations based on a RNL methodology whose averaging assumptions make it more appropriate for very large wind farms in the fully-developed regime.

4.4 Results and discussion

The results are presented in two sections. In Section 4.4.1 we evaluate the ability of the RNL-LES framework to simulate wind farms by comparing to standard LES of wind farms over a range of conditions summarized in Table 4.1. In Section 4.4.2 we report results from an initial application of the new RNL-LES framework to a parametric study of the effects of vertical staggering of turbine hub heights in very large wind farms.

4.4.1 Validating the RNL-LES wind farm model against LES

The results presented in this section are from the simulations summarized in Table 4.1. The number of columns (N_c) of turbines is fixed for all cases while the number of rows (N_r) is varied in order to assess the ability of the RNL-LES framework to capture multiple streamwise rows of turbines despite the reduced-order nature of the streamwise direction in the model. To enhance statistical convergence of the resulting statistics, each case is simulated ten times with different random initial conditions and then ensemble-averaged.

Group	$[\mathbf{N_x}, \mathbf{N_y}, \mathbf{N_z}]$	$\mathbf{S_y/D}$	$\mathbf{S_x/D}$	$\mathbf{N_r \times N_c}$
L2	[128,128,128]	5.24	5.24	6×6
L3	[128,128,128]	5.24	7.85	4×6
R1	[— ,128,128]	5.24	3.93	8×6
R2	[— ,128,128]	5.24	5.24	6×6
R3	[— ,128,128]	5.24	7.85	4×6
R3	[— ,128,128]	5.24	10.47	3×6

Table 4.1: Summary of simulation cases. The label 'R' refers to RNL-LES while 'L' refers to LES. N_r and N_c refer to the number of turbine rows and columns, respectively. The turbine-to-turbine spacings in the spanwise and streamwise directions are indicated by S_y and S_x, respectively.

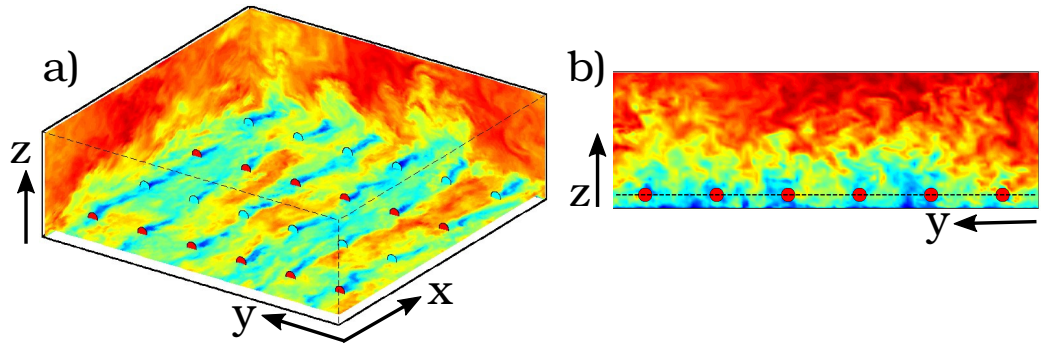

Figure 4.1: Contour plots of streamwise velocity obtained from (a) LES and (b) RNL-LES. Specifically, (a) corresponds to the turbine layout for case L3 of Table 4.1 while (b) shows the same configuration in the y-z cross-plane, which is effectively the domain of case R3, which only has a two-dimensional physical space grid and represents out-of-plane variations in streamwise Fourier space. The red and blue circles represent the turbine rotor swept areas and the dashed black line in panel (b) is at the turbine baseline hub height (z_h).

Note that case L3 of Table 4.1 corresponds to the primary configuration used by Calaf, Meneveau, and Meyers (2010). In Figure 4.1(a), we plot the three-dimensional domain with this turbine layout and superposed streamwise velocity contour plots on select planes from the LES. The horizontal plane is at the turbine hub height, where the wakes are clearly visible behind each turbine. Figure 4.1(b) shows the corresponding domain for the RNL-LES for the same configuration.

Next, the properties of the mean velocity distribution are examined, followed by a discussion of the kinetic energy budgets in the flow. Figure 4.2 plots the mean velocity profiles for the RNL-LES system without turbines as well as with turbines for the four different streamwise spacings considered herein. The RNL-LES mean velocity profiles (with turbines) compare well with those of the reference LES cases, particularly in the region around

the baseline turbine hub heights at $z/H = 10^{-1}$. We note that the LES case with no turbines over-predicts the rough wall log law while still having an accurate slope. This result is expected given our use of the constant coefficient Smagorinsky sub-grid scale model (Porté-Agel, Meneveau, and Parlange 2000). The RNL-LES mean velocity profile with no turbines (black circle markers) matches well with the rough wall log law, a result of our choice of nonzero streamwise Fourier modes, as discussed in Section 4.3.

The LES shows that as the streamwise spacing between turbine rows decreases, the resulting mean velocity profile decreases. This is the expected trend (as more energy is harvested from the ABL) and the RNL-LES accurately captures this effect despite the reduced-order nature of the model. The RNL-LES mean velocity is generally higher than that of the LES near the top of the domain and this effect seems to be increased a bit with the addition of the turbines in the domain as the RNL-LES overpredicts the mean velocity above the turbine region (i.e., for $z/H > 0.3$). Additionally, we note that the agreement between the RNL-LES and LES mean velocity profiles tends to decrease as the streamwise spacing of turbines increases. At $S_x/D = 10.47$ the disagreement is readily visible. This discrepancy makes sense in light of the simplified nature of the actuator disk implementation for RNL-LES, which is essentially a streamwise-averaged version of the actuator disk forcings, effectively reducing their effect to an "infinite tube" of turbines forcing the flow, as required by the streamwise-averaged nature of the RNL-LES system. The proposed approach therefore makes more sense as the streamwise spacing of turbines decreases and the column becomes more tube-like, explaining why

we have very good agreement between LES and RNL-LES mean velocity profiles in the turbine region at $S_x/D = 3.93$. We note that this approach is accurate for the range of streamwise row spacings seen in typical wind farms.

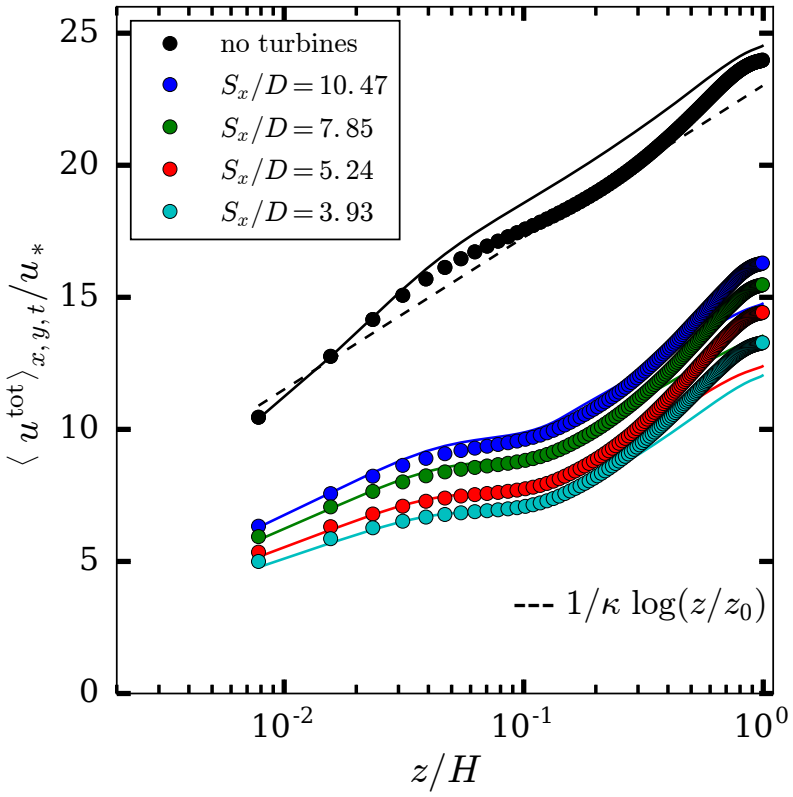

Figure 4.2: Mean velocity profiles for the RNL-LES system (circle markers) with and without turbines compared to those for the LES system (solid lines) and the rough wall log law (dashed line).

For a more qualitative appreciation of the mean velocity results, we consider next Figure 4.3, which compares the mean streamwise velocity in the y-z cross-plane for the LES and RNL-LES. The effect of the six spanwise turbine columns are clearly visible in each. While the actuator disk implementation differs slightly between LES and RNL-LES, the primary difference between the

LES and RNL-LES cases stems from the mean velocity profile, which, as noted previously in the discussion of Figure 4.2, is slightly faster for the RNL-LES system near the top of the domain, even for the baseline case without wind turbines.

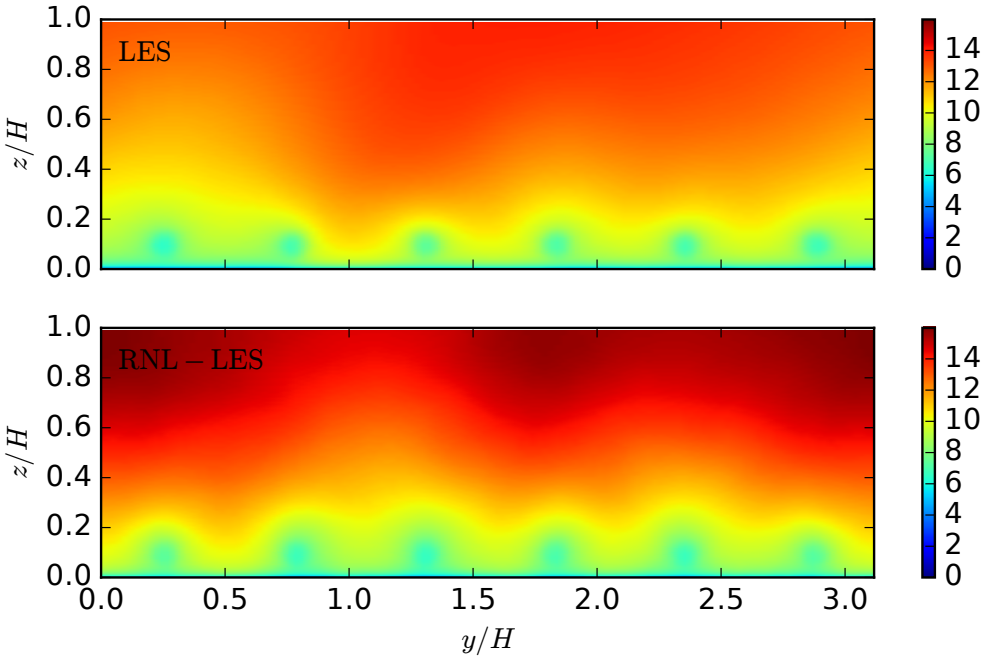

Figure 4.3: Contours of mean streamwise velocity in the y-z cross-plane for representative LES and RNL-LES cases.

As a next step, we analyze the terms affecting the kinetic energy in the

flow. For the LES system, the mean kinetic energy budget is described by

$$\partial_t E = \underbrace{-\left\langle \tilde{\mathbf{u}}^{\mathbf{tot}} \right\rangle_t \cdot \nabla E}_{\text{advection}} \underbrace{- \nabla \cdot \left[\left\langle \tilde{\mathbf{u}}^{\mathbf{tot}} \right\rangle_t \cdot (\mathbf{R} + \langle \tilde{\boldsymbol{\tau}} \rangle_t) \right]}_{\text{KE flux}} + \underbrace{(\mathbf{R} + \langle \tilde{\boldsymbol{\tau}} \rangle_t) : \nabla \left\langle \tilde{\mathbf{u}}^{\mathbf{tot}} \right\rangle_t}_{\text{KE dissipation}} -$$

$$\underbrace{\nabla \cdot \left[\left\langle \tilde{\mathbf{u}}^{\mathbf{tot}} \right\rangle_t p^{tot} + \left\langle \tilde{\mathbf{u}}^{\mathbf{tot}} \right\rangle_t p_\infty \hat{\mathbf{e}}_x \right]}_{\text{pressure work}} + \underbrace{\left\langle \tilde{\mathbf{u}}^{\mathbf{tot}} \right\rangle_t \cdot \langle \mathbf{F}_{\mathbf{T,n}} \rangle_t}_{\text{power extraction}}. \quad (4.13)$$

where $E = (\left\langle \tilde{\mathbf{u}}^{\mathbf{tot}} \right\rangle_t \cdot \left\langle \tilde{\mathbf{u}}^{\mathbf{tot}} \right\rangle_t)/2$ and $\mathbf{R} = \langle \tilde{\mathbf{u}}' \tilde{\mathbf{u}}' \rangle_t$ (here the prime symbol denotes departure from the time-averaged value of $\tilde{\mathbf{u}}^{tot}$).

In Figure 4.4 we plot vertical profiles of terms in the kinetic energy budget of Equation (4.13) for both the LES and RNL-LES systems, which show close agreement. Calaf, Meneveau, and Meyers (2010) demonstrated the importance of the vertical fluxes of kinetic energy in enabling the wind farm to extract mean-flow kinetic energy from the ABL. This phenomenon was confirmed by Cal et al. (2010) in their experimental investigations. As such, the ability of RNL-LES to closely match LES in the vertical profiles of relevant kinetic energy budget terms represents an important test for the new model and its ability to realistically model wind farm power output. We note that the power extracted by the turbines is clearly balanced by the vertical flux of kinetic energy, as expected.

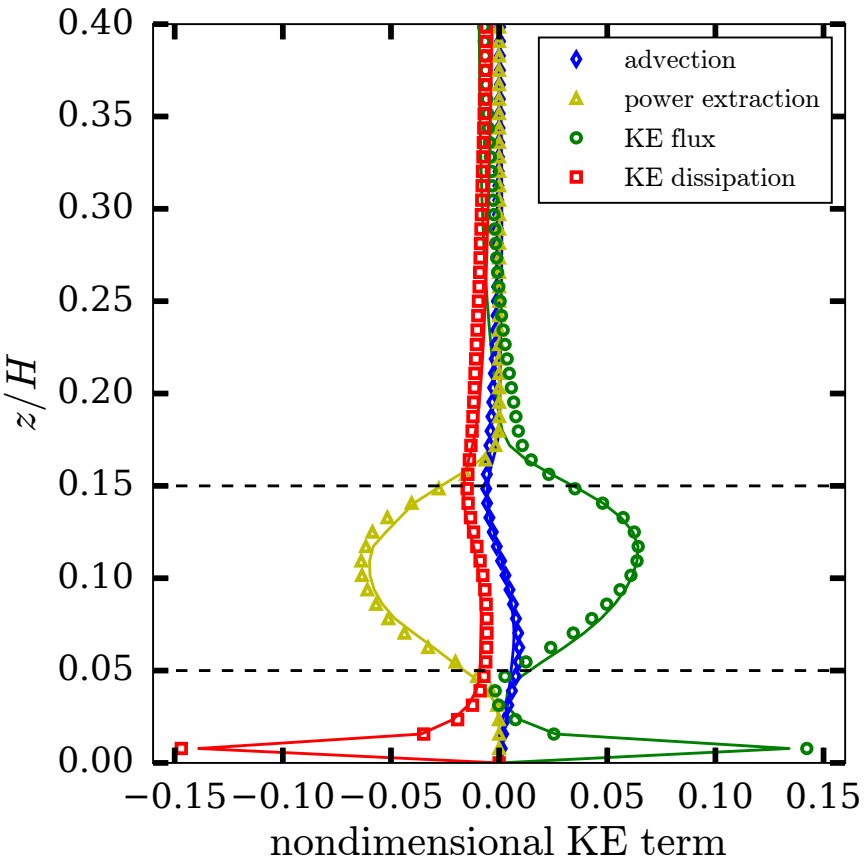

Figure 4.4: Vertical profiles of the relevant terms in the kinetic energy budget in Equation (4.13). Note that each term is horizontally-averaged for plotting purposes and each term is nondimensionalized by u_*^3/H. Markers and solid lines denote RNL-LES and LES data, respectively. The horizontal dashed lines mark the turbine region.

4.4.2 Application to vertical staggering

Since the RNL-LES simulated wind farm results match well with those obtained by LES, we now apply this low cost, reduced-order approach to a parametric study of the effects of vertical staggering of turbine hub heights. The vertical staggering of hub heights in real wind farms could serve as a

relatively straightforward strategy for mitigating wake effects (from upstream turbines) which tend to decrease overall wind farm power production. Recent work in this area has been primarily based on analytical wake models (see, e.g., the review in Vasel-Be-Hagh and Archer (2017)). High computational cost LES studies of vertically-staggered wind farms are still very limited, with Vasel-Be-Hagh and Archer (2017) reporting one vertically-staggered case with potential power gains of 9.5% (over the corresponding vertically aligned case) and Stevens, Arendshorst, and Wang (2017) reporting several vertically-staggered cases with significantly smaller performance gains. The high computational cost of LES is a major barrier for studies requiring many unique simulations, while approaches based on analytical models are typically much more computationally affordable with less physical fidelity. The RNL-LES framework strikes a balance somewhere in the middle, with physical fidelity closer to that of LES but with lower simulation wall times. The cases studied using RNL-LES (and some LES comparison cases) are summarized in Table 4.2.

While LES has been demonstrated to closely predict wind farm power output of real wind farms (Stevens, Graham, and Meneveau 2014) (albeit at high computational cost), wake model and RANS-based approaches (Barthelmie et al. 2009; Sanderse, Pijl, and Koren 2011) have shown considerably more variability in their ability to accurately predict wind farm power output. One additional advantage of the RNL-LES approach is the absence of any tuning parameters which are typically present in the engineering models.

Group	$[\mathbf{N_x}, \mathbf{N_y}, \mathbf{N_z}]$	$\mathbf{S_y/D}$	$\mathbf{S_x/D}$	$\mathbf{N_r \times N_c}$	**Staggering** (%)
L2	[128,128,128]	5.24	5.24	6×6	0, 10
L3	[128,128,128]	5.24	7.85	4×6	0, 30
R1	[— ,128,128]	5.24	3.93	8×6	0, 10, 20, 30, 40
R2	[— ,128,128]	5.24	5.24	6×6	0, 10, 20, 30, 40
R3	[— ,128,128]	5.24	7.85	4×6	0, 10, 20, 30, 40
R3	[— ,128,128]	5.24	10.47	3×6	0, 10, 20, 30, 40

Table 4.2: Groups are organized according to the nomenclature of Table 4.1, where each configuration is run at multiple different vertical staggerings. A particular case is referred to, for example, as R1-20, which indicates group R1 at 20% staggering.

In Figure 4.5 we plot the profiles of the two most important mean kinetic energy terms (power extractions at the turbines and vertical kinetic energy flux) across all five vertical staggering levels considered (0% staggered, i.e., vertically-aligned through 40% staggered). The horizontal dashed lines indicate the rotor swept areas of the vertically-aligned and vertically-staggered turbines. As the amount of vertical staggering increases, the swept area overlap decreases while the total swept area in the two newly exposed turbine regions increases, leading to an increase in turbine power extraction (with a corresponding increase in the vertical kinetic energy flux).

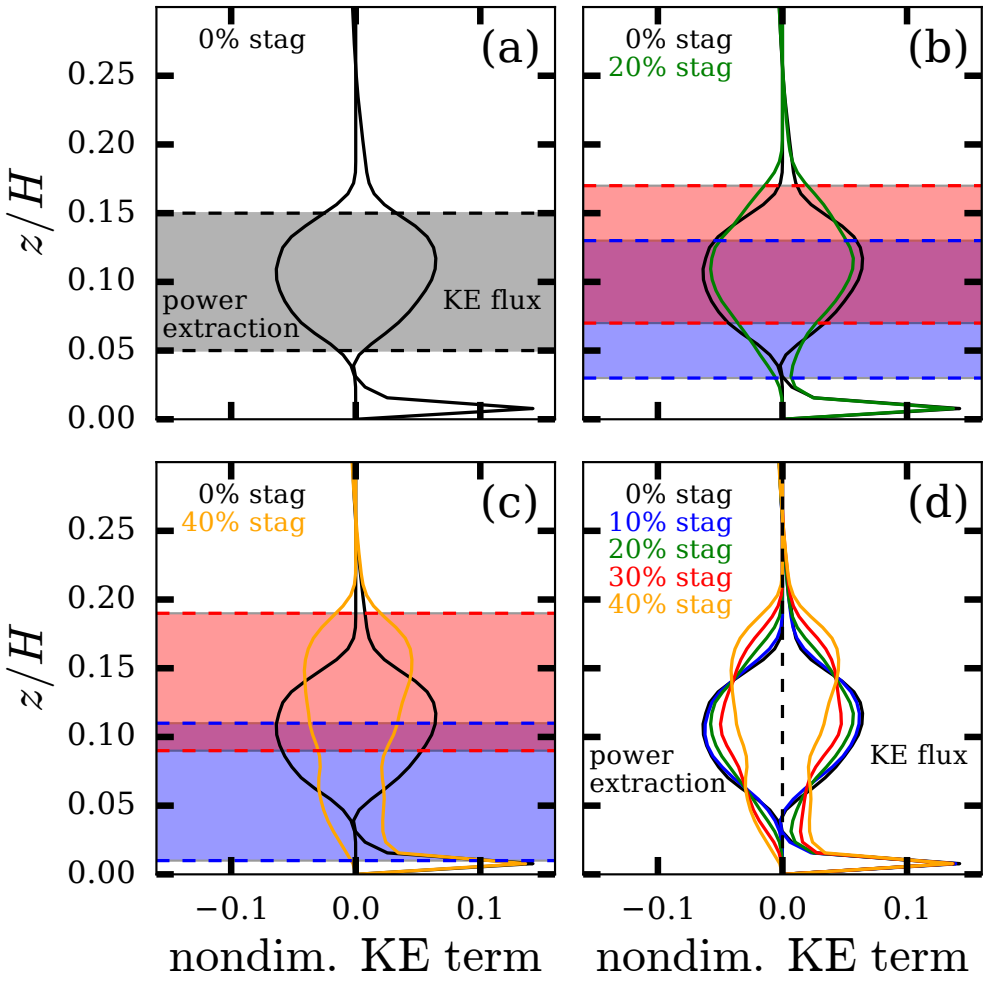

Figure 4.5: Vertical profiles of the power extraction and kinetic energy flux terms of the kinetic energy budget for all vertical staggering levels considered herein. Each term is nondimensionalized by u_*^3/H and horizontally-averaged. The black shaded region (panel a) shows the rotor swept area of the vertically-aligned turbines. The red and blue shaded regions (panels b and c) show the rotor swept areas of the upwardly- and downwardly-staggered turbines, respectively, with the purple region indicating area overlap.

In Figure 4.6 we compare representative power signals from LES and RNL-LES wind farms. The power produced by an actuator disk turbine is approximated as $P = -F_{T,3}(\mathbf{x}) \langle \tilde{u} \rangle_{d,t}$ (for LES) and $P = -F_{T,2}(\mathbf{x}) * \langle \tilde{U} \rangle_{d,t}$ (for

RNL-LES). Here the RNL-LES signals are smoother than the corresponding LES signals, which is an expected result of the streamwise-averaged dynamics of the RNL-LES system, as it retains fewer small turbulent streamwise scales. The RNL-LES power signals of panel (b) shows a clear correlation between the lower and upper rows of turbines, which is to be expected since at only 10% vertical staggering, there is still considerable overlap between the turbine swept areas of the lower and upper turbine regions. The correlation is noticeably less in panel (d), where the vertical staggering is 30%. The LES power signals in panels (a) and (c) are less correlated, as expected, since the model is fully three-dimensional, with true turbine rows that are separated in physical space.

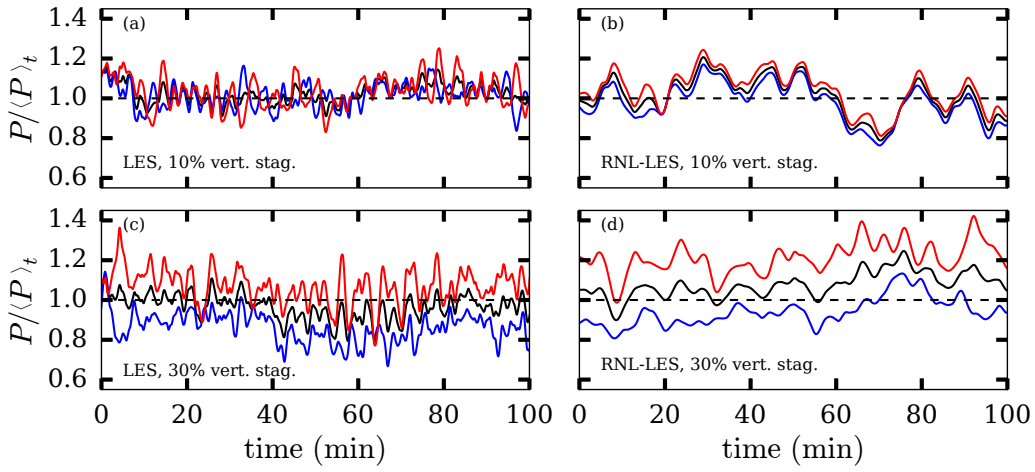

Figure 4.6: Representative wind farm power signals for both RNL-LES and LES at vertical staggering levels of 10% and 30%. The power signals are normalized by the time-averaged value of the power produced by the corresponding vertically-aligned wind farm. Red curves represent the average power production of upwardly-staggered rows while the blue curves are that of the downwardly-staggered rows. The black curves show the overall wind farm power output.

Figure 4.7 plots the power gain for all of the streamwise spacings and

vertical staggering levels considered herein. These results are computed via time- and ensemble-averages of the power signals like those plotted in Figure 4.6. There is a net gain in power output for all cases considered, with the gain increasing as the vertical staggering increases. While the upper rows of turbines increase in power output and the lower rows of turbines decrease (both as expected), the increase in the power output of the upper rows outstrips the decrease in the power output of the lower rows due to the higher wind resource above the farm, producing the effect of a net power gain across the entire wind farm relative to the corresponding vertically-aligned wind farm. This effect seems to be independent of the streamwise spacing of turbines considered here. Additionally, the RNL-LES compares fairly well with the two sets of LES reference cases. We note once again, however, that the wind farms simulated in this study are only to be interpreted in terms of the fully-developed region of a very large wind farm.

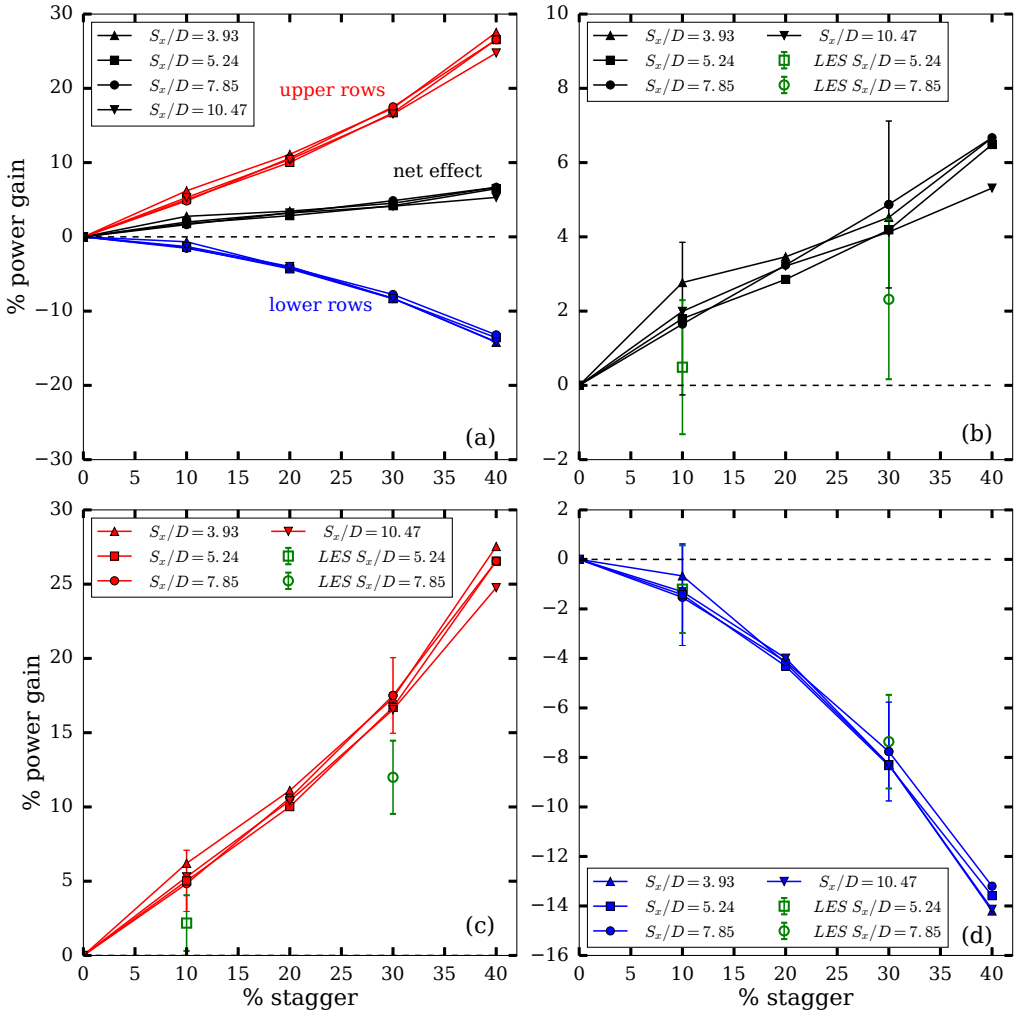

Figure 4.7: Wind farm power output gain as a function of vertical staggering. All results (a), net power gains (b), upper row power gains (c), and lower row power gains (d).

Vasel-Be-Hagh and Archer (2017) considered a wind farm of similarly sized turbines and reported net power gains of 5.4% (in a PARK-based (Katic, Højstrup, and Jensen 1986) model) and 9.5% (using LES) for a wind farm with approximately 25% vertical staggering. While both of these results are higher than those reported in Figure 4.7, their wind farm is a finite, developing

wind farm whereas our RNL-LES results pertain only to the fully-developed region of a very large wind farm. Stevens, Arendshorst, and Wang (2017) reported several LES cases of vertically-staggered large scale developing wind farms. They found small power gains ranging from approximately 1% to 5% in the fully-developed region of the wind farm and significantly higher power gains ranging from approximately 5% to 15% in the developing region. Their findings for the fully-developed region compare well with our findings of net power gains ranging from approximately 2% to 6% (cf. Figure 4.7(b)), which is the more fitting comparison for our model. In addition, Stevens, Arendshorst, and Wang (2017) found that the power performance enhancement decreased with increasing turbine spacing, a result which we do not obtain in the present work. We find no discernible difference in power gains as a function of streamwise turbine spacing, however, we note that the streamwise-averaged nature of the RNL-LES approach is likely the source of the disagreement between the RNL-LES and LES results as we know that the RNL-LES approach becomes less valid with increasing turbine row spacings as shown in Figure 4.2. Additionally, the fully three-dimensional LES results more accurately capture streamwise developing events like wake effects, which significantly affect wind farm power output. The RNL-LES approach also confirms that power performance enhancement increases with increasing vertical staggering, as expected, and in agreement with the trend observed in the LES-based work of Stevens, Arendshorst, and Wang (2017).

Chapter 5

Conclusions

In summary, in the second chapter we report DNS of a band-limited RNL system which yield improved first- and second-order statistics compared to those obtained from baseline RNL simulations. A single $k_x \neq 0$ "band" yields mean velocity profiles approaching standard values for the parameters κ and B. The specific wavenumber to be retained in the model had to be determined empirically for each of the moderate Reynolds number cases considered here. The specific streamwise-varying wavenumber to be retained for each of the moderate Reynolds number cases considered here was determined empirically using the skin-friction coefficient of Eq. (2.2), i.e. a ratio relating the bulk mean velocity and the wall stress, thus providing a necessary condition for realistic reproduction of the mean velocity profile. The results for the cases considered suggest that the wavenumbers associated with the optimal modes follows an inner scaling. Increasing the bandwidth to include a set of three adjacent wavenumbers shows slightly improved statistics when compared with the single $k_x \neq 0$ case at $Re_\tau = 180$. RNL simulations of the single $k_x \neq 0$ case, however, enable significant savings in computational cost of

about a factor of 100 compared to DNS of Navier-Stokes for the Reynolds numbers considered here. Future directions for work on DNS of the RNL system include complementing these initial results at a range of moderate Reynolds numbers with simulations at higher Reynolds numbers to determine whether realistic logarithmic laws can be achieved at arbitrarily high Reynolds numbers. Also worthy of future investigation are the asymptotic scaling of the optimal wavenumber and behavior of second-order statistics.

In the third chapter of this work we have proposed the RNL-LES system, a new extension of the RNL system suitable for LES at arbitrarily high Reynolds number. We have described and implemented a new numerical approach to simulating the model which leverages important features of the RNL system to enable increased computational efficiency. Computational speedups as high as 17x relative to LES were observed for band-limited RNL-LES cases under Regime II (this regime is described in chapter three and also summarized below). However, at even finer LES grid resolutions, the computational savings associated with the RNL-LES system could be even larger. This numerical approach could also potentially be adapted to QL/GQL simulation frameworks for increased computational efficiency.

Our results indicate that, consistent with previous studies of the RNL system, the RNL-LES system naturally supports a reduced set of streamwise Fourier modes and sustains turbulence even when the dynamics are restricted to a single nonzero streamwise Fourier mode (interacting with the streamwise mean flow). We have demonstrated that proper band-limiting of the streamwise wavelengths results in a correction of the active spanwise

wavelengths (relative to the baseline RNL-LES) by shifting the peak regions in one-dimensional spanwise energy spectra towards smaller lengthscales. The resulting turbulence statistics of the band-limited RNL-LES system show significant improvement over those of the baseline RNL-LES system. We have developed a procedure for selecting these important streamwise lengthscales *a priori*, an improvement over the empirical approach employed in previous work. This lengthscale identification procedure for RNL-LES could also potentially be used to identify the important lengthscales to include in the DNS-RNL system, although this has not yet been tested and is beyond the scope of the current paper.

Furthermore, we have identified two regimes of band-limiting behavior: Regime I, which is comprised of a range of streamwise lengthscales centered about the dissipative small scale wavelength and Regime II, which is comprised of one 'box-scale' large scale and the grid resolution dependent dissipative small scale. In Regime I, we have shown that this band of wavelengths corresponds to (sub-grid scale) dissipative wavelengths in the corresponding LES system, as measured by the premultiplied vorticity spectra, and that these wavelengths are small LES scales that scale with the Smagorinsky lengthscale (i.e., the grid resolution). In Regime II, the larger grid sizes create the possibility for more scale separation, necessitating the introduction of a larger scale in addition to the dissipative small scale. For the domain considered in this study, this larger scale is the wavelength corresponding to $k_{x,7}$, which is the first wavelength smaller than the height of the half-channel. This large scale does not vary significantly as the grid size increases.

In light of the accuracy of the band-limited RNL-LES results, which were obtained with just a fraction of the degrees of freedom which would be required by a corresponding LES, the band-limited RNL-LES system could be of use in engineering application areas, especially those where the streamwise dynamics are not particularly important but where the cross-plane dynamics are of interest. Future research on the RNL-LES system involves introducing an additional nonlinear restriction between spanwise Fourier modes, along with potential band-limiting of spanwise modes to achieve an even further-reduced-order model of wall-bounded turbulence.

In the fourth chapter, we have proposed a new, reduced-order approach for simulating very large (fully-developed) wind farms by deploying an actuator disk turbine model in the recently-formulated RNL-LES framework. The results of the RNL-LES wind farm system compare favorably with those obtained by the LES wind farm system with a similar turbine model. Despite the simplified nature of the streamwise dynamics, the model effectively captures the effect of multiple streamwise rows of turbines, as measured by the resulting mean streamwise velocity profile. We are also able to accurately reproduce complex quantities like those terms found in the equations for the kinetic energy budget, quantities which are known to be critical in predicting wind farm power output and may be unattainable through other reduced-order approaches.

We leverage the low computational cost of the RNL-LES system to carry out a preliminary parametric study of the effect of vertical staggering on wind turbine performance, a segment of the wind farm LES literature which has

received little attention so far. Vertical staggering shows a net positive effect on wind farm power output relative to vertically-aligned wind farms for the cases considered herein. Fully exploring the question of whether or not vertical staggering could be beneficial in real wind farms would require the addition of an economic model in order to balance the trade-offs between vertical staggering and costs incurred, such as added material and maintenance costs for the larger wind turbines. Future work may include such economic models, as well as parametric sweeps across other wind farm parameters. Further understanding of vertical staggering effects within the developing region of wind farms is also needed, a topic which is not addressed in this work. Potential power production enhancements aside, understanding the overall effects of vertical staggering in wind farms is also a direction for future work. As a final note on directions for future work, we note that the RNL-LES wind farm simulation framework is potentially well-suited for simulating dynamic, time-dependent wind farm applications, e.g., as a reduced-order model for wind farm controls applications.

We conclude with a note on the computational cost of the RNL-LES approach. For the particular cross-plane grid size configuration considered here, we found computational speedups of approximately 5x for the RNL-LES approach relative to standard LES (using the same hardware and same number of processors). While only a small speedup, this nonetheless enabled us to set up an RNL-LES case and obtain results the same day, as opposed to waiting multiple days for the corresponding LES results. We thus found it straightforward to conduct all of the two hundred RNL-LES numerical simulations

produced for this work. Furthermore, the cross-plane grid size is relatively small for the cases reported herein, and we expect the speedup to increase with increasing cross-plane grid size, as in Bretheim, Meneveau, and Gayme (2018a), who reported speedups as high as 17x for larger grid sizes. This fact bodes well for future parametric studies of RNL-LES wind farms with higher cross-plane resolution.

References

Abkar, Mahdi and Fernando Porté-Agel (2013). "The Effect of Free-Atmosphere Stratification on Boundary-Layer Flow and Power Output from Very Large Wind Farms". In: *Energies* 6.5, pp. 2338–2361. ISSN: 1996-1073. DOI: 10.3390/en6052338. URL: http://www.mdpi.com/1996-1073/6/5/2338.

Abkar, Mahdi and Fernando Porté-Agel (2014). "Mean and turbulent kinetic energy budgets inside and above very large wind farms under conventionally-neutral condition". In: *Renewable Energy* 70.Supplement C, pp. 142 –152. ISSN: 0960-1481. DOI: https://doi.org/10.1016/j.renene.2014.03.050. URL: http://www.sciencedirect.com/science/article/pii/S0960148114002146.

Abkar, Mahdi and Fernando Porté-Agel (2015a). "A new wind-farm parameterization for large-scale atmospheric models". In: *Journal of Renewable and Sustainable Energy* 7.1, p. 013121. DOI: 10.1063/1.4907600. eprint: https://doi.org/10.1063/1.4907600. URL: https://doi.org/10.1063/1.4907600.

Abkar, Mahdi and Fernando Porté-Agel (2015b). "Influence of atmospheric stability on wind-turbine wakes: A large-eddy simulation study". In: *Physics of Fluids* 27.3, p. 035104. DOI: 10.1063/1.4913695. eprint: https://doi.org/10.1063/1.4913695. URL: https://doi.org/10.1063/1.4913695.

Abkar, Mahdi, Ahmad Sharifi, and Fernando Porté-Agel (2016). "Wake flow in a wind farm during a diurnal cycle". In: *Journal of Turbulence* 17.4, pp. 420–441. DOI: 10.1080/14685248.2015.1127379. eprint: https://doi.org/10.1080/14685248.2015.1127379. URL: https://doi.org/10.1080/14685248.2015.1127379.

Adrian, R. J., C. D. Meinhart, and C. D. Tomkins (2000). "Vortex organization in the outer region of the turbulent boundary layer". In: *Journal of Fluid Mechanics* 422, pp. 1–54. DOI: 10.1017/S0022112000001580.

Albertson, John David (1996). "Large eddy simulation of land-atmosphere interaction". PhD thesis. University of California - Davis.

Alizard, Frédéric (2017). "Invariant solutions in a channel flow using a minimal restricted nonlinear model". In: *Comptes Rendus Mécanique* 345.2, pp. 117–124. ISSN: 1631-0721. DOI: http://dx.doi.org/10.1016/j.crme.2016.11.005. URL: http://www.sciencedirect.com/science/article/pii/S1631072116301401.

Allaerts, Dries and Johan Meyers (2015). "Large eddy simulation of a large wind-turbine array in a conventionally neutral atmospheric boundary layer". In: *Physics of Fluids* 27.6, p. 065108. DOI: 10.1063/1.4922339. eprint:

https://doi.org/10.1063/1.4922339. URL: https://doi.org/10.1063/1.4922339.

Archer, Cristina L., Sina Mirzaeisefat, and Sang Lee (2013). "Quantifying the sensitivity of wind farm performance to array layout options using large-eddy simulation". In: *Geophysical Research Letters* 40.18, pp. 4963–4970. ISSN: 1944-8007. DOI: 10.1002/grl.50911. URL: http://dx.doi.org/10.1002/grl.50911.

Bamieh, Bassam and Mohammed Dahleh (2001). "Energy amplification in channel flows with stochastic excitation". In: *Physics of Fluids* 13.11, pp. 3258–3269. DOI: 10.1063/1.1398044. eprint: http://dx.doi.org/10.1063/1.1398044. URL: http://dx.doi.org/10.1063/1.1398044.

Barthelmie, RJ, ST Frandsen, K Hansen, JG Schepers, K Rados, W Schlez, A Neubert, LE Jensen, and S Neckelmann (2009). "Modelling the impact of wakes on power output at Nysted and Horns Rev". In: *European Wind Energy Conference*.

Bastankhah, Majid and Fernando Porté-Agel (2014). "A new analytical model for wind-turbine wakes". In: *Renewable Energy* 70.Supplement C, pp. 116–123. ISSN: 0960-1481. DOI: https://doi.org/10.1016/j.renene.2014.01.002. URL: http://www.sciencedirect.com/science/article/pii/S0960148114000317.

Bobba, K. M. (2004). "Robust Flow Stability: Theory, Computations, and Experiments in Near Wall Turbulence". Ph.D. thesis. Pasadena, California, USA: California Institute of Technology.

Boersma, S., B. Doekemeijer, M. Vali, J. Meyers, and J.-W. van Wingerden (2017). "A control-oriented dynamic wind farm model: WFSim". In: *Wind Energy Science Discussions* 2017, pp. 1–34. DOI: 10.5194/wes-2017-44. URL: https://www.wind-energ-sci-discuss.net/wes-2017-44/.

Bourguignon, Jean-Loup and Beverley J McKeon (2011). "A streamwise-constant model of turbulent pipe flow". In: *Physics of Fluids* 23.9, p. 095111.

Bretheim, J. U., C. Meneveau, and D. F. Gayme (2015). "Standard logarithmic mean velocity distribution in a band-limited restricted nonlinear model of turbulent flow in a half-channel". In: *Physics of Fluids* 27.1, p. 011702. DOI: 10.1063/1.4906987. eprint: http://dx.doi.org/10.1063/1.4906987. URL: http://dx.doi.org/10.1063/1.4906987.

Bretheim, Joel U., Charles Meneveau, and Dennice F. Gayme (2017). "The restricted non linear - LES approach to simulations of large wind farms". In: *to appear in Bulletin of the American Physical Society, Division of Fluid Dynamics*. American Physical Society, Division of Fluid Dynamics. Denver, CO.

Bretheim, Joel U., Charles Meneveau, and Dennice F. Gayme (2018a). "A restricted nonlinear large eddy simulation model for high Reynolds number flows". In: *Journal of Turbulence* 19.2, pp. 141–166. DOI: 10.1080/14685248.

2017.1403031. eprint: https://doi.org/10.1080/14685248.2017.1403031. URL: https://doi.org/10.1080/14685248.2017.1403031.

Bretheim, Joel U., Charles Meneveau, and Dennice F. Gayme (2018b). "The restricted nonlinear large eddy simulation approach to reduced-order wind farm modeling". In: *submitted*.

Cal, Raúl Bayoán, José Lebrón, Luciano Castillo, Hyung Suk Kang, and Charles Meneveau (2010). "Experimental study of the horizontally averaged flow structure in a model wind-turbine array boundary layer". In: *Journal of Renewable and Sustainable Energy* 2.1, p. 013106.

Calaf, Marc, Charles Meneveau, and Johan Meyers (2010). "Large eddy simulation study of fully developed wind-turbine array boundary layers". In: *Physics of Fluids* 22.1, p. 015110. DOI: 10.1063/1.3291077. eprint: http://dx.doi.org/10.1063/1.3291077. URL: http://dx.doi.org/10.1063/1.3291077.

Calaf, Marc, Marc B. Parlange, and Charles Meneveau (2011). "Large eddy simulation study of scalar transport in fully developed wind-turbine array boundary layers". In: *Physics of Fluids* 23.12, p. 126603. DOI: 10.1063/1.3663376. eprint: https://doi.org/10.1063/1.3663376. URL: https://doi.org/10.1063/1.3663376.

Constantinou, N C, A Lozano-Durán, M-A Nikolaidis, B F Farrell, P J Ioannou, and J Jiménez (2014). "Turbulence in the highly restricted dynamics of a closure at second order: comparison with DNS". In: *Journal of Physics:*

Conference Series 506.1, p. 012004. URL: http://stacks.iop.org/1742-6596/506/i=1/a=012004.

Constantinou, Navid C., Brian F. Farrell, and Petros J. Ioannou (2016). "Statistical state dynamics of jet-wave coexistence in barotropic beta-plane turbulence". In: *Journal of the Atmospheric Sciences* 73.5, pp. 2229–2253. DOI: 10.1175/JAS-D-15-0288.1. eprint: https://doi.org/10.1175/JAS-D-15-0288.1. URL: https://doi.org/10.1175/JAS-D-15-0288.1.

Farrell, B. F., D. F. Gayme, and P. J. Ioannou (2017). "A statistical state dynamics approach to wall turbulence". In: *Philosophical Transactions of the Royal Society of London A: Mathematical, Physical and Engineering Sciences* 375.2089. ISSN: 1364-503X. DOI: 10.1098/rsta.2016.0081. eprint: http://rsta.royalsocietypublishing.org/content/375/2089/20160081.full.pdf. URL: http://rsta.royalsocietypublishing.org/content/375/2089/20160081.

Farrell, Brian F. and Petros J. Ioannou (1993). "Optimal excitation of three–dimensional perturbations in viscous constant shear flow". In: *Physics of Fluids A: Fluid Dynamics* 5.6, pp. 1390–1400. DOI: 10.1063/1.858574. eprint: http://dx.doi.org/10.1063/1.858574. URL: http://dx.doi.org/10.1063/1.858574.

Farrell, Brian F. and Petros J. Ioannou (2003). "Structural stability of turbulent jets". In: *Journal of the Atmospheric Sciences* 60.17, pp. 2101–2118. DOI: 10.1175/1520-0469(2003)060<2101:SSOTJ>2.0.CO;2. eprint: https://

doi.org/10.1175/1520-0469(2003)060<2101:SSOTJ>2.0.CO;2. URL: https://doi.org/10.1175/1520-0469(2003)060<2101:SSOTJ>2.0.CO;2.

Farrell, Brian F. and Petros J. Ioannou (2007). "Structure and spacing of jets in barotropic turbulence". In: *Journal of the Atmospheric Sciences* 64.10, pp. 3652–3665. DOI: 10.1175/JAS4016.1. eprint: https://doi.org/10.1175/JAS4016.1. URL: https://doi.org/10.1175/JAS4016.1.

Farrell, Brian F. and Petros J. Ioannou (2012). "Dynamics of streamwise rolls and streaks in turbulent wall-bounded shear flow". In: *Journal of Fluid Mechanics* 708, pp. 149–196. DOI: 10.1017/jfm.2012.300.

Farrell, Brian F. and Petros J. Ioannou (2017). "Statistical state dynamics based theory for the formation and equilibration of Saturn's north polar jet". In: *Phys. Rev. Fluids* 2 (7), p. 073801. DOI: 10.1103/PhysRevFluids.2.073801. URL: https://link.aps.org/doi/10.1103/PhysRevFluids.2.073801.

Farrell, Brian F., Petros J. Ioannou, and Marios-Andreas Nikolaidis (2017). "Instability of the roll-streak structure induced by background turbulence in pretransitional Couette flow". In: *Phys. Rev. Fluids* 2 (3), p. 034607. DOI: 10.1103/PhysRevFluids.2.034607. URL: https://link.aps.org/doi/10.1103/PhysRevFluids.2.034607.

Farrell, Brian F., Dennice F. Gayme, Petros J. Ioannou, B. K. Lieu, and M. R. Jovanović (2012). "Dynamics of the roll and streak structure in transition and turbulence". In: *Proceedings of the Center for Turbulence Research Summer Program*, pp. 34–54.

Farrell, Brian F., Petros J. Ioannou, Javier Jiménez, Navid C. Constantinou, Adrián Lozano-Durán, and Marios-Andreas Nikolaidis (2016). "A statistical state dynamics-based study of the structure and mechanism of large-scale motions in plane Poiseuille flow". In: *Journal of Fluid Mechanics* 809, pp. 290–315. DOI: 10.1017/jfm.2016.661.

Gayme, D. F., B. J. McKeon, A. Papachristodoulou, B. Bamieh, and J. C. Doyle (2010). "A streamwise constant model of turbulence in plane Couette flow". In: *Journal of Fluid Mechanics* 665, pp. 99–119. DOI: 10.1017/S0022112010003861.

Gayme, D. F., V. Thomas, B. F. Farrell, and P. J. Ioannou (Nov. 2013). "A minimal representation of turbulence in plane Couette flow". In: *Bulletin of the American Physical Society, Div. of Fluid Dynamics, Pittsburgh, PA*.

Gayme, Dennice F, Beverley J McKeon, Bassam Bamieh, Antonis Papachristo doulou, and John C Doyle (2011). "Amplification and nonlinear mechanisms in plane Couette flow". In: *Physics of Fluids* 23.6, p. 065108.

Gibson, J. F., J. Halcrow, and P. Cvitanović (2008). "Visualizing the geometry of state space in plane Couette flow". In: *Journal of Fluid Mechanics* 611, pp. 107–130. DOI: 10.1017/S002211200800267X.

Graham, Jason and Charles Meneveau (2012). "Modeling turbulent flow over fractal trees using renormalized numerical simulation: Alternate formulations and numerical experiments". In: *Physics of Fluids* 24.12, p. 125105.

DOI: 10.1063/1.4772074. eprint: http://dx.doi.org/10.1063/1.4772074. URL: http://dx.doi.org/10.1063/1.4772074.

Hamilton, James M, John Kim, and Fabian Waleffe (1995). "Regeneration mechanisms of near-wall turbulence structures". In: *Journal of Fluid Mechanics* 287, pp. 317–348.

Howland, Michael F., Juliaan Bossuyt, Luis A. Martínez-Tossas, Johan Meyers, and Charles Meneveau (2016). "Wake structure in actuator disk models of wind turbines in yaw under uniform inflow conditions". In: *Journal of Renewable and Sustainable Energy* 8.4, p. 043301. DOI: 10.1063/1.4955091. eprint: https://doi.org/10.1063/1.4955091. URL: https://doi.org/10.1063/1.4955091.

Hutchins, Nicholas and Ivan Marusic (2007a). "Evidence of very long meandering features in the logarithmic region of turbulent boundary layers". In: *Journal of Fluid Mechanics* 579, pp. 1–28.

Hutchins, Nicholas and Ivan Marusic (2007b). "Large-scale influences in near-wall turbulence". In: *Philosophical Transactions of the Royal Society of London A: Mathematical, Physical and Engineering Sciences* 365.1852, pp. 647–664.

Iungo, G V, C Santoni-Ortiz, M Abkar, F Porté-Agel, M A Rotea, and S Leonardi (2015). "Data-driven Reduced Order Model for prediction of wind turbine wakes". In: *Journal of Physics: Conference Series* 625.1, p. 012009. URL: http://stacks.iop.org/1742-6596/625/i=1/a=012009.

Iungo, Giacomo Valerio, Vignesh Santhanagopalan, Umberto Ciri, Francesco Viola, Lu Zhan, Mario A. Rotea, and Stefano Leonardi (2017). "Parabolic RANS solver for low-computational-cost simulations of wind turbine wakes". In: *Wind Energy*, n/a–n/a. ISSN: 1099-1824. DOI: 10.1002/we.2154. URL: http://dx.doi.org/10.1002/we.2154.

Jha, Pankaj K. and Sven Schmitz (2018). "Actuator curve embedding âĂŞ an advanced actuator line model". In: *Journal of Fluid Mechanics* 834. DOI: 10.1017/jfm.2017.793.

Jiménez, Javier (2012). "Cascades in wall-bounded turbulence". In: *Annu. Rev. Fluid Mech.* 44, pp. 27–45.

Jiménez, Javier (2012). "Cascades in wall-bounded turbulence". In: *Annual Review of Fluid Mechanics* 44.1, pp. 27–45. DOI: 10.1146/annurev-fluid-120710-101039. eprint: https://doi.org/10.1146/annurev-fluid-120710-101039. URL: https://doi.org/10.1146/annurev-fluid-120710-101039.

Jiménez, Javier and Parviz Moin (1991). "The minimal flow unit in near-wall turbulence". In: *J. Fluid Mech.* 225, pp. 213–40.

Jovanović, Mihailo R. and Bassam Bamieh (2005). "Componentwise energy amplification in channel flows". In: *Journal of Fluid Mechanics* 534, pp. 145–183. DOI: 10.1017/S0022112005004295.

Katic, I, J Højstrup, and Niels Otto Jensen (1986). "A simple model for cluster efficiency". In: *European wind energy association conference and exhibition*, pp. 407–410.

Kawahara, Genta, Markus Uhlmann, and Lennaert van Veen (2012). "The significance of simple invariant solutions in turbulent flows". In: *Annual Review of Fluid Mechanics* 44.1, pp. 203–225. DOI: 10.1146/annurev-fluid-120710-101228. eprint: https://doi.org/10.1146/annurev-fluid-120710-101228. URL: https://doi.org/10.1146/annurev-fluid-120710-101228.

Kim, J., P. Moin, and R. Moser (1987). "Turbulence statistics in fully developed channel flow at low Reynolds number". In: *J. Fluid Mech.* 177, pp. 133–66.

Klewicki, J. C., G. P. Chini, and J. F. Gibson (2017). "Prospectus: towards the development of high-fidelity models of wall turbulence at large Reynolds number". In: *Philosophical Transactions of the Royal Society of London A: Mathematical, Physical and Engineering Sciences* 375.2089. ISSN: 1364-503X. DOI: 10.1098/rsta.2016.0092. eprint: http://rsta.royalsocietypublishing.org/content/375/2089/20160092.full.pdf.

Kline, S. J., W. C. Reynolds, F. A. Schraub, and P. W. Runstadler (1967). "The structure of turbulent boundary layers". In: *Journal of Fluid Mechanics* 30.4, pp. 741–773. DOI: 10.1017/S0022112067001740.

Lee, Myoungkyu and Robert D. Moser (2015). "Direct numerical simulation of turbulent channel flow up to $Re_\tau \approx 5200$". In: *Journal of Fluid Mechanics* 774, pp. 395–415. DOI: 10.1017/jfm.2015.268.

Lu, Hao and Fernando Porté-Agel (2011). "Large-eddy simulation of a very large wind farm in a stable atmospheric boundary layer". In: *Physics of Fluids* 23.6, p. 065101. DOI: 10.1063/1.3589857. eprint: https://doi.org/10.1063/1.3589857. URL: https://doi.org/10.1063/1.3589857.

Lu, Hao and Fernando Porté-Agel (2015). "On the Impact of Wind Farms on a Convective Atmospheric Boundary Layer". In: *Boundary-Layer Meteorology* 157.1, pp. 81–96. ISSN: 1573-1472. DOI: 10.1007/s10546-015-0049-1. URL: https://doi.org/10.1007/s10546-015-0049-1.

Marston, J. B., G. P. Chini, and S. M. Tobias (2016). "Generalized quasilinear approximation: application to zonal jets". In: *Phys. Rev. Lett.* 116 (21), p. 214501. DOI: 10.1103/PhysRevLett.116.214501. URL: https://link.aps.org/doi/10.1103/PhysRevLett.116.214501.

Marston, J. B., E. Conover, and Tapio Schneider (2008). "Statistics of an unstable barotropic jet from a cumulant expansion". In: *Journal of the Atmospheric Sciences* 65.6, pp. 1955–1966. DOI: 10.1175/2007JAS2510.1. eprint: https://doi.org/10.1175/2007JAS2510.1. URL: https://doi.org/10.1175/2007JAS2510.1.

Martínez-Tossas, L. A., M. J. Churchfield, and C. Meneveau (2017). "Optimal smoothing length scale for actuator line models of wind turbine blades

based on Gaussian body force distribution". In: *Wind Energy* 20.6, pp. 1083–1096. ISSN: 1099-1824. DOI: 10.1002/we.2081. URL: http://dx.doi.org/10.1002/we.2081.

Martínez-Tossas, Luis A., Matthew J. Churchfield, and Stefano Leonardi (2015). "Large eddy simulations of the flow past wind turbines: actuator line and disk modeling". In: *Wind Energy* 18.6, pp. 1047–1060. ISSN: 1099-1824. DOI: 10.1002/we.1747. URL: http://dx.doi.org/10.1002/we.1747.

McKeon, B. J. and A. S. Sharma (2010). "A critical-layer framework for turbulent pipe flow". In: *Journal of Fluid Mechanics* 658, pp. 336–382. DOI: 10.1017/S002211201000176X.

Meyers, Johan and Charles Meneveau (2012). "Optimal turbine spacing in fully developed wind farm boundary layers". In: *Wind Energy* 15.2, pp. 305–317. ISSN: 1099-1824. DOI: 10.1002/we.469. URL: http://dx.doi.org/10.1002/we.469.

Morrison, Jonathan F, BJ McKeon, W Jiang, and AJ Smits (2004). "Scaling of the streamwise velocity component in turbulent pipe flow". In: *Journal of Fluid Mechanics* 508, pp. 99–131.

Moser, Robert D., John Kim, and Nagi N. Mansour (1999). "Direct numerical simulation of turbulent channel flow up to Re = 590". In: *Phys. Fluids* 11.

Pope, Stephen B. (2000). "Turbulent Flows". In: First. Cambridge, UK: Cambridge University Press. Chap. 7.1, p. 278.

Porté-Agel, Fernando, Charles Meneveau, and Marc B Parlange (2000). "A scale-dependent dynamic model for large-eddy simulation: application to a neutral atmospheric boundary layer". In: *Journal of Fluid Mechanics* 415, pp. 261–284.

Robinson, Stephen K (1991). "Coherent motions in the turbulent boundary layer". In: *Annual Review of Fluid Mechanics* 23.1, pp. 601–639.

Romanov, V. A. (1973). "Stability of plane-parallel Couette flow". In: *Functional Analysis and Its Applications* 7.2, pp. 137–146. ISSN: 1573-8485. DOI: 10.1007/BF01078886. URL: https://doi.org/10.1007/BF01078886.

Sanderse, Benjamin, SP Pijl, and Barry Koren (2011). "Review of computational fluid dynamics for wind turbine wake aerodynamics". In: *Wind energy* 14.7, pp. 799–819.

Schmidt, Helmut and Ulrich Schumann (1989). "Coherent structure of the convective boundary layer derived from large-eddy simulations". In: *Journal of Fluid Mechanics* 200, pp. 511–562. DOI: 10.1017/S0022112089000753.

Scotti, Alberto, Charles Meneveau, and Douglas K. Lilly (1993). "Generalized Smagorinsky model for anisotropic grids". In: *Physics of Fluids A: Fluid Dynamics* 5.9, pp. 2306–2308. DOI: 10.1063/1.858537. eprint: http://dx.doi.org/10.1063/1.858537. URL: http://dx.doi.org/10.1063/1.858537.

Shapiro, C. R., J. Meyers, C. Meneveau, and D. F. Gayme (2017a). "Dynamic wake modeling and state estimation for improved model-based receding

horizon control of wind farms". In: *2017 American Control Conference (ACC)*, pp. 709–716. DOI: 10.23919/ACC.2017.7963036.

Shapiro, Carl R., Johan Meyers, Charles Meneveau, and Dennice F. Gayme (2016). "Wind farms providing secondary frequency regulation: Evaluating the performance of model-based receding horizon control". In: *Journal of Physics: Conference Series* 753.5, p. 052012. URL: http://stacks.iop.org/1742-6596/753/i=5/a=052012.

Shapiro, Carl R., Pieter Bauweraerts, Johan Meyers, Charles Meneveau, and Dennice F. Gayme (2017b). "Model-based receding horizon control of wind farms for secondary frequency regulation". In: *Wind Energy* 20.7, pp. 1261–1275. ISSN: 1099-1824. DOI: 10.1002/we.2093. URL: http://dx.doi.org/10.1002/we.2093.

Sharma, A. S. and B. J. McKeon (2013). "On coherent structure in wall turbulence". In: *Journal of Fluid Mechanics* 728, pp. 196–238. DOI: 10.1017/jfm.2013.286.

Sharma, A. S., R. Moarref, and B. J. McKeon (2017). "Scaling and interaction of self-similar modes in models of high Reynolds number wall turbulence". In: *Philosophical Transactions of the Royal Society of London A: Mathematical, Physical and Engineering Sciences* 375.2089. ISSN: 1364-503X. DOI: 10.1098/rsta.2016.0089. eprint: http://rsta.royalsocietypublishing.org/content/375/2089/20160089.full.pdf.

Sharma, V., M. B. Parlange, and M. Calaf (2017). "Perturbations to the Spatial and Temporal Characteristics of the Diurnally-Varying Atmospheric Boundary Layer Due to an Extensive Wind Farm". In: *Boundary-Layer Meteorology* 162.2, pp. 255–282. ISSN: 1573-1472. DOI: 10.1007/s10546-016-0195-0. URL: https://doi.org/10.1007/s10546-016-0195-0.

Smagorinsky, Joseph (1963). "General circulation experiments with the primitive equations: I. The basic experiment". In: *Monthly weather review* 91.3, pp. 99–164.

Smith, C. R. and S. P. Metzler (1983). "The characteristics of low-speed streaks in the near-wall region of a turbulent boundary layer". In: *J. Fluid Mech.* 129, pp. 27–54.

Smits, Alexander J, Beverley J McKeon, and Ivan Marusic (2011). "High–Reynolds number wall turbulence". In: *Annual Review of Fluid Mechanics* 43, pp. 353–375.

Srinivasan, Kaushik and W. R. Young (2012). "Zonostrophic instability". In: *Journal of the Atmospheric Sciences* 69.5, pp. 1633–1656. DOI: 10.1175/JAS-D-11-0200.1. eprint: https://doi.org/10.1175/JAS-D-11-0200.1. URL: https://doi.org/10.1175/JAS-D-11-0200.1.

Stevens, Richard, Mark Arendshorst, and Mengqi Wang (2017). "Large eddy simulation study on the effect of vertical staggering in large-scale wind farms". In: *Bulletin of the American Physical Society, Division of Fluid Dynamics*. 62 14. American Physical Society. Denver, CO, p. 525.

Stevens, Richard J. A. M., Dennice F. Gayme, and Charles Meneveau (2014). "Large eddy simulation studies of the effects of alignment and wind farm length". In: *Journal of Renewable and Sustainable Energy* 6.2, p. 023105. DOI: 10.1063/1.4869568. eprint: https://doi.org/10.1063/1.4869568. URL: https://doi.org/10.1063/1.4869568.

Stevens, Richard J. A. M., Dennice F. Gayme, and Charles Meneveau (2015). "Coupled wake boundary layer model of wind-farms". In: *Journal of Renewable and Sustainable Energy* 7.2, p. 023115. DOI: 10.1063/1.4915287. eprint: https://doi.org/10.1063/1.4915287. URL: https://doi.org/10.1063/1.4915287.

Stevens, Richard J. A. M., Dennice F. Gayme, and Charles Meneveau (2016a). "Generalized coupled wake boundary layer model: applications and comparisons with field and LES data for two wind farms". In: *Wind Energy* 19.11, pp. 2023–2040. ISSN: 1099-1824. DOI: 10.1002/we.1966. URL: http://dx.doi.org/10.1002/we.1966.

Stevens, Richard J.A.M., Dennice F. Gayme, and Charles Meneveau (2016b). "Effects of turbine spacing on the power output of extended wind-farms". In: *Wind Energy* 19.2, pp. 359–370. ISSN: 1099-1824. DOI: 10.1002/we.1835. URL: http://dx.doi.org/10.1002/we.1835.

Stevens, Richard J.A.M., Jason Graham, and Charles Meneveau (2014). "A concurrent precursor inflow method for Large Eddy Simulations and applications to finite length wind farms". In: *Renewable Energy* 68.Supplement C, pp. 46 –50. ISSN: 0960-1481. DOI: https://doi.org/10.1016/j.renene.

2014.01.024. URL: http://www.sciencedirect.com/science/article/pii/S0960148114000536.

Stevens, Richard J.A.M. and Charles Meneveau (2017). "Flow Structure and Turbulence in Wind Farms". In: *Annual Review of Fluid Mechanics* 49.1, pp. 311–339. DOI: 10.1146/annurev-fluid-010816-060206. eprint: https://doi.org/10.1146/annurev-fluid-010816-060206. URL: https://doi.org/10.1146/annurev-fluid-010816-060206.

Thomas, Vaughan L., Binh K. Lieu, Mihailo R. Jovanović, Brian F. Farrell, Petros J. Ioannou, and Dennice F. Gayme (2014). "Self-sustaining turbulence in a restricted nonlinear model of plane Couette flow". In: *Physics of Fluids* 26.10, p. 105112. DOI: 10.1063/1.4898159. eprint: http://dx.doi.org/10.1063/1.4898159. URL: http://dx.doi.org/10.1063/1.4898159.

Thomas, Vaughan L., Brian F. Farrell, Petros J. Ioannou, and Dennice F. Gayme (2015). "A minimal model of self-sustaining turbulence". In: *Physics of Fluids* 27.10, p. 105104. DOI: 10.1063/1.4931776. eprint: http://dx.doi.org/10.1063/1.4931776. URL: http://dx.doi.org/10.1063/1.4931776.

Tobias, S. M. and J. B. Marston (2017). "Three-dimensional rotating Couette flow via the generalised quasilinear approximation". In: *Journal of Fluid Mechanics* 810, pp. 412–428. DOI: 10.1017/jfm.2016.727.

Vasel-Be-Hagh, Ahmadreza and Cristina L Archer (2017). "Wind farm hub height optimization". In: *Applied Energy* 195, pp. 905–921.

VerHulst, Claire and Charles Meneveau (2014). "Large eddy simulation study of the kinetic energy entrainment by energetic turbulent flow structures in large wind farms". In: *Physics of Fluids* 26.2, p. 025113. DOI: 10.1063/1.4865755. eprint: http://dx.doi.org/10.1063/1.4865755. URL: http://dx.doi.org/10.1063/1.4865755.

VerHulst, Claire and Charles Meneveau (2015). "Altering Kinetic Energy Entrainment in Large Eddy Simulations of Large Wind Farms Using Unconventional Wind Turbine Actuator Forcing". In: *Energies* 8.1, pp. 370–386. ISSN: 1996-1073. DOI: 10.3390/en8010370. URL: http://www.mdpi.com/1996-1073/8/1/370.

Waleffe, Fabian (2001). "Exact coherent structures in channel flow". In: *Journal of Fluid Mechanics* 435, pp. 93–102. DOI: 10.1017/S0022112001004189.

Xie, Shengbai and Cristina Archer (2015). "Self-similarity and turbulence characteristics of wind turbine wakes via large-eddy simulation". In: *Wind Energy* 18.10, pp. 1815–1838. ISSN: 1099-1824. DOI: 10.1002/we.1792. URL: http://dx.doi.org/10.1002/we.1792.

Vita

Joel U. Bretheim was born in 1990 in Redmond, Washington. He graduated from North Hunterdon High School in Annandale, New Jersey, in 2008. He attended Grove City College in Grove City, Pennsylvania, graduating in 2012. He began his doctoral studies later that year at Johns Hopkins University in Baltimore, Maryland.